COMPUTATIONAL METHODS IN RADIATION ONCOLOGY

A thesis submitted in partial fulfilment
of the requirements for a
Doctorate of Philosophy

Richard P. Hugtenburg

UNIVERSITY OF CANTERBURY

Department of Physics and Astronomy

CHRISTCHURCH NEW ZEALAND

1998

Abstract

This thesis examines computer technology in radiation oncology and the intimate role that it must now play in the dosimetry practices of this discipline. Aspects of the dosimetry and implementation of five radiation therapies are examined, namely total-body irradiation (TBI), total-skin electron therapy (TSET), electron therapy, superficial therapy and ophthalmic brachytherapy.

Computational techniques, in particular, Monte Carlo and several other numerical methods are used. The Monte Carlo platform, EGS4, and the treatment planning system, GRATIS, have been implemented on SUN and Silicon Graphics workstations. Monte Carlo methods are used in the investigation of electron therapy planning and superficial and brachytherapy dosimetry practices.

Monte Carlo techniques are used for radiation protection calculations of linear accelerator bunker design and for the optimisation of an *in vivo* X-ray fluorescence (XRF) technique used to measure platinum uptake associated with cisplatin chemotherapy.

Inverse Monte Carlo methods have been examined and implemented. Inverse methods, applied to in-phantom dose measurements, are used to determine phase-space information, such as spectra, for an incident electron beam. Analogous methods are examined for megavoltage and superficial X-rays, in particular, source parameterisation with attenuation and photoactivation techniques.

Two linear accelerators, a Varian 2100C and a Varian 600C, provide megavoltage X-rays or electrons. The TBI therapy uses a 6 MV X-ray beam. The TSET technique uses 6 MeV electrons which degraded to a lower energy by a screen placed in front of the patient at an extended source distance. The 9 MeV and the 20 MeV electron modalities are also closely examined. Two Philips superficial therapy units, RT100 and RT50 provide 10 through 100 kVp X-rays. ^{125}I seeds are used for the investigation of ophthalmic brachytherapy dosimetry.

Methods of dosimetry incorporated in this work include in-phantom, ionisation-chamber and diode measurements. Thermoluminescent dosimeters (TLDs), Silver-halide and radiochromic films are used. Measurements have been performed in water, solid water, polymethyl-methacrylate (PMMA), and polystyrene phantoms. Fricke, ferrous based, gels are investigated as a method of dosimetry in a uniform medium. Three-dimensional dose distributions are examined for several radiation modalities. The concentration of radiation-induced ferric ions and hence dose is determined using magnetic resonance imaging (MRI). A high-purity germanium detector and a thalium doped sodium iodide detector are employed for the measurement of source spectra and for fluorescing and activated materials.

Contents

Figures

Chapter 1

Introduction

1.1 History

The material in this thesis is a reflection of the growing role of computers in radiotherapy dosimetry. The thesis builds on a programme of medical physics research here in Christchurch, including the development of algorithms ultimately intended for use in the day-to-day practice of radiation oncology planning.

A method for calculating photon therapy treatment plans was first suggested by Clarkson[4]. Our own in-house implementation of this algorithm[5, 6] was originally coded on a PDP-8 (Digital Equipment Corp.) and subsequently installed at several other centres in Australasia. The implementation shares similarities with Digital's own implementation of the algorithm[7].

Workers at the University of Canterbury were responsible for the early operation of a computer tomography scanner[8, 9]. There has also been development here in the amalgamation of CT information into radiation oncology planning[10, 11, 12].

More recently a commercial treatment planning system has been purchased by the Christchurch Oncology Service. "FOCUS" (Computer Medical Systems) is one of a number of a new generation of treatment planning systems that perform pseudo three-dimensional calculations. FOCUS incorporates a modified Clarkson sector-integration algorithm[13, 14] for photon dosimetry and the electron pencil beam method, developed independently by a number of workers [15, 16, 17, 18, 19], for electron dosimetry. More will be said about the history of electron algorithms when the transport equation is introduced later in the chapter.

The inclusion of electron algorithms in commercial treatment planning systems is a recent innovation and is a reflection of both the growing popularity of this type of radiation in therapy and of performance gains in computer technology.

The material in this thesis covers a broad range of dosimetry problems. Various techniques both experimental and analytical have been used. The in-

volvement of computational methods in this research has been mandatory and a keen eye on the state-of-the-art, in particular on performance measures[20, 21, 22, 23, 24], is useful to contextualise this research. In recent years the Clarkson algorithm has been replaced by methods which offer a closer approximation to the fundamental physics and which better acknowledge the full three-dimensional and multiple-scatter nature of this problem. While these methods offer greater accuracy, the algorithms require orders of magnitude more clock cycles. In general, the thoroughness of treatment algorithms parallels gains in computer technology, though this is not always the case. In particular, a slower more studious algorithm may not be an improvement in a busy clinical environment.

Much of this thesis is concerned with the application of the Monte Carlo method to the problem of radiation transport in materials and tissue. The Monte Carlo method adds a high level accuracy and scientific rigour to these types of problems but it is a computationally intensive method. Despite its inherent slowness it is now used extensively in radiation dosimetry for calculations that are only required to be performed once. More significantly it is very useful in support of experimental methods and various less precise modelling techniques.

This thesis includes examples of dosimetry techniques used in a variety of treatment scenarios and in a range of radiation types. The manner in which these calculations progress often depends critically on the geometrical aspects and radiation properties of the treatment scenario. As a result the reader will find contrasting methods used in each chapter.

1.2 Overview of research

Chapters two and three are concerned with large field techniques used in the treatment of whole-body conditions. Large field therapies present a number of dosimetric issues. Contrary to standard dosimetry practices the determination of dose is performed in a volume (phantom) that is generally smaller than the extent of the field. Frequently the dose is determined in air and related to the dose, in-vivo, using tabulated values of the tissue-to-air ratios (TAR). Our practice differs slightly. It has been the preference at Christchurch Oncology Service to perform in-phantom measurements wherever possible. This circumvents a reliance on tabulated data which can then be used for the sake of comparison.

First we consider a total skin therapy (TSET) that uses 2.5 and 3.5 MeV electrons. This technique is used to treat the condition mycosis fungoides. The

chapter is a brief introduction to electron dosimetry and to the determination of absorbed dose from the computerised convolution of overlapping radiation fields. This work has been published in the manner of a dosimetry protocol[25]. The chapter presented here is proportion of the publication and representative of experimental work performed by Mr John Turner and myself. It is appropriate to acknowledge here the clinical involvement of Dr Chris Wynne, who shares co-authorship of the published paper.

The second whole-body treatment examined is a total body irradiation (TBI) technique using 6 MV X-rays. TBI is a critical procedure in the bone marrow transplant operation used to treat leukemias of various types. This chapter discusses standard dosimetry calculations including the formulation of a table of TMR values specific to the determination of dose in this treatment methodology. The present method of therapy distinguishes itself from other methods of TBI in that it is a prone/supine treatment performed on an isocentrically mounted accelerator. It is proposed that the accelerator output be controlled to deliver a uniform field about the patient. The feasibility of this method has been analysed and subsequently presented[26, 27, 28] and published[29]. Interest in this work by Varian Inc. of Palo Alto, has lead to a contract of research with the Christchurch Oncology Service and the installation of software control capabilities on an accelerator here.

Chapter three is based substantially on this work and contributions from Messrs Shaun Baggerley, John Turner, Niles Oien and David Pinchin, Drs Chris Atkinson and Richard Tremewan are ackonwledged. Further work, using the Monte Carlo method to investigate the effects of highly oblique beam incidences at the extremes of the patient anatomy and corrections for lung inhomogeneity, is presented in the masters thesis of Mr Peter Love[30].

In chapters four to seven, the Monte Carlo method is applied other radiation problems. Monte Carlo is an extremely useful tool in radiotherapy physics. Consequently the development of a facility to perform such calculations has been advantageous for both therapy and non-therapy radiation applications at Christchurch Hospital. Two projects, although peripheral to radiation oncology itself, are included in this thesis.

The first of these projects (chapter four) is an examination of radiotherapy bunker design in response to the installation of a 6 MV linear accelerator[31] and in preparation for the installation of a 10 MV linear accelerator[32]. The design of bunkers is a radiation protection issue and an aspect of dosimetry that every oncology department must be concerned with. Monte Carlo code has been written entitled MAZE2D. The code has an adequate front end that enables a less programming-orientated user to enter maze structure coordinates

or indeed parse this information from a computer aided design (CAD) package.

In chapter five Monte Carlo methods are used to optimise an X-ray fluorescence system for determining the uptake of heavy metals in humans. The uptake of platinum in the form of the cytostatic chemotherapy agent, cisplatin, has been examined[33, 34]. Here is a case where radiation is used as a dosimetric aid for chemotherapy. Issues of radiation dosimetry (or radiation protection) need also be adhered to because of the application of radiation *in vivo*. This chapter is based on a published paper that deals principally with the issues of minimum detection limits as a function of X-ray source energy[35, 36]. The Monte Carlo code XRFCOMP has been written to perform these calculations and is available on request. Sections of the work presented in this chapter are from the co-authored material cited above and it is appropriate to acknowledge the experimental work of Mr John Turner and Miss Diana Mannering and clinical input from Dr Bridget Robinson.

The final two chapters of the thesis examine an extension of the stochastic method called the inverse Monte Carlo method and how it is used in combination with standard empirical dosimetry techniques. The aim of these is to obtain information about the particles generated from the various radiation sources in the department.

In chapter six we consider low-energy photon sources used in superficial therapy and a manner of measuring source spectra more directly than is possible with higher energy sources. Chapter seven examines the acquisition of electron beam parameters from in-phantom measurements, such as would be performed for standard dosimetry practices. Monte Carlo based dosimetry is desirable in both these circumstances[37] and incident beam information enables forward Monte Carlo calculations to be performed. Furthermore a review of methods used in the determination of X-ray spectra at supervoltage energies is presented in the Honours III project of Ms Jenny Williams[38]. All of these techniques depend on inferences relating measurements to the actual beam parameters and are, as such, inverse methods.

Superficial X-rays are generated by X-ray tubes with peak potentials of 10 through 100 kV_p. The deposition of energy is typically close to the surface of the patient and consequently this modality is used to treat shallow tumours and pterygia. Dosimetry methods used with this modality are comparable to the dosimetry of ^{125}I brachytherapy sources used to treat ocular melanoma. The small scale in which radiation of this energy is attenuated is in obvious contrast to the whole-body therapies of chapters two and three.

The dosimetry technique presented here uses spectra measured with a high-purity germanium detector[39, 40]. The conventional method of converting raw

pulse-height distributions to incident spectra is called "stripping". Here the procedure is described in terms of an inverse Monte Carlo method. Backscatter factors and depth dose curves are determined using forward Monte Carlo calculations. The results and measurement techniques are contrasted with those from the literature. The use of novel measurement techniques such as Fricke dosimetry and radiochromic film have been examined in the honours III project and the masters thesis of Mr Mark Stevens[41, 42].

Appendix one relates to material in this chapter and is a published article[43]. The article gives an overview of our radiochromic film dosimetry in superficial and brachy-therapy and describes a novel suggestion for how film densitometry might be performed at measurement scales typical to these therapies. The publication has been appended to this thesis as my contribution was significant, in particular to discussion of the research and the final form of the presentation.

The second appendix is a published article[44] describing sets of measurements performed to determine field size and source-to-surface dependence relations. Electrons tend also to deposit energy close to the surface and in many circumstances treatments may be adequately planned with output measurements and dose versus depth relationships. These parameters are field-size and source-distance dependent. I was significantly involved in discussions, measurements performed and the final form of the publication, thus warranting its inclusion.

In chapter seven we consider Monte Carlo based electron therapy dosimetry. We consider how Monte Carlo calculations might be set up in clinical circumstances using measurements performed in-phantom and on site to establish incident beam (phase-space) information[45, 46, 40]. Methods for reconstructing spectra are considered and an argument is presented for a stochastic method of inversion such as the Markov chain-Monte Carlo method[47]. Markov chains have been used extensively in statistical physics, beginning with the work of Metropolis *et al*[48].

Subsequent sections in this introduction are to be regarded as introductory material. I give a description of the equipment used, and then give a brief overview of the techniques and relevant background material for each of the main topics. It is not anticipated that this material will provide a thorough review for the reader unfamiliar with the groundwork, but rather a fresh perspective. However, an effort is made to indicate appropriate sources of review material should this be required.

1.3 Implementation

The Christchurch Oncology Service has provided a significant proportion of the resources required in this research. Much of the experimental work in this thesis has been performed on a Varian 2100C linear accelerator which has two photon modalities rated at 6 and 18 MV. The electron modalities range from 6 MeV through to 20 MeV. Other units include the recently installed 6 MV Varian 600C accelerator for which bunker radiation protection calculations were performed and a Cobalt-60 Therac treatment unit. An excellent review of the modern therapeutic linear accelerator is by Karzmark[49] and an overview can be found in Johns and Cunningham[14].

Two superficial X-ray units (Philips RT100 and RT50) and radioactive sources in the form of Iodine-125 seeds were used in the low-keV dosimetry investigations.

The majority of the computational work has been carried out using Unix operating systems. The Christchurch Oncology Service has several Silicon Graphics workstations and the Department of Physics and Astronomy has several Sun/Sparc workstations.

Several key pieces of code have been installed on these systems. EGS4[1] (Electron Gamma Shower version 4) is software distributed freely for performing Monte Carlo calculations for radiation problems ranging in energy from a few keV through to several GeV. The code is a unified set of routines for transporting either photons or electrons through media contrived as elements, compounds or mixtures.

GRATIS[50, 51] is a developmental treatment planning system. The software distribution has a number of useful applications for standard calculations performed in an oncology department. It has provided calculational support in a number of circumstances and is an appropriate platform for the development of therapy algorithms.

1.4 Radiation dosimetry

This thesis considers the dosimetry of applied radiation. It is therefore appropriate, before we proceed any further, to define radiation "dose"[14, 52]. The absorbed dose, D is defined as energy absorbed in a medium per unit mass or

$$D = \frac{\mathrm{d}E_{ab}}{\mathrm{d}m}. \tag{1.1}$$

The dose can also be constructed from a particle fluence. The fluence, Φ, is defined as the number of particles crossing a surface of unit area perpendicular

to the direction of motion. The energy fluence, Ψ, is sometimes used and this is total energy passing through a surface of unit area.

Differential fluence, $\Phi_{E,\mathbf{u}}$, is an element of fluence possessing an energy, E, and a trajectory, $\mathbf{u}$. Often it is sensible to separate a fluence into such components. When we examine a beam spectra or the in-air distribution of a point source, we are referring to a differential fluence.

When a particle interacts with the medium, it does so with probability per unit length, μ, and $1/\mu$ is the mean free path between interactions. If $\overline{E}_{ab}$ is the mean energy absorbed by the medium, then the absorbed dose is defined as

$$D = \Phi \left(\frac{\mu}{\rho} \right) \overline{E}_{ab}. \tag{1.2}$$

Dose can also be calculated from the divergence of the vectorial energy fluence,Ψ[53], and is the manner in which the fluence transport equation is used to generate analytic models of dose distribution.

$$\begin{aligned} D(\mathbf{x}) &= -\frac{1}{\rho(\mathbf{x})} \nabla \cdot \Psi \\ \text{where } \Psi &= \int_{4\pi} \int_{0}^{\infty} \Phi_{E,\mathbf{u}} E \mathrm{d}E \mathrm{d}\mathbf{u} \end{aligned} \tag{1.3}$$

1.5 Total skin electron therapy

A therapy technique has been implemented at the Christchurch Oncology Service for treating the skin lymphoma mycosis fungoides[54] with low energy electrons arranged in a large field[55]. The method is a variation of the original Karzmark or Stanford technique[56, 57, 58]. The patient stands in a frame positioned at an extended source-to-skin distance (SSD). The divergence of the beam and a specially designed degrader conspire to provide a uniform beam front and to reduce the energy of the source electrons[59]. The patient adopts six different orientations and, in this manner, the dose is distributed evenly about the skin surface, sparing the internal structures.

The method presented here is an alternative to an 8 field technique[60, 61] and the original 12 field prone/supine technique performed at Christchurch Hospital[62].

Electrons tend to deposit dose close to the surface, although the highest electron modality (20 MeV) available at the Christchurch Oncology Service has a range of approximately 10 cm. The advantage that electrons have over other radiations is the very abrupt fall off in dose beyond the dose maximum.

This is useful for therapies where treatment is required to a particular depth, for example, if a tumour overlies a sensitive organ. Treatment planning for electrons is typically rudimentary. This is due, in part, to the complexity of electron transport and in particular, their propensity to scatter. However, because electron therapies are often orientated about the surface a lot of information can generally be obtained by standard dosimetry measurements. The dosimeter of choice is the parallel plate chamber[63, 64, 2]. The large fields employed in this technique mean that consideration needs to be taken of the induction of charge in the ionisation-chamber cable[65, 63]. Film and thermoluminescent dosimeters (TLD) are also used and, again, electron dosimetry requires special considerations[66, 67].

1.6 Total body irradiation

The total body irradiation technique is used in conjunction with bone marrow transplant[68] to facilitate the treatment of several haemopoietic malignancies, including leukemia. A method devised at the Christchurch Oncology Service uses 6 MV X-rays and a moving gantry to sweep a wide beam across the patient. The patient lies in the prone and supine positions at a point of extended SSD. Variation in the length of a ray from the accelerator to the patient can be compensated by varying the accelerator output. The modern, computer controlled, accelerator is capable of modulated therapies. A conformal therapy[69] would provide an optimally uniform dose distribution to the midline of the patient.

The method has a number of advantages over other arrangements of patient and beam, in particular, the prone/supine method of irradiation which keeps the variation in beam path through the body of the patient to minimum. A 6 MV modality is desirable in these circumstances.

Quast[70] and Gerig *et al*[71] describe a therapy that incorporates a specially designed moving couch. The arrangement of a moving patient is not always desirable and care must be taken that the motion of the couch is locked to the output rate of the accelerator. There is also the issue of patient comfort. Pla *et al* [3] used a head mounted gantry and were able to use a rotational axis of around 2 metres. With arc-mode on a centrally mounted accelerator, the beam must be passed beyond the isocentre with an effective axis of rotation of only 1 metre. We show, however, that with a small degree of output compensation at the extremities we can produce a distribution that is, at least, equivalent to that of a head mounted gantry.

The work divides into several sections. Firstly a series of measurements

including tissue-maximum ratios were performed to analyse the dose distribution associated with the arced field. An external control system was devised to alter the dose output in the appropriate manner. This exercise was performed in anticipation of the appropriate software control being installed on the accelerator and can be regarded as a feasibility study.

Monte Carlo methods have been used to examine aspects of dose uniformity and resolution with extended field sizes, the details of which are described in the masters thesis of Peter Love[30]. A mathematical anthropomorphic model is used to examine the effects of lung disequilibrium[72, 73] and oblique incidences[74, 75, 76, 77] at the extremities of a patient.

The Christchurch Oncology Service has recently acquired the software to enable full internal software control. A preliminary study is carried out and includes details of the creation of segmented treatment tables for use with the Varian dynamic therapy toolbox[78].

1.7 Monte Carlo methods in radiotherapy treatment planning

As a substantial proportion of this thesis is devoted to Monte Carlo calculations, it is appropriate to provide a brief review of this method, particularly as it is applied in medical radiation physics. The reader is referred to several other useful texts[79, 80, 81, 82]. The EGS4 suite[1, 83] is the code upon which the Monte Carlo calculations presented in this thesis are based. It is distributed with substantial documentation including tutorial exercises and detailed descriptions of the physical implementation. EGS4 has been tested on a wide variety of computer platforms. Comparisons of EGS4 performances for various architectures are published for comparison[23] and a web site is continually updated with the performances of new systems.

Monte Carlo methods are now on the brink of being introduced to routine therapy planning[37]. Certainly, Monte Carlo presently plays a large part "in the wings". In circumstances where an aspect of a therapy dosimetry can be pre-calculated, Monte Carlo is very useful. Examples in this thesis of pre-planning calculations include the determination of backscattor factors and depth-dose relationships in homogeneous phantoms. Increasingly, the results of Monte Carlo calculations are being used as input data to treatment planning systems.

Several issues must be carefully addressed. Is the physics right (yet)? Are we sure this is what the beam looks like? Do we know the composition of

our patient? With respect to the first question, EGS4 has the advantage that many workers use it, that it is constantly criticised[84, 85, 86, 87, 88] and that it is continually revised[89, 90, 91, 92, 93, 94, 95]. The citations given here will hopefully give the reader an idea of the scale of the undertaking, with each new revision catering for an increasingly subtle aspect of the physics.

The second question is one that will be addressed specifically in chapters six and seven. When Monte Carlo is used in computational physics we have to know information about the initial properties of the system and here in terms of the fundamental properties of the particles, energy and trajectory. Usually the most appropriate way to determine these quantities is via experiment.

The final question is not generally addressed in a therapy context however tremendous progress is being made in the world of diagnostic medicine and due, as with advances in radiation therapy planning, to fast electronics and fast computers.

A CT scanner images electron density due to the predominance of Compton scatter and the photoelectric effect at diagnostic X-ray energies. Magnetic Resonance Imaging (MRI) continues to improve from the earliest work[96]. The selective excitations of hydrogen nuclei in a magnetic field and their subsequent decay enable us to measure the density of this element in the body. In terms of Monte Carlo based radiotherapy planning it is desirable to know the concentrations of all the elements *in vivo* or at least have some way of arriving at an effective atomic number[97, 98]. We are certainly a long way from scanning elemental compositions.

A step in the right direction is perhaps the *in vivo* x-ray fluorescence technique of chapter five. Several workers acknowledge the potential for the use of XRF in the imaging of bulk medium-Z materials[99, 100].

1.7.1 The structure of EGS4

EGS4 is a Fortran based, electron and photon transport, Monte Carlo code. The routines making up the package are coded in Mortran[101], a macro extension to Fortran-77. Macros are used as a faster method of coding frequently called geometry routines and the random number generator.

EGS4 is comprised of internal and user orientated routines. There are three user oriented routines which are modified by the user from one problem to the next and are are collectively referred to as the user-code.

Figure 1.1 illustrates the relationship of the three user control routines MAIN, AUSGAB and HOWFAR to the inbuilt physics routines. MAIN contains initialisations including the initial particle trajectories. One call to SHOWER

is performed per particle history. AUSGAB is called whenever an interaction occurs and perhaps energy is to be deposited. HOWFAR is called whenever the routines need to determine the distance to a boundary where transport conditions will change.

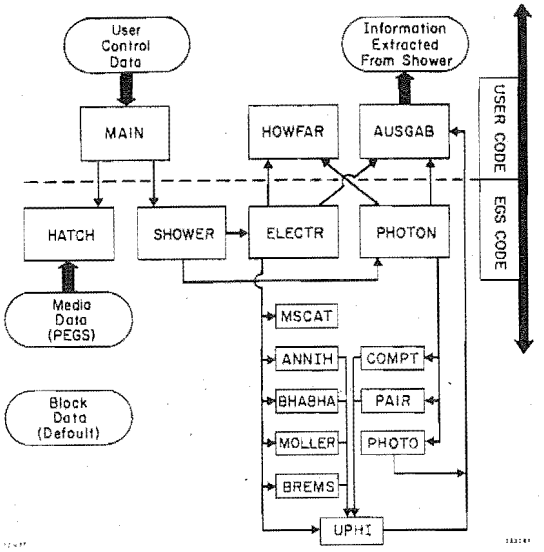

Figure 1.1: Structure of EGS4 showing the distinction between user and internal subroutines and flow of the program and data. From Nelson *et al* 1985[1].

The EGS4 internal routines deal with specific elements of the particle transport. Standard EGS4 contains algorithms for photons to determine the consequences of Compton scatter (COMPT), the photoelectric effect (PHOTO) and pair production (PAIR). For electrons bremsstrahlung (BREM), Möller scatter (MOLLER), Bhabha scattering (BHABHA), annihilation events (ANNIH) and multiscattering/ condensed history steps (MSCAT) are considered. The reader with interest in this package is encouraged to read the EGS4 manual[1], containing a good deal of information on the implementation of these interactions.

The routine UPHI stands for uniform phi distribution and deals with the regeneration of particle trajectories.

Arrays containing tables of relevant data are generated by the EGS4 preprocessing package (PEGS4). Tables for single element media, mixtures and compounds can be generated of arbitrary density. PEGS4 generates cross-sectional data and the HATCH routine places this data in accessible arrays for the EGS4 photon and electron interaction routines to use. Recent additions to EGS4 are incorporated in this thesis. This includes extensions written at

KEK - the high energy physics facility in Japan[93, 94, 102, 95]. The additions deal with transport in the low keV range of energy and include corrections to Compton scattering to include a linear polarisation term, bound Compton scattering and Doppler broadening.

1.7.2 Random number generators

The Monte Carlo method is a statistical sampling technique formally equivalent to integration[81]. The method relies on the generation of unbiased sets of random numbers. Unfortunately the generation of random numbers has evolved into somewhat of a black science and the history of Monte Carlo methods is potted with instances of calculated effects that have been shown, in the end, to be due to a quirk in the mode of generation[103, 104]. Since random number generators depend on the computer hardware, it is necessary to understand certain aspects of their implementation.

A *truly random* sequence can only be generated by a random physical process. Possible methods include the measurement of thermal noise or decay processes. Frigerio and Clark[105] describe a method where alpha decay events are counted over a fixed time period. An odd or even count would generate a zero or one bit. The disadvantage of such methods is the limited rate at which the random digits are produced. This is particularly problematic, given that computer processing speeds are upwardly mobile. It is not infeasible that millions of floating point numbers will need to be generated per second for routine radiotherapy calculations.

A computational method will generate, what is referred to as, a *pseudo-random* number sequence. There are several popular algorithmic methods for generating long sequence sets of random numbers, suitable for radiation physics problems. While such an algorithm will not give a purely random number, it is sufficient to demonstrate that the set is uniformly distributed over the range of possible values.

One further class is the *quasi-random* number generator. In this method no attempt is made to acquire a random sequence and here a sufficient condition is that the numbers are uniformly distributed and that they can take any value within the sampled domain. The method when applied to problems of integration is therefore somewhere between Monte Carlo and numerical quadrature techniques.

The advantage that Monte Carlo and "*quasi*-Monte Carlo" have over standard numerical integration techniques is that they avoid the pre-selection of a grid (or a regular distribution of sample points). For problems in small

numbers of dimensions, standard integration techniques such as the trapezoid method are clearly more efficient than Monte Carlo methods. However, in higher dimensions random distributions lead to faster convergence than regular distributions. This is due to the size of the volumes traced out by even relatively close grid points which, in hyper-dimensions, leave substantial volumes of the function domain unsampled. With a uniform sampling method no such biasing occurs. Monte Carlo methods applied to a high dimensional problem may also require substantial sampling but if the information sought is a projection of the sampling domain into a lower dimension, then convergence occurs quickly and is a reflection of the coherency of the problem.

The radiation transport problem is one of high dimension. This is apparent given the number of independent parameters and sampled distributions that influence the flight of a particle. It is intuitively obvious that a random sampling method will be a successful method for simulating a random process. Conversely, in the limit of a large number of particle histories, we can use the Monte Carlo method to solve the radiative transport equation. More will be said about this shortly.

1.7.3 Random number generators in EGS4

Two methods of random number generation are used in this thesis. The first to be considered is the linear multiplicative linear congruential generator. It is easily implemented and is given as an example in the EGS4 tutorials. A random number, ξ_i, may be generated from

$$\xi_i = (A\xi_{i-1} + B) \pmod{M} \tag{1.4}$$

where M is tge modulus, A the multiplier and B is a constant. In the 32-bit implementation of EGS4 the following two lines of code generate each new random number.

```
IXX=IXX*663608941
R=0.5+IXX*0.23283064E-09
```

The repetition rate with this algorithm is of the order $2^{30} \approx 10^9$ and is adequate in situations where up to 10^6 particles are initiated. This generator must be initialised with an even number in the 32-bit architecture.

In much of the work presented in this thesis, a larger number of histories is desirable. A second algorithm provided with the EGS4 distribution is the lagged Fibonacci sequence. Shift register and lagged-Fibonacci generators have cycles of the order 2^{570} (approximately 10^{171}).

Initialisation procedure	Number generating call
IXX=1802	R=URNDM(IXX)-URNDM(JXX)
JXX=9373	IF(R.LT.0.) R=R+1.
I = MOD(IXX/177,177) + 2	URNDM(IXX) = R
J = MOD(IXX,177) + 2	IXX=IXX-1
K = MOD(JXX/169,178) + 1	IF(IXX.EQ.0) IXX=97
L = MOD(JXX,169)	JXX=JXX-1
DO II=1,97[	IF(JXX.EQ.0) JXX=97
S =0.0;T=0.5	CRNDM=CRNDM-CDRNDM
DO JJ=1,24[	IF(CRNDM.LT.0.) CRNDM=CRNDM+CMRNDM
M=MOD(MOD(I*J,179)*K,179)	R=R-CRNDM
I=J	IF(R.LT.0.) R=R+1.
J=K	NRANM=NRANM+1
K=M	
L=MOD(53*L+1,169)	
IF(MOD(L*M,64).GE.32) S=S+T	
T=0.5*T]	
URNDM(II)=S]	
CRNDM = 362436./16777216.	
CDRNDM = 7654321./16777216.	
CMRNDM = 16777213./16777216.	
IXX = 97	
JXX = 33	

Figure 1.2: Marsaglia long sequence lagged Fibonacci generator used in most of the Monte Carlo calculations presented in this thesis.

$$\xi_i = (\xi_{i-p} \oplus \xi_{i-q}) \pmod{M} \tag{1.5}$$

where $\oplus$ is a binary or logical operation and p and q are the lags ($p > q$).

The implementation of the lagged-Fibonacci sequence in EGS4 is rather more involved than for the linear-congruential method (see figure 1.2). The initialisation procedure establishes a table of random number values. $p = 97$ and $q = 33$ are the starting points in the table.

The call is also more involved than the multiplicative linear congruential generator and increases computation times in EGS4 by approximately 30%.

For maximum speed of execution, in EGS4, these routines are coded in the form of a macro named $RANDOMSET. When the Mortran user-code is interpretted into Fortran-77, the macro is written out in full. It is debateable whether this procedure is still necessary with a modern compiler. In-lining is

often a standard part of optimisation that occurs at compile time.

1.7.4 An argument for performing Monte Carlo on 64-bit operating systems

Marsaglia[106] describes a curious phenomenon exhibited by many *pseudo-random* number generators. The effect is that if successive d-tuples of samples are taken as coordinates of points in a d-dimensional space, that all points will lie on certain finite number of hyperplanes. The effect was described for multiplicative-congruential generators but has recently been shown to also occur in the lagged-Fibonacci generator mentioned above[107].

Marsaglia shows that the effect is related to the number of bits, t, used to generate the random number and the dimensionality of the problem. The maximum number of hyperplanes into which all sampled d-dimensional points will fall is given by $(d!2^t)^{1/d}$. For sampling in 3-dimensions, a 32-bit operating system will therefore generate points on a maximum of 2953 hyperplanes. A Monte Carlo integration, using such a generator, is no better than a numerical integration using a grid of 1000^3 points from 3 sets of 1000 intersecting planes. An easy operation in today's computing climate.

The situation for these generators worsens in higher dimensions but significant gains are made by going to longer word lengths. For example a 64-bit word length will generate a maximum of 4.8×10^6 hyperplanes equivalent to around 10^{18} grid points. This is a strong argument to adopt 64-bit architectures if Monte Carlo techniques are to be the predominant mode of computation.

1.7.5 The radiation transport equation

It is illustrative to state the radiative transport equation. The equation is not required, as such, to perform Monte Carlo calculations though the two procedures are complementary. The transport equation represents the diffusion of radiation through a fixed point in space and is an Eulerian representation. The Monte Carlo method, on the other hand, traces the history of individual particles within the system and is, in that respect, Lagrangian[108].

$$\frac{1}{\nu}\frac{\partial \psi}{\partial t} + \mathbf{u} \cdot \nabla \psi(E, \mathbf{u}, \mathbf{x}, t) = Q\psi(E, \mathbf{u}, \mathbf{x}, t) \tag{1.6}$$

is the time dependent linear Boltzmann equation where,

$$Q\psi(E, \mathbf{u}, \mathbf{x}, t) = \mu\left(\int_0^\infty \mathrm{d}E' \int_{4\pi} \mathrm{d}\mathbf{u}' \psi(E, \mathbf{u}', \mathbf{x}, t)\sigma(E' \to E, \mathbf{u}' \cdot \mathbf{u}) - \psi(\mathbf{u}, \mathbf{x}, t)\right)$$

and $\psi(E, \mathbf{u}, \mathbf{x}, t)$ is an element of particle fluence rate (flux) at time t, and position $\mathbf{x}$, with energy E, trajectory $\mathbf{u}$ and velocity ν. The particle stream interacts with the medium with a probability per unit pathlength, μ, and has scattered with probability per unit pathlength σ from a direction $\mathbf{u}'$ with energy E'.

We will, in general, maintain certain aspects of this nomenclature. In particular, the interaction probability, μ, is also called the linear attenuation coefficient. σ is called the interaction cross-section and like μ is highly dependent on the energy of the radiation and the nature of the medium.

1.8 Accelerator maze design

This sub-project of this thesis arose from a need to perform radiation protection calculations during the installation of a 6 MV accelerator in the third bunker at the Christchurch Oncology Service. A first-order, scattering technique can be used[109, 110] and this is described, however a full Monte Carlo calculation such as presented by Biggs[111] using the ITS[112] Monte Carlo code or using EGS4 as presented in this thesis, allows many of the assumptions inherent in this type of calculation to be eliminated. Consequently a higher degree of confidence can be reached than with order of magnitude calculations. Further a Monte Carlo analysis enables the assessment of coefficients of scatter inserted into these more familiar calculations.

The Monte Carlo method is widespread and provides a convenient means for oncology institutions to optimise their accelerator bunker designs. EGS4 is designed for portability over a wide range of platforms. A user-code has been written in such a way that other institutions will be able to implement this code easily. The user-code MAZE2D presented in this thesis is designed to accept a set of user inputs. The format for these inputs is described and an example provided.

At Christchurch Hospital we were interested in photon transport through the radiation bunker. However for accelerators exceeding 10 MV another process must be considered, namely the production of photon-neutrons by the (γ, n) reaction. This process has been considered by a number of workers [113, 114, 115, 116, 117, 118, 119, 120, 121, 122, 123, 124].

The elimination of these neutrons requires special considerations, for example, the 18 MV mode on the Varian 2100C accelerator has a safety interlock that ensures a set of neutron moderating doors (boron/polyethylene) are closed before beaming can occur. EGS4, as such, does not treat neutron transport. MCNP[125, 126] (Monte Carlo, Neutrons and Photons) is available for neutron

transport calculations, however, MCNP does not specifically treat the (γ, n) interaction. Clearly an all-particle framework, with a coded user interface, is the preference for a complete treatment of this problem.

1.9 Optimisation of *in-vivo* X-ray fluorescence

X-ray fluorescence is a non-invasive technique that can be used to measure concentrations of a variety of trace elements in the body[127, 128]. The technique is used extensively in geology as a non-destructive means of measuring constituents in rock. A number of medical applications have been forthcoming [129, 130, 131, 132, 133, 134], as the level of radiation required is comparable to a conventional diagnostic X-ray.

We look specifically at the uptake of the chemotherapy drug, cisplatin, as a technique to determine dosage to various organs within the body. The technique also promises spin-offs in disciplines such as pediatrics and occupational medicine. Assessment of the concentrations of trace metal toxins such as lead, cadmium and mercury would be useful in the analysis and subsequent treatment of poison uptake.

A wholesale reduction in the minimum detectable limit is obtained by polarisation of the incident X-rays [134, 135, 136, 130, 137, 138]. By appropriate positioning of the detector, we can selectively remove radiation that is not involved in the fluorescent process. Further fine tuning of the collimation and polarisation processes will lead to an improvement in sensitivity and, ultimately, a greater versatility of the method. Monte Carlo modelling is used to examine radiation transport in the set up. From this analysis, we can determine the best possible arrangement of collimators and scattering surfaces to achieve maximum possible detection efficiency thereby keeping the dose to the patient to the minimum.

The calculations presented require an extension to the conventional Monte Carlo code to cater for the influence of polarisation on the transport of Compton scattered X-rays[93, 94, 102, 95] and the fluorescence of multiple element materials[91].

1.10 Dosimetry at low energies: Superficial and brachytherapies

Techniques involving Monte Carlo methods for the determination of various treatment parameters used in superficial therapy and brachytherapy have been

developed. Photon transport calculations proceed very rapidly at these energies due to the high probability of photoelectric absorption occurring in solid materials. Photoelectrons generated under such circumstances have an extremely short range and can be considered to deposit all their energy at the site of primary interaction. Monte Carlo methods will be desirable in superficial and brachytherapy planning algorithms especially for treatments involving a high degree of tissue inhomogeneity.

Monte Carlo is used to determine dose versus depth relationships and backscatter factors for a superficial therapy device. The procedure involves the determination of spectral data measured with an energy sensitive detector[139, 140, 141]. This research is analogous to the electron spectral reconstruction work of the following section, in that a measurement technique is used to determine incident spectra which, in turn, is to be used for the determination of dosimetric qualities. In this case, the measurement is more directly related to the spectrum. None-the-less, a "true" spectrum still needs to be determined, through a process referred to as "stripping" in the literature[142, 143, 144].

In our own work a cryogenically cooled, high-purity, germanium detector system is used. The detector requires a substantial reduction in the beam fluence. This is achieved with a substantial source to detector distance and pin-hole collimation[39].

We will show that the stripping procedure is trivial example of an inverse-Monte Carlo method[145, 146].

Forward Monte Carlo calculations are performed and back-scatter factors and depth-doses determined for spectra acquired from the Philips RT100 superficial unit. The back-scatter factors are compared with the literature[14, 147, 148], including several other Monte Carlo based calculations [149, 150, 151, 152, 153]. The difficulty associated with measuring or calculating back-scatter factors is evident[154, 148, 155, 156, 157]. Central-axis depth doses are also reported in the literature[158, 14].

Monte Carlo calculations can be performed to determine dose distributions about ^{125}I seeds. In this case the source spectrum is well defined and due to the nuclear transitions we would expect to see from this isotope. Plaques of ten seeds are used in the treatment of ocular melanoma. The distribution of dose along the central axis of the plaque has been calculated using Monte Carlo calculations for a spherically symmetric geometry and a superposition method. This work is, however, incomplete and not presented. There are a number of papers discussing Monte Carlo calculations [159, 160, 161, 162, 163, 164, 165, 166, 167, 168] and empirical relations [169, 170, 171, 172, 173, 174, 175,

176]. While many workers have used complex TLD setups for experimental verification[177, 178, 179, 180] we and other groups have used radiochromic films[181, 182] and Fricke dosimetry[183, 42].

The determination of source characteristics here is trivial. Forward Monte Carlo transport through anatomical medium gives a complete system of treatment planning and is desirable for this type of radiation. A Monte Carlo method using heterogeneous tissue compositions [98, 184, 185, 186, 187, 188] is the next step and promises significant improvements on the current method.

1.11 Electron therapy planning.

Electron therapy is an increasingly popular modality. There is a growing need for improvements in electron therapy dosimetry particularly as a significant application of this type of radiation is to treatment volumes overlying or within sensitive tissues. The traditional method relies on the characterisation of two beam qualities, namely R_{50}, the depth at which the dose reaches 50% of the maximum, and R_p, the practical range[52, 3].

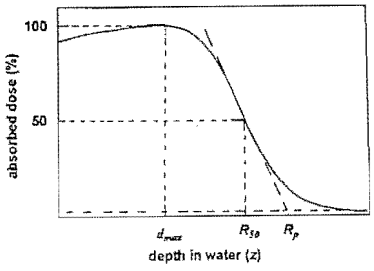

Figure 1.3: Definition of different electron range parameters. R_{50} is the range at which the absorbed dose reaches 50% of maximum dose, $d_{\max}$. R_{p} is the practical range (from IPEMB 1996[2])

Figure 1.3 shows a typical electron dose versus depth relationship (depth-dose). We see the dose initially increase with depth due to electrons back-scattering from the surface of the phantom. This effect is also described in terms of a charge equilibrium and, when forward and back scattered electrons are equal at a point in the medium, a maximum occurs, $D_{\max}$. The dose falls rapidly beyond $D_{\max}$ until such a point that all electrons have been brought to rest in the medium, i.e. the practical range. What remains is contributions from the absorbtion of bremsstrahlung radiation generated in

both the treatment head and the phantom[190, 191] and is related to the radiative stopping power of the incident electrons.

Electrons and positrons interact very strongly with the medium. The interactions are Coulombic[192, 193, 194, 195, 108] and cause the charged particle to slow very rapidly and to scatter away from the direction of incidence. Consequently the electron and other charged particles have a finite range. An approximation to this range can be determined by considering a quantity called the stopping-power. It is a measure of the energy loss with path-length and is a function of the particle energy and of the medium.

$$\begin{aligned}(S/\rho)_{\text{tot}} &= (S/\rho)_{\text{col}} + (S/\rho)_{\text{rad}} \\ &= -\frac{1}{\rho}\frac{\mathrm{d}E}{\mathrm{d}x}\end{aligned} \tag{1.7}$$

where $(S/\rho)_{\text{tot}}$ is the total stopping power for electrons, which is a sum of the collisional stopping power $(S/\rho)_{\text{col}}$ and the radiative stopping power $(S/\rho)_{\text{rad}}$. Stopping powers are tabulated[52]. Their derivation from theory is described in some detail in the EGS4 manual[1], ICRU report 35[52] and references therein.

The practice of dividing through by the density of the medium, ρ, is a reflection of the strong influence that the density has on the range but also this practice helps to maintain a regularity to the values of stopping powers over a wide range of material densities.

If an electron is assumed to lose energy in a continuous fashion as it travels through the medium, starting with an initial energy, E_0, then the average range of the particle, r_0, is

$$r_0 = \int_0^{E_0} \left(\frac{S(E)}{\rho}\right)^{-1}_{\text{tot}} \mathrm{d}E. \tag{1.8}$$

This result is the continuous slowing down approximation. r_0 is called the **csda** range. We have mentioned that an electron is quickly scattered away from its incident trajectory, therefore we would expect the **csda** range to be somewhat larger than the range in a forward direction and this is indeed the case for an average electron trajectory. The range of the average electron trajectory in the medium is R_{50}. Due to a process called electron energy straggling, the electron energies are distributed above and below that determined by the continuous slowing down approximation. Consequently, it is possible that some electrons will travel further than the **csda** range. The difference between the practical range and the **csda** range is therefore representative of the degree of energy straggling that occurs.

With heavy charged particles such as protons, the straggling and scatter are less. Heavy particles lose a smaller proportion of their energy per interaction with atomic electrons, consequently they interact many more times before stopping. Paradoxically the greater number of interactions leads to less straggling because the total energy loss is closer to the average. The consequence is that most of the energy is deposited at the end of the range. This is the origin of the so called "Bragg peak"[196, 197, 198].

Several empirical relationships relate the energy of the beam to the range related parameters. For example, ICRU recommends the formula

$$\bar{E}_0 = 2.33\,\mathrm{MeV\ cm^{-1}} R_{50}, \tag{1.9}$$

in the energy range 5 MeV$< \bar{E}_0 <$ 35 MeV, where $\bar{E}_0$ is the average energy of the beam at the surface.

The practical range, R_p, is often considered to be a better indicator of beam voltage.

$$E_{p,0} = 1.95\mathrm{MeV\ cm^{-1}} R_p + .48\mathrm{MeV}, \tag{1.10}$$

where $E_{p.0}$ is the most probable energy at the surface. The equation is applicable in a similar range to the above (from ICRU35[52] see also the IPEMB electron dosimetry code of practice, 1996[2] for recent revisions to these relations).

A measure of the rate at which electrons are deflected from an initial trajectory is expressed in the mass scattering power,

$$\left(\frac{T}{\rho}\right) = \frac{1}{\rho}\frac{\mathrm{d}\bar{\theta}^2}{\mathrm{d}l}, \tag{1.11}$$

where $\mathrm{d}\bar{\theta}^2$ is a small change in the mean square scattering angle. Mass scattering power and its integral along a particle trajectory (the mean square scatter) provide us with a convenient measure of the scatter away from the normal.

Mass stopping and scattering powers have been examined for electron range calculations[199, 200, 201]. The reader is also referred to chapter 21 of Evans[202].

1.12 Stochastic methods in electron therapy dosimetry

In chapter seven we examine the determination of electron beam spectra and angular distributions (essentially, phase-space information) from in-phantom measurements. An inverse-Monte Carlo method is proposed and for reasons

of problem dimensionality it is argued that the inverse method is most easily implemented as a Markov-Chain Monte Carlo method[47, 203].

The inverse method is the complement of most current research. Forward Monte Carlo has been applied, with impressive results, to the processes of collimation, attenuation and scatter in the interior of the accelerator head[204, 205, 206] (see also Ebert *et al*[207] for a recent review). In some cases, however, the parameters necessary for Monte Carlo-based treatment planning may be obtained more quickly and accurately using numerical deconvolution techniques and readily available depth-dose and profile data. Here we examine such techniques.

The OMEGA project (Ottawa/Madison Electron Photon Algorithm) and their code extension to EGS4, BEAM[206], enables a physicist to enter the design parameters of the accelerator head and applicators and to perform a detailed Monte Carlo calculation to determine the nature of the incident beam. With such a detailed approach, the question one might ask is "when do I make a measurement?"

Dosimetry is a measurement science and one that impinges on public health. Clearly efforts need to be made to bring these rather disparate viewpoints to a middle-ground.

Chapter seven demonstrates several interesting results including the discovery of a dual energy effect in an earlier version of the Varian 2100C electron applicator cones. This finding has been confirmed in a recent paper examining collimator effects in Varian machines[208].

The Markov method is applied to a fictitious beam comprised of two monoenergetic components of 9 and 11 MeV. A depth dose is determined for the beam and analysed. We demonstrate how the method is able to resolve the components to a degree that relates to the type and the accuracy of the measurement performed.

Finally, we look at determining the electron spectrum and other influential parameters, such as the angular distribution, more precisely from in-phantom measurements and the analysis of two- and three-dimensional dose distributions. Radiochromic film and the Fricke dosimetry technique are both investigated as a means to obtain unperturbed dose distributions.

1.13 Future research.

Radiation oncology is a technology orientated discipline. The modern computer controlled accelerator is capable of complex, pre-programmed therapy procedures. The Christchurch Oncology Service now has a fully automated

6 MV Varian 600C accelerator. The compensated arc procedure[29] described here is an example of the way institutions in the future may well choose to perform large field therapies.

Faster computers will lead to more sophisticated algorithms. Monte Carlo methods, for example, are now an integral part of dosimetry. With computer power ever increasing it is now possible to perform more accurate and more detailed Monte Carlo simulations in a rapid time frame. Hence the potential for real-time treatment planning. It is expected that this sort of technology will be implemented over the next few years[37].

Equally impressive are various technology related trends in micro- and macro-dosimetry practices[209] such as the use of radiochromic films[43](see appendix one) and Fricke dosimetry[183]. Such advancements in measurement and calculation methods mean that many previously unanswered questions in radiation-biology are now being examined[210, 211, 212, 213].

Chapter 2

Total skin electron therapy at two energies on a linear accelerator

2.1 Introduction

Mycosis fungoides[54] is a T-cell type lymphoma which initially appears as an eczematous-type skin rash. As the disease progresses skin tumours develop with lymph node enlargement and spread to visceral organs. Topical therapy can include corticosteroids, nitrogen mustard and PUVA but the most effective treatment is Total Skin Electron Therapy or TSET[57, 214].

Low energy electrons (< 4 MeV) at an extended source-skin distance (SSD) are the modality of choice because of the rapid fall off of dose with depth and the large field size that is possible. The large field size at an extended SSD avoids difficult and time consuming field abutting procedures. The X-ray contamination should be minimal and there should be little regional variation of energy. A high dose rate is required in order to treat the patient at 3 to 4 metres SSD in the time that a conventional field would be treated at the isocentre.

For TSET, field flatness of $\pm$ 5% or better is recommended in order to achieve a uniform dose distribution over the patient[58]. In order to achieve a flat profile in the vertical axis two beams may be combined such that the 50% point of one beam overlaps the 50% point of another[58, 215]. This method is a variation of the original Karzmark technique[56].

In this centre a 12 field technique had been employed with the previous Clinic 6 linear accelerator[62] but the technique was very slow and required multiple field abutting.

2.2 Treatment technique

The method that we have adopted has been described in many previous publications[57, 60, 58] and summarised in the AAPM report 23 of the Task Group 30 Radiation Therapy Committee[214].

Figure 2.1 illustrates the positioning of the patient at an extended SSD in order to obtain uniform coverage. The patient is positioned behind a vertically placed energy degrading screen. The screen is supported in a wooden frame which is used for both support of phantoms and dosimeters as in figure 2.2. The composite dose distribution from the 2 beams (later referred to as a "beam pair") is repeated every 60° by rotation of the phantom or patient. An alternative (more uniform) technique involves 8 fields [60, 61]. However, the extra fields mean increased patient set up time and also results in a greater bremsstrahlung contamination. The patient poses in the six characteristic positions of the technique[214]. Six, 60°, beam entry points are transferred to the patient from a previously measured umbilical contour. The beam height (axis of a beam pair) is dictated by the accelerator in the horizontal (gantry angle = 90°) position. Six beam pairs are applied over a two day cycle. Day one, anterior and two posterior obliques; day two, posterior and two anterior obliques.

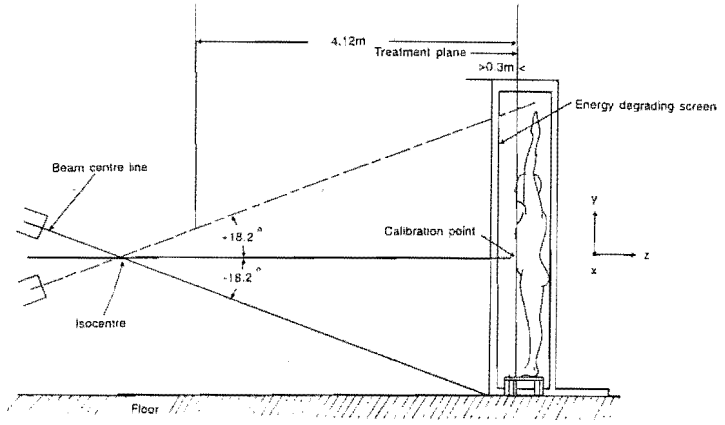

Figure 2.1: Geometrical arrangement of the symmetrical dual-field treatment technique. Equal exposures are given with each beam. The calibration point dose is at(x=0, y=0) in the treatment plane.

The patient holds onto handles (not shown) on the sides of the frame, has protective lead/acrylic shields over the eyes and nails and stands on a raised platform. The time for each field is short (< 1 minute) using the Varian 2100c high dose rate option and because no time consuming field matching is required.

The Varian 2100c accelerator incorporates a purpose designed, high dose rate, 6 MeV modality (high density total-skin electrons or HDTSe) in response

to the suggestions of previous workers[58] and the recommendations of the AAPM Task Group 30 Radiation Therapy Committee [214]. The dose rate at the isocentre is approximately 23 Gy/min corresponding to a dose rate behind the screen at 4.2 metres of 273 cGy/min, which is the same order of dose rate (240-320 cGy/min) used at the isocentre for normal operating mode. The 6 MeV (nominal) beam is from the same source, however, the shape of the beam is quite different since no applicator is employed (figure 2.3).

2.3 Materials and methods

From study of the literature it is apparent that the physics measurements necessary before proceding with any patient treatments at our centre would be as follows :

1. Beam flatness from a two-dimensional matrix of point measurements.
2. Energy variation over the same matrix of points.
3. X-ray contamination over the same matrix of points.
4. Absolute calibration at a reference point and specified depth.
5. Dose distribution in circular and anthropomorphic phantoms.
6. Calculation from 5 of an *overlap factor*.
7. Validation of use of solid water[216] (manufactured by Radiation Measurements Incorporated) phantom material for items 2, 3 and 4.

2.3.1 Arrangement for phantom measurements and patient treatments

Figure 2.2 illustrates the TSET frame that is used to both support the large 120 cm by 240 cm perspex beam degrader and also act as a positioning platform and arm support for the patient. Also shown is the phantom support shelf that is necessary to support the phantoms and ionisation chamber in a large number of positions to obtain a two-dimensional array of dose measurements. The TSET frame is constructed entirely from wood; metal has been avoided to prevent the generation of X-rays. It was also necessary to temporarily move an in-room TV monitor for this reason and also to protect the electronics from the high electron flux.

All measurements have been made with a parallel-plate (Markus) ionisation chamber connected to an electrometer with dual polarity function(Nuclear Enterprises Ionex Dosemaster 2590). A parallel plate ionisation chamber is the detector of choice for electron energies below 5 MeV[217, 52]. Initial measurements made it clear to us that the reversal of polarity method to correct for the polarity effect in the ionisation chamber and leads was mandatory. Shielding of the leads with lead foil is not a practical solution, as the leads must be moved over the array, and would produce bremsstrahlung radiation.

The Markus chamber was sandwiched between two 10 mm sheets of perspex such that the top surface (the effective point of measurement) was flush with the top surface of the perspex (figure 2.4). The detector block could then be embedded between sheets of solid water to accommodate a range of positionings from the surface to 120 mm depth.

The solid water/perspex/Markus chamber arrangement was supported in preselected positions in a two-dimensional array (figure 2.2). Field flatness and depth ionisation (including the subsequent parameters derived from this e.g. X-ray contamination) were examined over this array. The measurements were made over an area 180 cm by 80 cm firstly with a single beam and then with "beam pairs" in order to establish the optimum gantry angle from the horizontal to get the flattest vertical profile.

It was decided that the TSET facility would be available at two energies to cater for the different clinical requirements. We performed preliminary depth dose measurements for a single beam in order to decide upon the degrader thicknesses. The measurements in this study were all performed with 6 mm and 10 mm thickness perspex beam degraders.

The water equivalence of Solid Water for electrons emerging from the degrading screen was checked and any effect on the absolute calibration noted. We used a water tank at the isocentre and an energy degrading perspex screen to reduce the mean energy E_0 to midway between the two energies used for TSET. A Therados RFA-7 dosimetry scanning system was used to move the Markus chamber in the water bath. Great care was taken to position the chamber at the surface and an accuracy of 0.25 mm was achieved with this method. The water was emptied from the tank and the Solid Water positioned at 100 cm SSD. The chamber protective cap was removed and measurements at increasing depth were made by the usual method, maintaining a fixed SSD throughout the procedure. Depth ionisation data was converted to depth dose data by applying stopping power ratios for water to air [52, 217].

It was felt inadvisable to perform these latter isocentric measurements at a higher exposure rate, so the Varian High Dose Rate applicator interlock was

overidden enabling the conditions for 6 MeV at conventional (240 cGy/min) exposure rates to be set while still being in the Varian HDTSe mode.

2.3.2 Absolute dosimetry, depth dose and X-ray contamination

We have adopted the IAEA dosimetry protocol which has been adapted for Australasia by the National Radiation Laboratory at Christchurch, New Zealand[217]. The calibration was performed with a single beam in the horizontal position using the Solid Water/perspex/Markus chamber arrangement (figure 2.4). The perspex is the same material as the chamber as recommended[65] and only contributes to backscatter and some side scatter. We assume (from comparison measurements with a cylindrical chamber at 6 MeV and above) that the 2 cm thickness of perspex does not exhibit significant charge trapping effects[66]. The build-up material is Solid Water which we have shown to be equivalent to water for the energy range used in this application. The calibration depths were 2 mm and 4 mm corresponding to 2.5 MeV and 3.5 Mev respectively for the 10 mm and 6 mm degraders.

The absorbed dose in water according to the IAEA protocol is

$$\begin{aligned} D(w) &= M_u N_D S_{\mathrm{w,air}} p_u p_{\mathrm{cel}}, \\ \text{where } M_u &= \frac{M_u^0}{\mathrm{MU}} F_{\mathrm{TP}} p_s F_{\mathrm{sw}}, \end{aligned} \tag{2.1}$$

M_u^0 is the ionisation reading per monitor unit (MU), N_D is the chamber calibration (Gy/unit ionisation) and $S_{\mathrm{w,air}}$ is the stopping power ratio, water to air.

The calibration factor for the Markus chamber (N_D) had previously been found by performing a high energy (20 MeV) intercomparison with a calibrated cylindrical chamber[64, 63]. The cylindrical chamber calibration is traceable to an international standard through the National Radiation Laboratory (NRL) in New Zealand.

The factors p_s (the recombination correction factor) and $\mathrm{F_{sw}}$ (the solid water to water correction factor) are unity. The perturbation factors p_u and p_{cel} are both assumed to be unity for the parallel plate chamber as stated in the IAEA protocol[217]. The Markus chamber has a smaller guard ring compared with other similiar chambers e.g. 0.7 mm against 3.2 mm and 5 mm for the NACP and Holt/Memorial chambers. It is therefore possible the the perturbation correction may not be unity, but since we have been well within 0.5% of absorbed dose determinations at 6 MeV with a cylindrical chamber (with a perturbation correction applied) it is not expected to be an error more

than 1%[218]. Care should be taken with the perturbation correction although many workers' values for this factor are at variance in the low energy range[64].

Measurements were performed at -250 volts and +250 volts for absolute dosimetry and depth ionisation curves, and our work confirms that of others [65, 63] that the dual polarity measurements are critical. The IAEA protocol requires use of either depth ionisation or depth dose but at 2.5 and 3.5 MeV they are very similar. The energy and significance of the X-ray contamination was measured from the tail of the measured depth dose curves according to the accepted method[52].

The fact that the six beam pairs overlap one another at the skin surface has the effect of *increasing* the average skin dose compared with the calibration dose from a single beam pair. The ratio of average skin dose to calibration dose, which we have termed the overlap factor R_{ov} in a later section, is probably the most significant factor of all.

Some institutions[219] have examined the variation in this ratio over a range of cylindrical dimensions. However, by and large, most have ignored the increased dose that will be apparent for wrists, ankles and fingers where the radii are approaching that of the electron practical range.

2.3.3 Multiple field measurements

The purpose of these measurements was:

1. To investigate and quantify the regional distribution of dose over curved surfaces with 6 beam pairs.

2. To relate the resultant treatment skin dose (with six field pairs) to the calibration dose in solid Water.

3. To investigate the effective depth dose for multiple fields.

4. To investigate the regional distribution of dose over a humanoid type phantom.

Several different types of phantom were employed including regular cylindrical phantoms and an anthropomorphic phantom. Film and lithium fluoride thermoluminescent dosimeters (TLD) were used in a complementary way. The TLD were prepared by batching into six sensitivity groups in order to improve the reproducibility. The batching procedure produced a "research" group of dosimeters with a reproducibility better than $\pm 3\%$ (2SD) which we used for this work.

A 30 cm diameter regular phantom was supported centrally and edge-on to a beam pair or single horizontal beam to simulate the regional distribution of dose about a patient trunk. Film and lithium fluoride TLD were used, following a similar method employed by Cox et al[58]. The phantom consisted of two slabs of cylindrically shaped perspex blocks with a piece of wrapped X-omat V film sandwiched in between (figure 2.5). The film-in-packet was cut flush with the circumference of the phantom and resealed with light-fast tape. 3 mm by 3 mm by 1 mm TLD chips were sealed in polyethylene and placed around the circumference covered with a 1 mm layer of wax. It was predicted that the dose maximum for multiple field irradiation conditions would occur somewhere between the surface and 2 mm depth.

We also performed measurements with similar phantoms of different diameters corresponding approximately to the upper thigh (15 cm diameter) and ankles/arms (7.5 cm).

The TLD results were used both to assess the fall off of dose between fields and the factor to be used for the ratio of treatment skin dose to calibration dose. Thus an absolute calibration for the TLD was not required but was performed for later film calibration measurements.

Film was used to determine depth doses from multiple beams[67]. Three, four and six beam pairs were employed (the major contribution at any given point is from three). Between each irradiation of a single beam or a beam pair the phantom was rotated through 60°.

In an attempt to reduce measurement errors associated with re-positioning the phantom, we also exposed the cylinder to a single horizontal beam in the same orientation as for the multiple beam exposures. The single beam data was used to simulate multiple beam data by performing a simple convolution of the beam data set in six orientations. The vertical position of the cylinder was slightly off-axis to suppress problems such as "tunneling"[52].

A Therados RFA-7 scanning densitometer was employed to obtain depth doses from the film data. Although film was not used for absolute measurements we were able initially to relate a dose from the TLD, which was calibrated by placing several dosimeters at the calibration position (figure 2.4) and comparing this dose with the absolute dose measured with the Markus chamber for a single beam. With the appropriate correction to the film data we found that the single beam depth dose from the film matched very well with the single beam data from the ionisation measurements with the Markus chamber.

Measurements were also made over an anthropomorphic phantom (the RMI rando phantom) using TLD and a Markus chamber. Forty-three lithium fluo-

ride chips were encapsulated in polyethelene and affixed to selected body regions under 1 mm wax build up (figure 2.6). The regions were chosen to include areas likely to be subject to shadowing. The lower limbs were not available, but were simulated with cylindrical wooden poles. In retrospect these measurements failed to account for the increased dose to lower limbs due to the large radial dependence highlighted in this study.

2.4 Results

To investigate the importance of the polarity effect we irradiated varying lengths of cable and positioned the chamber at various depths. The magnitude of this effect is described by $(Q_+ - \tilde{Q})/\tilde{Q}$ where Q_+ is the charge measured at +250 volts and $\tilde{Q}$ is the average of charge measurements at both +250 and -250 volts. For the horizontal profile measurement at matrix position (0,0) the polarity effect was 12% while beyond the electron practical range the polarity effect accounts for the greater proportion, 85%. of charge accumulated. We conclude that it is not sufficient to calculate a single polarity correction factor, but one must always take the average of ionisation measurements at both negative and positive polarities.

2.4.1 Field flatness and beam angulation

AAPM report 23[214] suggests $\pm 20°$ for the beam tilt in order to obtain a flat field. An iterative approach was used to determine the optimum angle for the dual beams to give the most uniform profile. A first approximation to the angle was determined by examining the profile for a single beam then applying an appropriate projection. This is similar to a method used by Almond[215]. After adjustment 18.2° was found to be the optimum angle of tilt (figure 2.7).

The variation in dose at the treatment plane resulting from this dual beam arrangement is represented in figure 2.8. The flatness from the combined beam is $\pm$ 2% over the vertical height 1.60 m and $\pm$ 5% over the increased height of 1.80 m (the height suggested by Cox et al[58] who have refined this technique.) A matrix of relative point doses was obtained over a number of sessions. For each point 12 measurements have in fact been made, as each of the dual beams require three averaged measurements at each polarity. The recommendations of Cox et al are well within the AAPM recommendations.

2.4.2 Depth doses and energy variation

The perspex energy degrading screen serves the purpose of both reducing the mean energy (E_0) of the beam and scattering the beam to improve the uniformity. Using the arrangement shown in figures 2.2 and 2.4 we obtained depth ionisation curves in Solid Water at the origin of the screen and at several other sites to investigate any possible regional variation of energy. We did not investigate the effect of the screen at closer distances to the accelerator.

The corrected depth doses in Solid Water for the two different thicknesses of screen are shown in figure 2.9 with the derived mean energies at the surface of the phantom. These curves correspond to the combined effect of two angulated beams (18.2°), they were repeated for single horizontal beams and the difference in % ionisation found to be insignificant. The single beam has an R_{50} increase of less than 0.2 mm resulting in less than a 2% error in energy. The horizontal beam data was later used to determine the position of dose maximum (the calibration depth) for the absolute calibration.

The regional variation of energy is acceptably small and will have little effect on the dosimetry. Variation in R_{50} with angle accounts for ±2% variation in effective energy. If we combine this with the effect of oblique transmission through the degrader the overall effect is around ±4%. However this translates to less than 0.1% variation in the stopping power and the effect can be neglected.

2.4.3 Absolute dose measurement

The calibration depths were 2 mm and 4 mm respectively corresponding to a practical thickness of solid water which is close to the real dose maxima obtained from the depth ionisation data in figure 2.10 (dots) for a single horizontal beam. The dose was measured with the Markus chamber at the $(0, 0)$ position. For the 10 mm degrader the mean energy of the beam (E_0) in this mode was 2.55 MeV and the practical range (R_p) was 15.6 mm. For the 6 mm beam E_0 = 3.45 MeV and R_p = 19.5 mm.

2.4.4 X-ray contamination

AAPM report 23[214] recommends an X-ray background of the order of 1%. The technique of angled beams reduces the total X-ray contamination at the centre (x,y)=(0.0) because the main bremsstrahlung component is on the central axis of the beam. In circumstances where the bremsstrahlung

is large a more rigorous method is recommended to determine the absolute dose[157, 220, 191].

We measure the X-ray contamination to be 0.7% at (0,0) rising to 1.2% at (0,+90 cm) and 1.1% at (0,-90 cm). This is consistent with a value of 1.2% at (0,0) for a single beam (central axis value). The HVL in solid water suggests a mean energy of 0.6 ± 0.1 MeV.

2.4.5 Surface variation and depth doses using cylindrical phantoms and an anthropomorphic phantom

Highly oblique incident electrons will deposit a greater proportion of dose at the surface[221]. It is therefore necessary to quantify the variation of surface dose with angle.

Figure 2.11 shows the surface dose variation for six beam pairs of low energy electrons (2.55 MeV) with a dose variation of less than $\pm 3\%$, with the troughs located at a point midway between each field. It is important to identify variation aside from the uncertainty inherent in the TLD readings. This was done by performing a sinusoidal fit to the data.

Earlier measurements were made using fewer fields. However, it became apparent that significant dose was being delivered by glancing beams (90° about the circumference) and it was therefore necessary to use at least five beams to get a realistic contribution at the minimum 30° positions.

The film data from multiple irradiations were difficult to process because the phantom surface position and the dose maximum position are so close. Figure 2.9 shows the percentage depth dose for the two treatment energies following correction for the stopping power ratio. This data was sufficient to proceed to the first patient treatment, but it was felt necessary to use a more accurate and reproducible method of obtaining depth dose for combined beams.

A set of TLD readings for a single beam (or one could use a single beam pair) were mathematically convolved and shown to agree with the variation and overlap factor determined by irradiating with six beams lending support to this method. Film dosimetry is much more straightforward by this method with re-positioning of the film unnecessary.

The film measurements were obtained by densitometry of film exposed in the cylindrical phantom as illustrated in figure 2.5. Figure 2.10 compares the results of several measurements. Firstly, there is a comparison for a *single horizontal beam* between depth dose measured in Solid Water with the Markus chamber (dots) and depth dose measured in the cylindrical phantom with

film. This agreement confirms that the calibration of the film is satisfactory for depth doses.

The other curves represent film results when six beams are exposed, it is important for the physicist to communicate to the oncologist the difference between this effective depth dose (which occurs in the patient situation) and the depth dose from a single beam (used for the absolute calibration only.)

Data from the cylindrical measurements enable the calculation of Overlap Factor. Both the multiple exposure and summated single exposure methods yield similar results which agree well with ionisation chamber and TLD results on the anthropomorphic phantom. The results are tabulated as follows and discussed later.

Figure 2.6 and the table presented in the next section illustrate the results from the anthropomorphic phantom and that we were clearly mislead when predicting the ankle doses. This is because a regular 15 cm cylinder failed to adequately indicate the high dose dependence on limb diameter.

Overlap factors were obtained for both degrading screens and are presented in the next section. The results show reduced dose due to shadowing in anatomical regions previously reported[54, 61]. It is important that these particular measurements be repeated for each patient for a number of dose fractions as dose in these areas tends to be sensitive to patient repositioning. We were to conclude that the patient limb positions cannot be adequately represented with a regular anthropomorphic phantom.

2.4.6 Ratio of *average skin dose* to *calibration dose* : The overlap factor

R_{ov} was calculated using calibrated TLD around the perimeter of the cylindrical phantom. The dosimeters were irradiated with six fields at 60° intervals. The average dose was taken by sampling all the TLD chips; the calibrated dose is known from the absolute measurement using the Markus chamber in Solid Water.

R_{ov} was also calculated for the anthropomorphic phantom using TLD and using the Markus chamber with a 2 mm build up cap as a calibration. The following table gives Overlap factors, R_{ov}, measured with a variety of phantoms and dosimeters. An actual patient result has been provided by Mr John Turner.

Method	Diameter	R_{ov}	
		2.5 MeV	3.5 MeV
Multiple beams	340 mm	2.4 ± 0.1	2.5 ± 0.1
Multiple beams($\times 4$)	340 mm	-	2.6 ± 0.1
Multiple beams	156 mm	2.8 ± 0.1	-
Multiple beams	75 mm	3.2 ± 0.1	-
Single beam convolution	300 mm	2.4 ± 0.1	-
Rando Phantom (TLD)	umbilicus	2.4 ± 0.1	-
Rando Phantom (Markus Chamber)	umbilicus	2.38 ± 0.02	-
Patient (TLD)	umbilicus	2.7 ± 0.2	2.8 ± 0.2
Patient (TLD)	knee	-	3.1 ± 0.2
Patient (TLD)	ankle	-	3.4 ± 0.2

2.4.7 Validation of solid water as a suitable medium for absolute calibration and reference depth dose

The Markus chamber was fitted with its protective waterproof cap and supported in a water bath. A 20 cm square piece of "clingfilm" was supported in an expanded polystyrene frame and floated on the water surface. Clingfilm removed the surface tension effect and enabled accurate positioning of the chamber with respect to the water surface.

The measurements were made at the isocentre (100 cm) in the gantry zero position at the same dose rate as for TSET at 4 metres. A 12 mm perspex degrader was affixed to the HDTSe fitting on the accelerator head. It was predicted that this thickness would provide the appropriate energy degradation caused by 4 metres of air and a 6-10 mm degrader.

The results of the intercomparison are seen in figure 2.12. The R_{50} values differ by 0.6 mm resulting in a mean surface energy (E_0) difference of less than 5% corresponding to a variation of 0.25% in stopping power and hence absolute dose.

2.4.8 Conclusion

Before proceding with total skin electron therapy (TSET) on a new accelerator, it is important to make specific measurements for this modality.

All measurements must be made at negative and positive polarity to account for the polarity effect. a polarity correction factor may be used only when the geometry of the ion chamber leads are known and reproducible i.e. for the regular QA checks of consistency of output.

The first priority should be the machine calibration at the lower mean energy (due to the energy degrading screen). We have described the application of the IAEA dosimetry protocol but whichever is used it is important that parameters such as R_{80}, R_{50} and R_p are accurately ascertained in order to be able to look up calibration factors.

The regional distribution of dose over the patient surface is optimised by computing the best vertical angle combination and making measurements over a matrix of points. A very flat field may be achieved at the screen but TLD monitoring of many patient anatomical areas is still essential. Account should be taken of the fact that certain areas of the body are not uniformly rotated; this can result in under and overdosing.

It is necessary to measure depth of ionisation at a selection of positions over the two-dimensional array both to assess the calibration depth and the degree of bremsstrahlung. Depth doses (in cylindrical phantoms) from multiple beams indicate to the clinician the effective treatment depth. This depth is not used for dosimetry purposes.

The applied treatment dose must account for an overlap factor. This relates the true average skin dose (due to beam overlap) to the calibration dose. It should be checked during treatment using TLD or diode dosimetry. Account must be taken of the fact that this factor increases for reduced diameter limbs in the vertical axis i.e. thighs and ankles: this is not true for arms which are positioned non-vertically. Part shielding (preferably with 2-3 cm of wax) is shown to be necessary for the feet, otherwise a dose exceeding 150% of the mean skin dose may result.

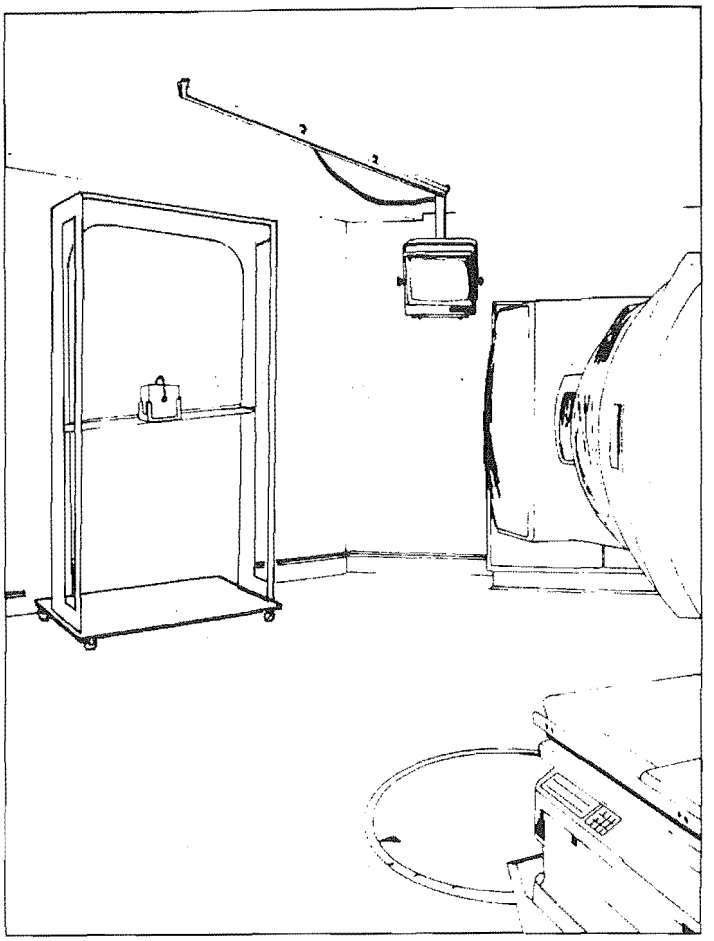

Figure 2.2: The all-wooden frame supporting the energy degrading screen. A horizontal shelf is movable vertically in 10 cm increments. The solid water phantom may be moved horizontally along the shelf which has chocks at 10 cm increments. Some modifications were added for patient treatments.

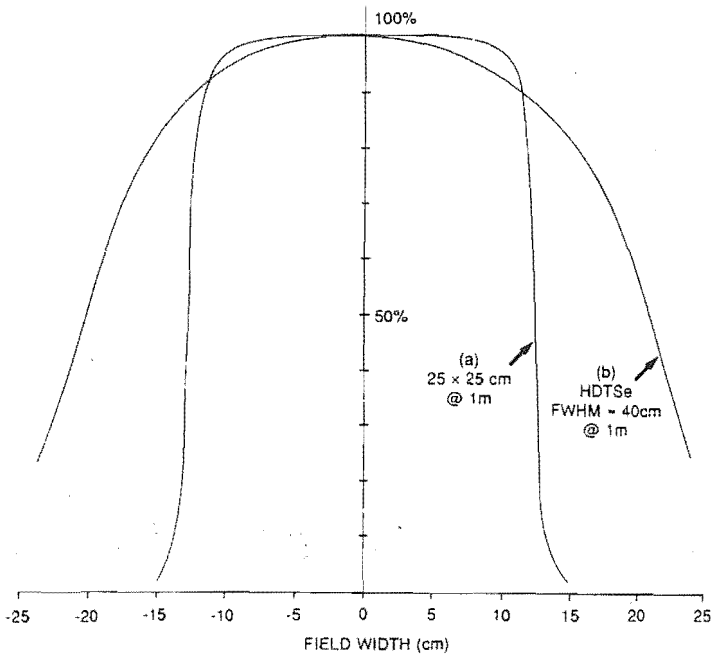

Figure 2.3: Comparison of 6 MeV electron beam profiles as Varian 2100c at 1 cm depth in water at 1 metre SSD. The high dose rate TSET mode (HDTSe) on the Varian 2100c accelerator has no applicator. (a) Standard 25 × 25 cm applicator (b) HDTS electron mode with no applicator.

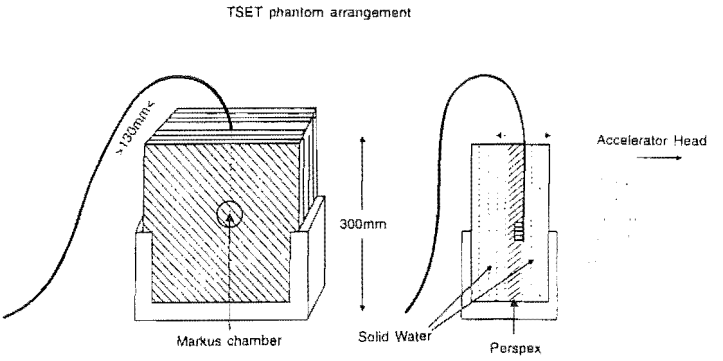

Figure 2.4: Placement of the Markus chamber in perspex and Solid Water. The Solid Water slab thicknesses vary from 2 mm to 5 mm.

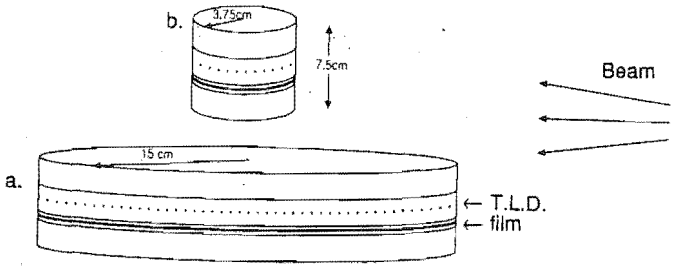

Figure 2.5: Cylindrical phantoms were used to access both the dose variations between the angled beams and the "overlap factor". Various diameters were employed to investigate the variation in this factor. (a) 30 cm (b) 7.5 cm. A 15 cm diameter cylinder was also employed.

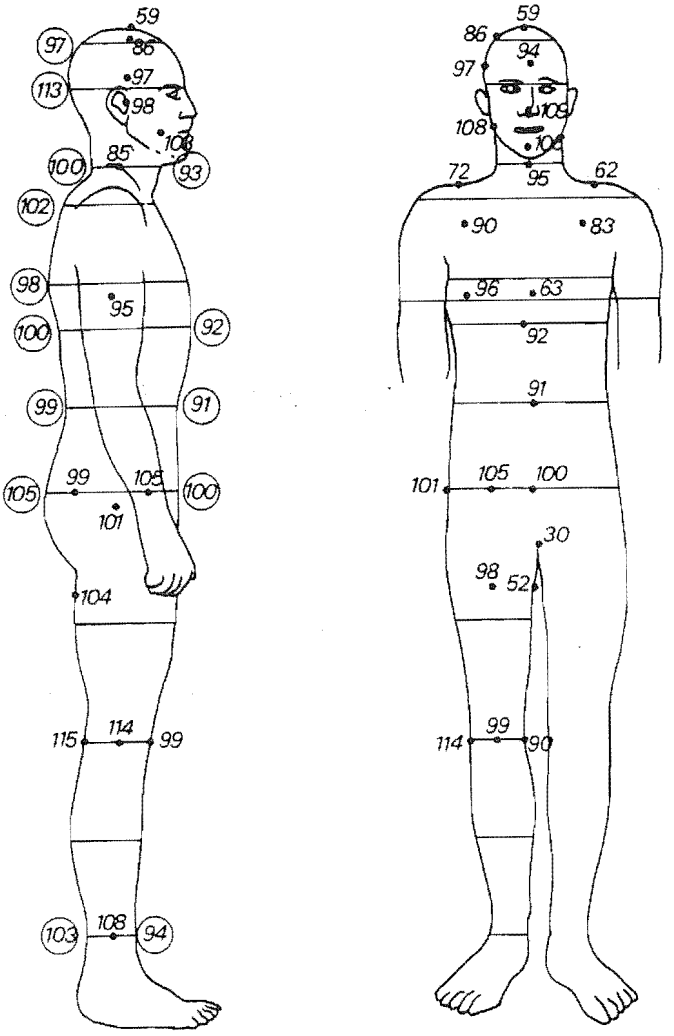

Figure 2.6: Distribution of dose measured with TLD on an anthropomorphic phantom.

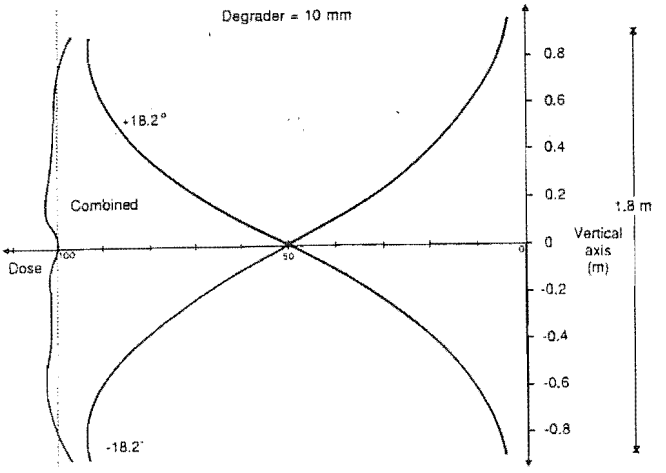

Figure 2.7: Vertical profile from a combined pair at $\pm 18.2°$. When the beam angles are optimised a very flat combined profile is achieved.

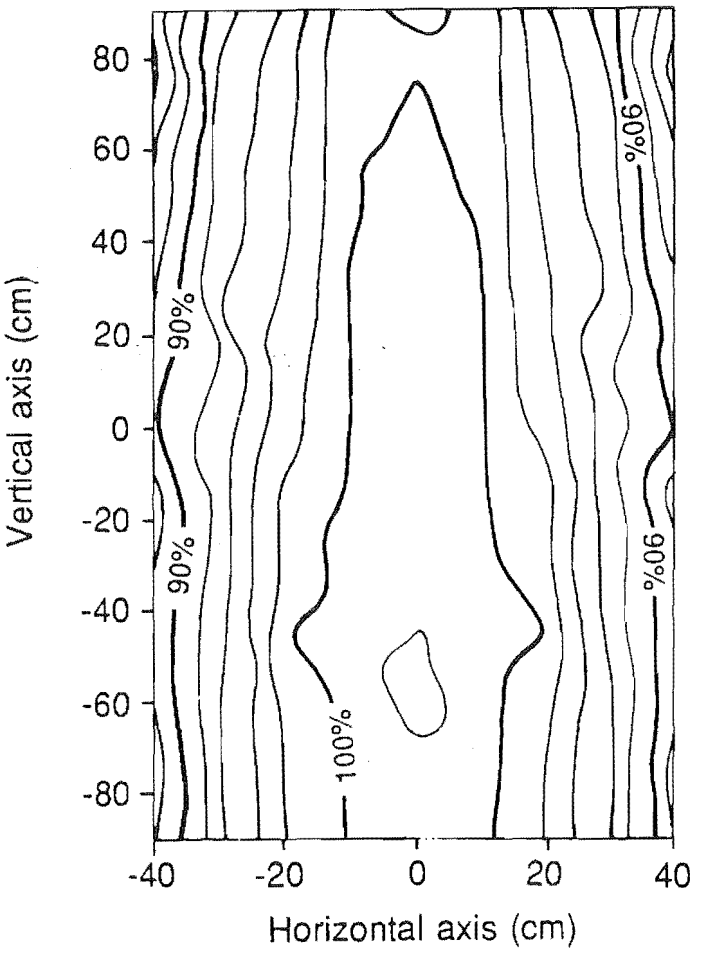

Figure 2.8: Regional dose distribution for a dual beam through the 10 cm degrader.

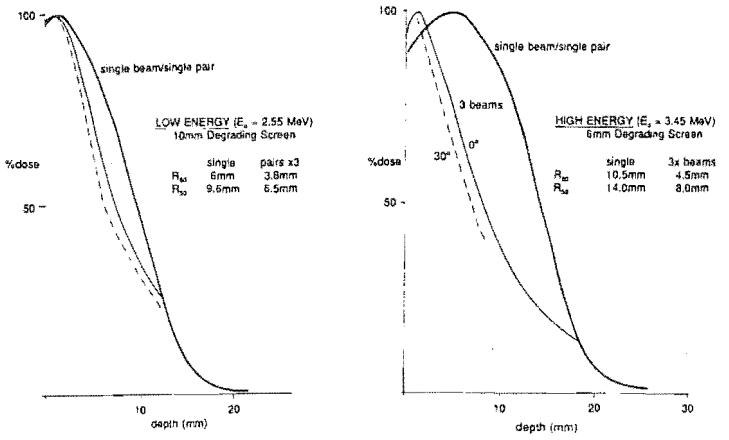

Figure 2.9: Initial % depth dose results. There is little difference between curves in Solid Water for a single horizontal beam and a single pair (<0.25 mm). Here a single pair/single beam is compared to three beams at 60° increments. Measurements were made at 0° and 30° in a perspex phantom with film.

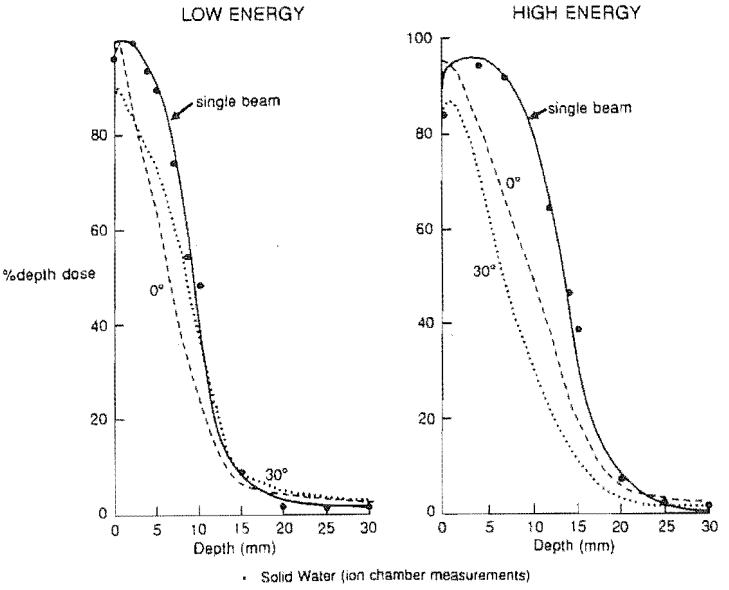

Figure 2.10: % depth dose for a single beam in Solid Water (•) and perspex cylindrical phantom compared with 6 beams of 60° separation with measurements made at 0° and 30° with film.

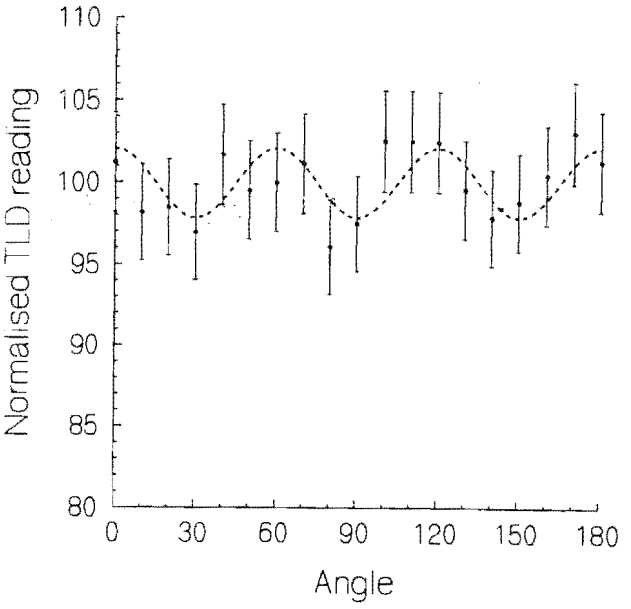

Figure 2.11: Cyclical variation about a cylindrical phantom for 2.55 MeV electrons, employing six beam pairs.

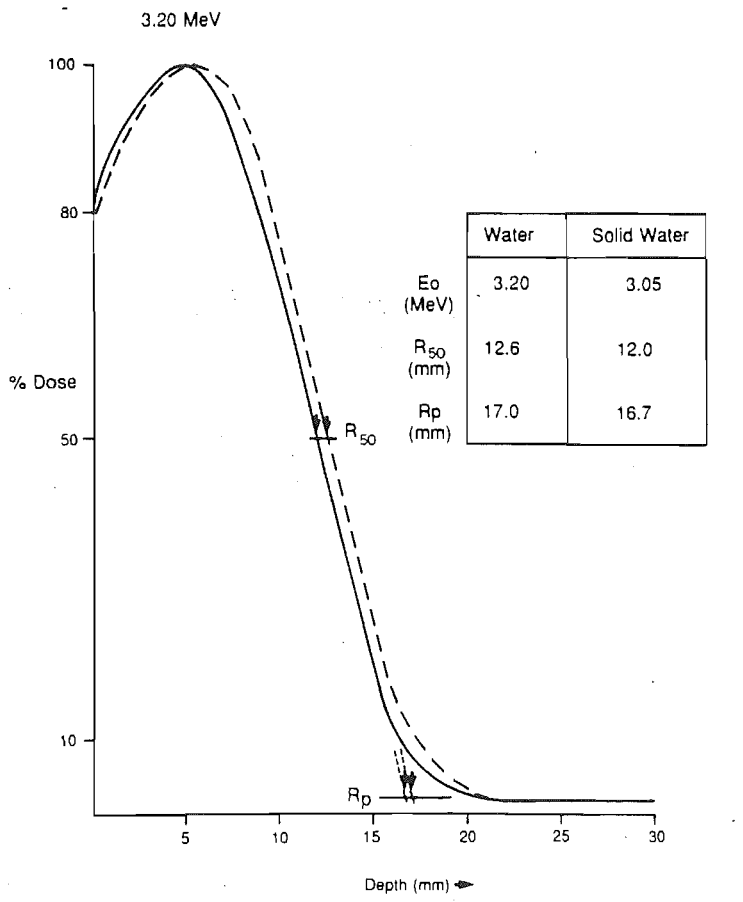

Figure 2.12: Depth Dose comparison between Solid Water and water at 3.20 MeV.

Chapter 3

Total-body irradiation on an isocentric linear accelerator: A radiation output compensation technique

3.1 Introduction

Bone marrow transplantation(BMT)[68] is a proven therapy for the treatment of many different malignancies, predominantly of haemopoietic origin. High dose radiation therapy is an important part of the conditioning treatment prior to the BMT. It functions to both destroy any remaining malignant cells and to ablate the patient's immunologic capability so that the transplanted marrow is not rejected.

Total Body Irradiation (TBI) has been used for the conditioning of a selected group of bone marrow transplant patients at Christchurch Hospital since 1978. The total dose administered must be carefully calculated prior to treatment, monitored closely during delivery and must be given according to extremely tight technical specifications to achieve the desired clinical outcome and avoid severe side effects.

TBI is now performed extensively and a number of different treatments are currently in use[222]. A prone/supine method of exposures is favoured over lateral fields by many institutions. This set-up tends to produce a more uniform dose distribution, particularly at the skin, and is comfortable for the patient. Practically, prone/supine treatments are difficult to implement because standard treatment fields are often not large enough. A number of methods have been devised to dynamically move either the patient or beam. Quast[70] describes a method where a specially designed couch is driven beneath a large field. Cunningham *et al*[223] have designed a movable Cobalt head that is mounted on a linear ceiling track. Such dedicated facilities are appropriate for centres with large numbers of TBI treatments. Smaller departments generally require their facilities for more routine treatments meaning that modifications can only ever be temporary. This introduces wear and tear and the possibility of component failure.

Our institution currently treats patients with the radiation beam from a modified Theratronics 780 Co-60 unit[224]. The patient is treated in the prone/supine position below the source as close to the floor as is practical and comfortable. Despite the temporary removal of the collimators and the use of a special beam-flattening filter, patients often require additional exposure to head and feet to bring the overall dose to within tolerance of the reference dose.

This chapter discusses the examination of an arcing TBI technique for the Varian 2100C linear accelerator. The technique employs gantry rotation in an arc therapy mode to produce a sweeping beam (figure 3.1). The dose reference point which lies on the mid-plane at the level of the patient umbilicus is one metre below the isocentre and two metres from the source. The lungs are relatively close to the central axis so that lead shielding in this area would be irradiated at close to normal incidence.

The method is similar to a sweeping beam technique previously applied by Pla *et al*[3] on a Therapi-4, 6MV linear accelerator with a swivel mounting. The swivel mounted unit has a longer distance between axis of rotation and the floor and therefore a larger area of acceptable flatness. With a centrally mounted gantry as is found on the Varian 2100C the dose at the patient plane suffers greater variation with gantry angle. We have compensated for this effect by altering the output. This method has not, to our knowledge, been previously performed on a modern gantry mounted accelerator.

Output control of this type enables the structure of patients to be used to obtained improved dose uniformity along the patient midline. This generalised technique is known as conformal therapy. Conformal TBI treatments have been performed using low melting-point cutouts. Jensen *et al*[225] describe the method and much of the central philosophy associated with this technique.

The chapter is divided into five main sections. The first is an experimental feasibility study in which profile measurements have been made and a PC based dose modulation system is used to assess the viability of this technique as a conventional accelerator modality. The next two section discuss the intricacies of calculating output tables, first for the uniform phantom then for non-uniform conformal patient treatments. A discussion is presented describing the manner in which conformal therapy is incorporated into this technique. The final two sections discuss patient dosimetry beginning with the calculation of tissue-maximum-ratio tables and concluding with a theoretical analysis of optimisation within the technique. This last section incorporates the measured data from the previous section combined with theoretical dose convolution to simulate the effects of the sweeping beam. The variation in dose is carefully

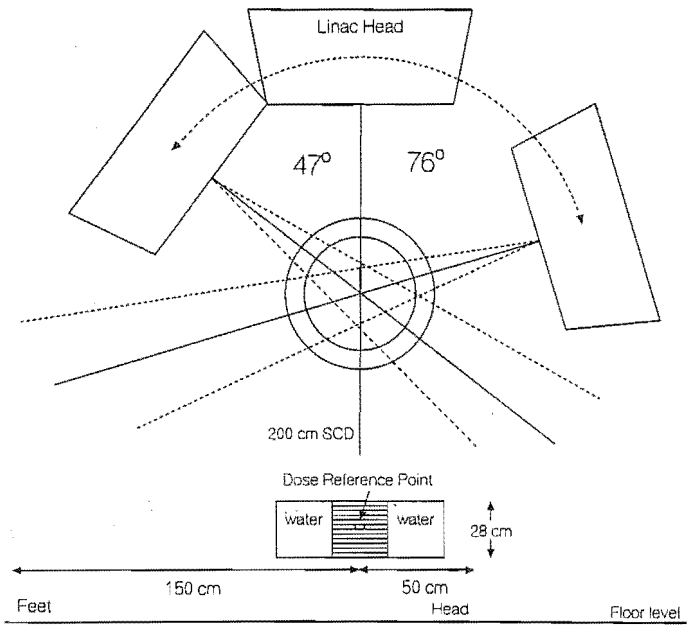

Figure 3.1: Schematic of the arc TBI treatment. The dose reference point (DRP) is a point 100 cm below the physical and dosimetric isocentre. The dose at the DRP is determined by the dose/deg setting in arc-mode and the width of the beam in the direction of travel. The phantom consists of a central stack of Solid Water between two tanks of liquid water and flanked by hard wood. The arrangement has a total width of 50 cm and total length of 90 cm.

considered under a range of patient and treatment conditions.

3.2 Feasibility study

Measurements of the spatial profile were taken for an arcing beam of 6 MV photons. A 0.1 cc cylindrical ionisation chamber was positioned at 1.5 cm depth in a 30cm × 30cm × 28cm stack of Solid Water (Radiation Measurement Inc, model 457). The Solid Water is flanked by containers of the equivalent size and shape filled with liquid water. The arrangement was placed at varying positions along the patient plane (figure 3.1). Figure 3.2 illustrates the results. The dashed line is the dose profile, $S(l)$, predicted from inverse square law

assumptions of the form,

$$S(l) = \frac{f^2}{[f_0 + \sqrt{(f - f_0)^2 + l^2}]^2}. \tag{3.1}$$

f_0 is the distance from the target to the physical and dosimetric isocentre, f is the distance from the target to the calibration point at the midline and l is the lateral position along the midline.

A difference is calculated between the two curves and a linear fit is made to these residual values. The curve of best fit is an inverse square function, as above, with an extra linear term that absorbs the effects of the changing oblique incidence. A look-up table is generated from the physical profile. The process by which this is generated will be described in the following section. In our feasibility study an IBM compatible personal computer was used to monitor gantry angle and control dose per degree. The PC used the look-up table to adjust the output such that a uniform dose profile would be produced in the regular phantom.

The present system on the 2100C deposits and records dose in half degree sections. The look-up table is configured in terms of a dose monitor unit (MU) per half degree where 1 MU roughly corresponds to 1 cGy at the isocentre. The control system reads the gantry angle and the number of monitor units already delivered then produces an output that is determined from the look up table.

The accelerator with PC controlled output adjustment, is driven manually through a complete arc ($-47^{\circ} \rightarrow 76^{\circ}$). These angles correspond to gantry positions that set the inside field edge of the beam, at the beginning and end of exposure, off the edge of the phantom. A dose distribution has been obtained in the same manner as the profile. The results are displayed in figure 3.2 where each point represents a separate arc. The variation is associated largely with uncertainty in the gantry angle determined by the PC control system and with mechanisms that will be discussed in the following section.

While the range of variation is unacceptable for patient treatment with better determination of the accelerator output and gantry angle this would be significantly improved. We do not, however, recommend the use of such exterior PC control for actual patient treatments. The modifications should ultimately be made to the accelerator's internal control software and this development will need to be carried out by the manufacturers.

The responsibility for the correct dosimetry for this technique lies with the institution as does the quality assurance of the software driving system whether it be PC controlled or internal to the accelerator. Quality assurance

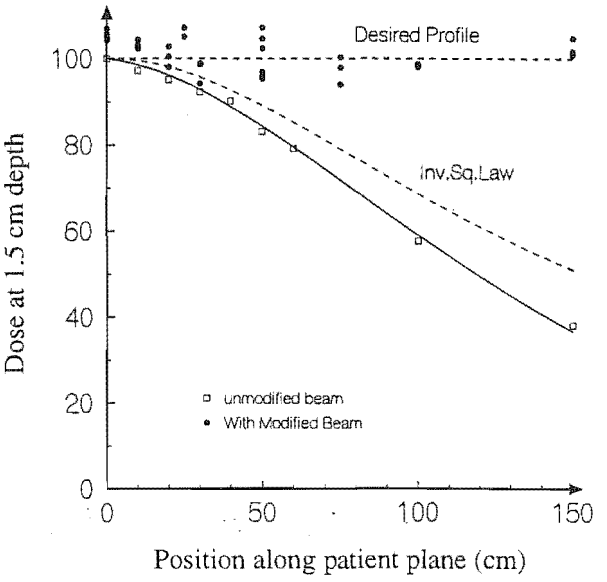

Figure 3.2: The dose profiles for unmodified and modified beams along the length of the patient plane. Measurements were made with a 0.1 cc cylindrical ionisation chamber. The inverse square law (dashed line) is determined from geometrical constraints and the best-fit is this expression coupled with a simple linear relationship.

of this technique can be maintained by in-phantom measurements of the dose-uniformity along the patient plane.

Finally, great care must be exercised whenever modifications of this sort are made to a linear accelerator control system. We recommend the practice of standard quality assurance assessments such as output and energy checks after any such modification and before any patient treatments.

3.3 The output look-up table

In practice, the finite width of the arcing beam complicates the calculation of an output look up table. A large field width is desirable because the dose delivered is directly proportional to the width along the patient axis. There is essentially a trade off between the spatial resolution of the field and the dose rates necessary for a practical treatment. Consider that at the maximum dose

rate (10 MU/deg), a field 10 cm wide at the dose reference point will require at least 18 arcs for one half of the 1.33 Gy treatment fraction we use at our institution (12 Gy in 9 fractions). Dose compensation will further increase the number of arcs as the maximum dose rate is required at the extremities where the beam suffers the greatest divergence. On the other hand, a field 80 cm wide at the dose reference point would require only 2 passes per patient orientation. However, in this case we are less able to control the deposition of dose and serious non-uniformity within the treatment volume may arise.

The controlled variation in the output with gantry angle, $O(\theta)$, can be calculated by forming a convolution of $O(\theta)$ with the field and and dose profiles, $F(\theta - \phi)$ and $S(\phi)$, to produce a uniform distribution.

$$\int_{-\frac{\pi}{2}}^{+\frac{\pi}{2}} O(\theta)F(\theta - \phi)S(\phi)d\theta = 1 \tag{3.2}$$

In Fourier space,

$$\overline{O(\phi)} = \frac{\overline{1/S(\phi)}}{\overline{F(\phi)}} \tag{3.3}$$

The transforms can be performed and a deconvolution of the output function can be extracted by pointwise division of the results.

If we assume that the beam is effectively zero width (a delta function) then the control function, $O(\theta)$, is just the reciprocal of the profile.

$$\begin{aligned} 1/S(\phi) &= \int_{-\frac{\pi}{2}}^{+\frac{\pi}{2}} O(\theta)\delta(\theta - \phi)d\theta \\ 1/S(\phi) &= O(\phi) \end{aligned} \tag{3.4}$$

The approximation is satisfactory when the variation in dose profile is small, ie close to the central axis. As the beam tends towards 90^0 proper compensation becomes impracticable if a sensible range of outputs is to be used. Consequently, it makes little difference whether a full Fourier inversion or reciprocal are taken. With the latter method we can choose an analytic extension to the profile that sets the resultant dose at the two extreme points to a predetermined value. The width of the field along the patient plane is then limited by what we determine to be an acceptable level of variation between the desired and actual output.

Discrepancy resulting from the finite width of the beam is related to several treatment dependent parameters, the length of the patient and the variation in depth to midplane along the length of the patient. The human body tapers in thickness towards the head and feet so in many cases we would want to reduce

the incident dose at the extremities. The result is that less adjustment needs to be made to the to the standard profile to achieve a uniformly distributed dose. In fact, Pla *et al*[3] found that the swivel mounted Therapi-4 Linear Accelerator produced a fall off in profile at the head and feet that was not only within an acceptable range of uniformity but also appropriate for the average patient dimension.

3.4 Conformal TBI

Dynamic control of the output can be used to introduce dose modifying data, pertinent to individual patients. The data is obtained by simple caliper measurements from reference points along the patient's length. Best-fit curves are calculated for each patient using tissue-maximum ratios (derived from thickness measurements) varying over the three parameters depth-to-midplane, field-width and distance from the central axis. The range of best-fit curves can be specified by only one parameter for the typical range of treatments. This parameter is the 2nd order coefficient, a. for a quadratic that is symmetric about the central axis.

$$D(l) = (1 - a(l/f_0)^2)D(0) \tag{3.5}$$

The coefficient a is therefore a dimensionless representation of the amount of fall-off required at the extremes. $D(l)$ is then coupled with the output function calculated from either equation 3.3 or 3.4 and an output look up-table can be constructed.

3.5 Tissue-maximum ratio measurements

Conformal treatments require the optimisation of beam parameters from patient details such as depth-to-midline. Tissue-maximum ratios (TMR) are used to convert these readings into the dose at midline. The TMR presented here (table 3.5) have been calculated from sets of percentage depth dose (%DD). The arc modality produces a field that is effectively infinite along the length of the patient. The effective field at each point along a patient midline is calculated from an arcing beam of width determined from the patient width at that point. This will lead to a small degree of error in the calculation particularly in regions of non-uniformity such as the neck. However, the overall effect is small as the compensating curve is formed from a smooth fit through all the data points. $D_{\max}$ varies along the patient plane and tends towards the surface

as the beam reaches lower angles of incidence. We have chosen to normalise all the TMR to 1.5 cm depth which is close to $D_{\max}$ at the umbilicus. Normalisation to a reference depth is, in effect, the definition of the tissue-phantom ratio (TPR). However, clinically the TPR is often associated with dose prescription to a deeper calibration point. In an effort to distinguish between the two concepts we would prefer to continue referring to these measurements as TMR.

A 50cm × 90cm × 28cm phantom has been used for all the TMR calculations (figure 3.1). The arrangement consists of a central stack of Solid Water and a cubical tank of liquid water on either side. Hard-wood flanks the arrangement to make up the volume. We find that for the largest fields, phantom material beyond the Solid Water (30 cm by 30 cm sheets) contribute less than 1% to the overall dose at normal incidence. However, it is necessary to place a water filled phantom on either side of the central phantom to minimise the effect of the shorter passage of radiation through the sides of the Solid Water at low angles of incidence. The effect is responsible for a dose increase of around 5% for an ion-chamber at 150 cm from the dose-reference-point and 10 cm depth (corresponding to an angle of incidence of about 30^0) and increases with depth. The phantom arrangement is sizable and it is not practical to perform actual TMR measurements. Instead depth dose measurements were made and peak scatter factors were measured to convert to TMR's. The conversion[226] has been adapted to incorporate fields of infinite length and finite width that we are using.

$$\mathrm{TMR}[d, w] = \frac{\%\mathrm{DD}[d, f, wf/(f+d)]}{100} \frac{\mathrm{PSF}[wf/(f+d)]}{\mathrm{PSF}[wf/(f+d_m)]} \left(\frac{f+d}{f+d_m}\right)^2, \quad (3.6)$$

where w is the field width and d_m is the calibration depth (generally at $D_{\max}$).

TBI treatments generally involve field coverage beyond the patient profile so the application of TMR's to TBI dosimetry is not trivial [227, 228]. The dose at midline is calculated from TMRs that are normalised to $D_{\max}$ over the range of field size and so a peak-scatter factor is applied to account for both collimator and in-phantom scatter. In large field techniques the size of the patient defines the field and is therefore independent of collimator effects. For convenience we have chosen to incorporate the in-phantom scatter term and table 3.1 expresses this adjustment to the TMR readings.

Depth-to-midplane readings taken from a patient are then converted into TMR via linear interpolation of table 3.1. A quadratic is fitted to the data and an output look-up table created as described in the last section. In prac-

Position	Depth	T.M.R. (Field width)			
	(cm)	15 cm	20 cm	30 cm	50 cm
0cm	1.0	0.959	0.972	0.999	1.023
	1.5	0.969	1.000	1.025	1.034
	2.0	0.976	0.997	1.020	1.027
	6.0	0.873	0.888	0.917	0.929
	10.0	0.774	0.790	0.819	0.834
	15.0	0.628	0.644	0.677	0.694
50cm	0.6	0.968	0.980	1.003	1.054
	1.5	0.995	1.000	1.023	1.065
	2.0	0.984	0.995	1.016	1.058
	5.0	0.899	0.912	0.937	0.977
	10.0	0.744	0.760	0.791	0.823
	15.0	0.605	0.622	0.656	0.684
100cm	0.6	0.984	1.000	1.030	1.041
	1.5	0.980	1.000	1.022	1.038
	2.5	0.934	0.949	0.976	0.986
	5.0	0.777	0.807	0.865	0.882
	10.0	0.584	0.612	0.669	0.686
	15.0	0.543	0.557	0.588	0.595
150cm	0.6	1.010	1.030	1.073	1.132
	1.5	0.990	1.000	1.045	1.099
	2.5	0.940	0.960	0.997	1.046
	5.0	0.816	0.836	0.873	0.905
	10.0	0.621	0.638	0.674	0.689
	15.0	0.474	0.491	0.525	0.526

Table 3.1: Tissue maximum ratio measurements made over a range of positions along the patient plane. Field width, perpendicular to the motion of the beam, is determined at the dose reference point (200 cm SAD). The arcing beam is 80 cm long in the direction of motion, the full field effectively infinite in length. A field factor dependent only on in-phantom scatter has been included in the TMR values (see text). At large distances from the DRP the obliquity of the incident beam means that D_{max} approaches the surface. The TMR are normalised to a depth of 1.5 cm for all positions hence some values are greater than unity.

tice the TMR points will tend not to fall in a neat quadratic pattern and the spread about these points would suggest significant variation at the treatment stage as illustrated in figure 3.5 for both patients A and B. This is a limitation associated with many large scale treatments such as TBI and total skin therapies. This treatment method represents a significant improvement in that general trends in patient structure can be taken into account rather than assuming the patient is entirely uniform. There is nothing to prevent this system being adapted to highly conformal treatments where detailed dose reconstruction would be possible about inhomogeneities such as the lungs, neck and feet. This approach would require narrow fields and consequently long treatment times.

3.6 Theoretical study

It is now useful to demonstrate how the recorded TMR data would be used to construct a conformal treatment. Theoretical dose deposition has been calculated for a range of former TBI candidates using a discrete convolution of the beam output to simulate the effect that varying dose has on a finite beam. The maximum discrepancy between the desired dose profile and the theoretically determined profile has been examined under a range of conditions. The optimisation of treatment is achieved by finding the balance between field width (which effects the treatment time) and the overall level of variation in dose. It is therefore useful to establish a maximum level of acceptable non-uniformity and base treatment optimisation upon this. For example, tall patients represent the worst-case situation and in this circumstance the best mid plane distribution is obtained by maintaining a uniform field along the length of the patient plane. For the average patient, the best distribution is obtained by allowing the field to fall off at the extremities in a similar manner to the field produced by the swivel mounted system. We have examined the role of two treatment parameters in this optimisation process, patient length and the extent of fall-off as discussed earlier. The patient length is reflected in terms of an umbilicus to toe measurement, $l_{\max}$, which represents the maximum distance from the central axis where dose is required. The results of this investigation are illustrated in figures 3.3 and 3.4.

Figure 3.3 examines the dose variation over changing field width and $l_{\max}$ necessary to produce a uniform ($a = 0$) field. Note that recommended variation in dose in the treatment volume places an upper limit on the field width used for treatment. Note also that treatments extending to 150 cm would represent the worst case and we see that a 40 cm field width is a safe lower bound to any

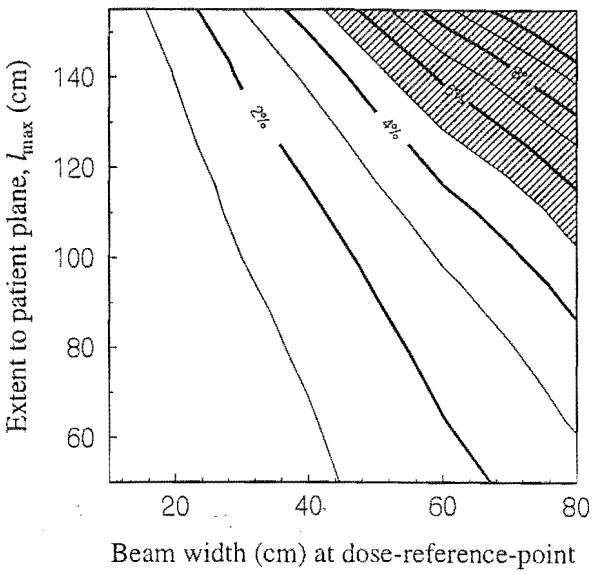

Figure 3.3: The effect of a finite beam width on the degree of dose uniformity over a range of maximum beam extent. Variation in patient length leads to some degree of control over the width of field in the direction of motion. l_{max} is defined as the distance from umbilicus to toe. The shaded area represents a level of non-uniformity within the treatment volume that lies outside the $\pm 5\%$ limit recommended by the National Radiation Laboratory of New Zealand.

treatment. However we note that for such a case an 80 cm field width would result in more than $\pm 10\%$ variation in dose. Figure 3.4 is a combination of the two treatment dependent parameters a and l_{max}. ICRU (1976) findings adopted by the National Radiation Laboratory in New Zealand suggest that variation of dose within the treatment volume be kept within $\pm 5\%$. The recommendation represents an upper limit to the field width used during a treatment.

Finally let us consider a treatment plan. Figure 3.5 shows the calculated TMR's for patients A and B with a best fit polynomial taken through each set of data. Note the difference in fall-off for the two cases. We will examine a treatment plan for patient A. If we refer back to figure 3.4 we see that this treatment would allow a field width of more than 70 cm and still remain within

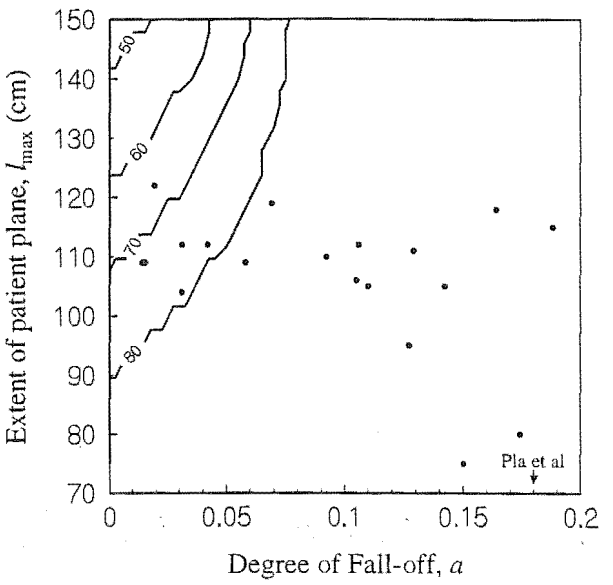

Figure 3.4: The limiting field-width imposed by a ±5% recommendation for variation within the treatment volume. Marked points on the graph represent a number of recent TBI candidates at this institution. Patient records have been used to compile sets of TMR values for a number of points along the body. Lines of best fit are used to determine values of a. The arrow marks an effective a value for treatments with the swivel mounted system described by Pla *et al*[3]the. l_{max} is defined as the distance from umbilicus to toe. Note that of 19 previous patients, 13 patients could be treated with the maximum 80 cm long arcing field.

the ±5% recommendation level. The patient is positioned with umbilicus at the dose reference point requiring the gantry to go beyond 115 cm (l_{max}) in the patient plane.

For the purpose of these calculations we estimate the size of the reference dose (D_{ref}) by multiplying the dose per degree output of the machine by the angular width of the beam. D_{ref} is defined as the dose at D_{max} at the dose-reference-point for an 20 cm wide arcing beam (the TMR at this position is 1.00 by definition). The maximum dose rate for the arc modality on a 2100C is of the order 0.1 Gy/deg at the isocentre and the 70 cm wide beam has an angular spread of 19.8^{o}. This leads to a maximum dose of around 0.5 Gy being deposited at the treatment plane per treatment arc. Finally to deliver the range

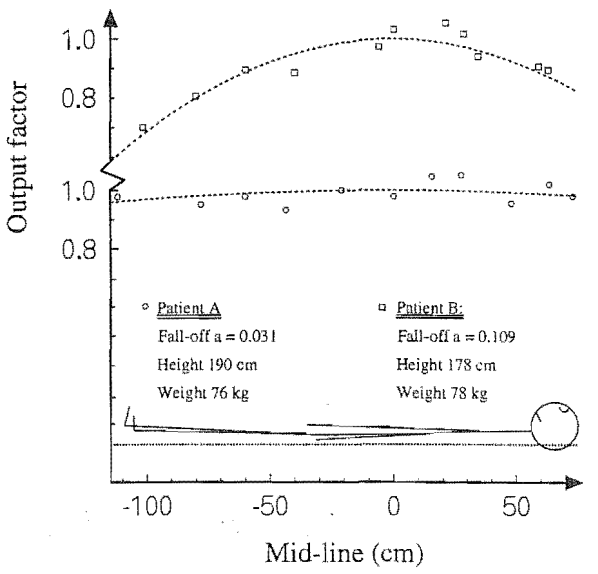

Figure 3.5: Comparison of conformal treatments for two patients. Patient A and B are former TBI candidates at this institution. Output factors are determined from TMR measurements as described in the text.

of dose required for compensation the maximum dose-rate is required at the extremities. The reference dose is reduced by a factor $D(l_{\max})$, in this case 1.95. $D(l_{\max})$ is determined from the profile (figure 3.2) at $l_{\max}$ as discussed earlier in the chapter.

$$\begin{aligned} D_{\text{ref}} &= \left(\frac{100\text{cm}}{200\text{cm}}\right)^2 \frac{0.1\text{Gy/deg} \times 19.8^{\text{O}}}{1.95} \\ &= 0.25 \text{ Gy} \end{aligned} \tag{3.7}$$

The value of the midline TMR at the umbilicus completes the calculation, in this case 0.76. A prone/supine treatment delivers twice the dose.

$$\begin{aligned} D_{\text{arc}} &= 2 \times 0.76 \times D_{\text{ref}} \\ &= 0.40 \text{ Gy per dual treatment arc} \end{aligned} \tag{3.8}$$

A 1.33 Gy fractional treatment would be achieved by arcing the beam over the patient four times per patient orientation. Dose delivery of less than 0.4 Gy is

controlled by changing the dose per degree or some other associated parameter. The calculation demonstrates the benefits of large field treatments. While the approach has shortcomings, particularly in the area of dose homogeneity, the problem is controllable and with good dosimetry can be minimised for accurate and efficient treatment.

3.7 The Dynamic Beam Delivery toolbox

This section describes an examination of the Varian dynamic beam delivery control software. The evaluation took place at Varian Inc., Palo Alto, California. This system has been recently installed on the Varian 600C accelerator at the Christchurch Oncology Service.

3.7.1 Operation

Segmented treatment (ST) tables are calculated and loaded into the accelerator PC. The Dynamic Beam Delivery (DBD) toolbox operates as an extension to service mode. The user indicates this option under the setup menu and is required to enter a file name of the type *.stt . The STT can be constructed off-line and is built in the manner described in the following section.

The segmented treatment is coded in terms of the accelerator coordinate versus a normalised cumulative dose. The ST table is independent of the total dose which is dialed up in the usual manor. A dose segment (as opposed to the cumulative dose) gets scaled appropriately.

The cumulative dose can be regarded in terms of a time coordinate and indeed indicates the forward progress of the treatment. The position coordinates of the accelerator for each axis in motion (be it gantry angle, collimator angle/positiou. couch position, etc) during the course of a treatment therefore need to be worked into a set of discrete positional elements. It is not neccesary to tabulate coordinates which will not change. The orientation of the accelerator must correspond with the starting coordinates set or else an interlock will occur.

The cumulative dose and the accelerator orientation at any point in the treatment constitute a target for the accelerator mechanism. If for any reason these parameters lie outside of the the Varian specification for tolerance the accelerator will correct appropriately. The controller can optionally reduce the dose rate (for over-dosing at the target position) or slow the progress of the accelerator mechanism (for under-dosing). If either of these conditions are critical the accelerator can stop motion, stop the beam and even back up as

necessary. In general the manner in which a particular segmented treatment is performed in such a way as to minimise the treatment time. Motional and dose production constraints lead to two different limiting behaviours, dose-rate limited or motion limited.

The dose-rate dialled up in service mode is regarded as a maximum dose-rate by the DBD toolbox. Consequently if the positional coordinates are easily attained in the time required to deliver the dose fraction (this is simply a mechanical constraint) then the treatment segment is described as dose-rate limited. In other words it is the constraint of generating the actual dose that limits the time required to complete the treatment and hence the rate of motion must be reduced to compensate.

Conversely if the dose is easily generated in the time required to mechanically reposition the accelerator for each position in the segmented table then the treatment segment is described as motion limited and the dose-rate must fall to compensate. Examples of both types of behaviour will be discussed shortly in the context of the arc-TBI technique.

3.7.2 Arc mode TBI tests

Dynamic TBI therapy can be facilitated in a number of ways given the full dynamical freedom of the accelerator. We shall analyse two methods. The first method uses the dose modulation technique described in previous sections. A second variation on this technique controls dose at the patient midline by varying beam width in the direction of motion.

The dose at the midline for a uniform beam output can be determined to a first approximation using simple geometrical arguments including the inverse square law. The SSD varies with angle according to the following formula

$$\mathrm{SSD}(\theta) = f_0 + \frac{f - f_0}{cos\theta} \tag{3.9}$$

where f_0 is the source to the axis of rotation (1 m) and f is the distance from the target to the dose reference point as defined for equation 3.1. If we assume the inverse square law applies then the dose-rate $D(\theta)$ at θ must be proportional to

$$D(\theta) = (f_0 + \frac{f - f_0}{cos\theta})^2 \tag{3.10}$$

The representation of dose in the segmented treatment table is a normalised cumulative dose (NCD) and hence it is necessary to integrate the above formula from the starting angle to the angle θ' and to divide the resulting expression

by the full integral between the start and the final angle θ_f ie

$$\mathrm{NCD}(\theta') = \frac{\int_{\theta_i}^{\theta'} D(\theta)d\theta}{\int_{\theta_i}^{\theta_f} D(\theta)d\theta} \tag{3.11}$$

which increases monotonically from 0 through to 1. The simplest way to carry out this calculation is to generate a table of $D(\theta)$ of adequate grid size and use a numerical procedure to generate the NCD function. The number of entries in the segmented treatment is dictated by the grid size determined at this point.

The rotation of the gantry requires special consideration owing to the highly inertial nature of the motion. While it is possible to request large variations in the rate of rotation of the gantry in the segmented table the actual implementation may require complicated combinations of dose-rate and gantry rotation-rate. This is easily illustrated if we consider a treatment where an already dose-limited situation is compounded by a rapid increase in the segmented dose requiring the accelerator to slow the gantry abruptly. In this case the controller would stop the dose and gantry motion and back up before continuing with the treatment. As this process is fully automated the only consideration is that dose is being placed accurately throughout the procedure.

Two types of checks are necessary. Firstly the machine must behave according to well defined specifications of output as determined in the treatment head. However, it essential to see these tolerances transferred to in-phantom measurements. With stationary therapies these two measures will correspond but in the case of a dynamic therapy the output at the head is spread over a range and does not necessarily correspond to the dose at the patient. Fortunately, with an arc mode method, using a fixed field and output compensation, the dose at any particular point is porportional to the total cumulative dose and to the field size in the direction of the gantry motion. On the other hand when the field size varies during the course of the treatment there is no direct relationship between the output determined at the head and the dose in the treatment plane.

A series of tests were performed with the DBD toolbox using sets of .stt tables derived in the manner described above. Some variations on the basic compensated arc (RTBI1) were also examined including multiple arcs (RTBI2), a single arc with a discontinuity (RTBI3) such as might be used for automatic lung compensation and a multiple treatment using a combination of variation in field width and dose-rate (RTBI4).

Two methods of dosimetry were used in addition to the accelerators inbuilt ion chambers. A 0.6 cc chamber and Farmer type electrometer were used

Total dose	Dose rate	IonCh reading
50MU	600 MU/min	46 R
	100 MU/min	46 R
200MU	600 MU/min	183 R
	300 MU/min	184 R
	100 MU/min	182 R
800MU	600 MU/min	730 R
	100 MU/min	717 R

Table 3.2: Dose consistency from an arc therapy with variations in the total dose and dose-rate.

to examine in-air exposures. Standard XOmat film was used to examine the dose distributions generated by the arcs with a discontinuity.

The first set of measurements examined the dose-rate effects described above. A segmented treatment for a single compensated arc was examined with the ionisation chamber at the intersection of the central axis and the patient plane. The patient plane was defined to be 56.8cm below the isocenter.

The results in table 3.2 illustrate the stability of the accelerator dosimetry system for a range of gantry motion limited (for example 50 MU delivered at 600 MU/min) and dose-rate limited (for example 800 MU at 100 MU/min) circumstances. The measurements for the 800 MU treatments were somewhat different but the discrepancy was found to be due to ion chamber drift particularly as the latter of these two treatments requires 8 minutes to be performed.

Table 3.3 is a summary of ion-chamber readings for the four segmented treatments examined. All the arcs were performed at a 600 MU/min dose-rate and a total dose of 200 MU. Under these circumstances, the treatments progress at the maximum and constant gantry rate of 5^0/sec. Dose compensation, therefore, is entirely due to variation in the output and/or field size. The initial and final angles are 110^0 and 250^0 in the Varian coordinates system. The chamber is placed at the dose reference point, defined above.

A second set of measurements were performed with the chamber at a position, 50 cm from the dose reference point in the direction of gantry motion (table 3.4).

Comparison of the measured exposures at the two positions indicates that the dose is only 90% of the reference dose at 50 cm despite compensation in the output. A comparison to the theoretical prediction of the uncompensated dose, using equation 3.1, gives some encouragement, in that the uncompensated dose at this point would be 80% of the reference dose. A measurement was made

.stt file	Description	field size	IonCh reading
RTBI1	single arc	10×20	564 ± 2 R
RTBI2	triple arc	10×20	573 ± 3 R
RTBI3	single arc	2×20	26 R
	with 5cm gap	10×20	383 R
RTBI4	single arc	10×20	400 ± 2 R
	dose+field size compensation		

Table 3.3: Dose measurements at the dose reference point for four TBI dynamic delivery routines.

.stt file	Description	field size	IonCh reading
RTBI1	single arc	10×20	503 ± 7 R
RTBI2	triple arc	10×20	510 ± 2 R

Table 3.4: Dose at the pateint plane, 50 cm from the central axis.

of the exposure for a standard fixed field of size 10 cm×20 cm at 180^0. 50 MU produced a reading of 1700 R. The same fixed field was directed at the 50 cm position (a gantry angle of 139^0) giving an exposure of 1400 R. The ratio of these values (0.82) suggests the model we have used is accurate in predicting the dose fall off.

As we have used a much closer dose reference point in this exercise, 160 cm SSD as opposed to 200 cm SSD in the feasibility study, we would expect some of the effects discussed in previous sections, such as rapidly changing dose rates, to have an even more profound influence.

3.8 Conclusion

Radiotherapy treatment machines can be involved in a wide variety of routine treatment methods but present methods of TBI treatment will often encroach upon regular treatment schedules. A technique has been proposed that does not compromise routine treatments through machine modifications and is easy to set up. The patient is treated in the prone/supine position offering maximum comfort while avoiding problems with lateral exposure.

The present generation of computer controlled linear accelerators readily lend themselves to this application of "conformal therapy"[69]. Individual patient compensation can be achieved by measuring an array of TMR values for the three parameters depth, field width and position then calculating best-fit

output tables. Theoretical treatment plans have been investigated for a range of previous patients. These calculations suggest that practical and efficient TBI treatment using a variable output mode of arc therapy will be of significant benefit to our own institution and many others.

Chapter 4

A Monte Carlo approach to linear accelerator bunker design.

4.1 Introduction

A central issue during the installation of a linear accelerator is the the degree of exposure generated by the linear accelerator in the area outside the accelerator maze structure. This is often an area with high occupancy owing to radiation technologist traffic in to the maze immediately after treatment. It is therefore in the interests of oncology institutions to have accurate estimates of exposures rates likely to be recorded in these areas.

With this general problem in mind and with the immediacy of installation of a Varian 600C, 6 MV, therapeutic linear accelerator at our own institution, this project was initiated. Several user-codes that operate with the EGS4 system have been written. These programs have been tailored for the job at hand but with emphasis on the portability of the coding to other maze designs. The original version of user-code, MAZE600C, is modified to a more generalised format that accepts an input file with tabular information about the maze design. This code is called MAZE2D. The user-code and some straightforward examples are available from the author.

4.2 Designs and alterations

Figure 4.1 shows the design of the third bunker built according to Varian specifications, recent alterations are indicated. Early investigations suggested the need for increased shielding. This was due in part to the advent of new radiation dose limits in 1990 as proposed by the ICRU but also to the somewhat costly assumption that leaded doors would be installed. Our investigations suggest that with the addition of a second wall between accelerator and entrance and lintel piece reducing the size of the portal at this position would bring the absorbed dose in high occupancy area outside the exit within specifications.

4.3 First order scatter calculations

A approximate technique is typically used during commissioning of therapeutic linear accelerators. The techinque is good for an order-of-magnitude estimate of maze leakage and has been used at Christchurch Hospital during the installation of the 2100C accelerator and as a calculational check during the design of the 600C bunker.

We are interested in computing the occupational exposure for a set of target points outside the beam enclosure. An integration of the product of factors (f1, f2, f3,...) associated with scatter off the maze walls and inverse-square law factors for the distances separating source, scatter and target points ($1/s1^2 \times 1/t1^2$) can be performed (see figure 4.2).

Scatter coefficients are often referred to as albedo and a number of recent papers have looked at the calculation of an albedo for materials such as the concrete in the wall[109, 110]. The calculation considers primary scatter in the patient or phantom and secondary scatter at the walls or roof and as such the calculation comprises of a product of two scatter terms and three inverse-square-law terms.

The calculation can be greatly simplified by dividing the inner surfacee of the maze into strips of wall that be regarded as equidistance from the source or from the target point. A summation of these elements can be performed using a spreadsheet program.

4.4 EGS4 User-codes

Several user-codes have been written for the purposes of these calculations. As well as code to simulate the scatter inside the maze a user-code TANK determines the interaction of the accelerator X-rays with a large cylindrical tank. The code generates spectra for each of the three surfaces and fractionates the energy deposition into forward- and back- and side-scatter components as a fraction of the total energy output of the accelerator (figure 4.3).

The spectrum so calculated using a 6 MV spectra and TANK is then used in conjunction with MAZE600C to simulate the passage of scattered photons through the maze. MAZE600C records the differential (spectra) and total fluence for radiation passing through the entrance. The code has a generalised layout so that changes to the maze structure can be easily introduced into the code. A 6 MV spectrum can be found amongst the EGS4 distribution. This spectrum was generated by Mohan et al[229] using Monte Carlo simulation.

The other piece of external information required for this simulation is the

atomic composition and density of concrete. The EGS4 system is both well documented and well supported. Amongst many handy routines and user-codes is a reasonable assortment of material inputs required for the preprocessing package, PEGS4. A garden-variety concrete has been provided as an example of a mixture. This is be quite suitable for the accuracy of calculations that were required. The material composition was also obtained using geological XRF, performed on a concrete core, drilled from the same concrete as in the bunker. This approach is recommended as there can be variations in the concrete mixture, especially purpose mixed concretes used in a radiation protection context.

The geometry encoding in MAZE600C consists of intersecting planes. The planes form the bounding regions of the maze structure (see figures 4.4 and 4.5) and are inputed in a table. Planes and the regions between them are labelled and used in the EGS4 HOWFAR and AUSGAB routines for boundary crossings and energy bookkeeping. The table has an entry for each plane that consists of one coordinate on the the plane and a normal vector to the plane. The planes divide the geometry up into a number of regions where neighbouring regions contain different materials. Other planes are simply convenient book-keeping divisions of the same material.

A table of regional transitions is created according to the geometric relationships of these regions in the maze. The walls can be reflecting surfaces or absorbing surfaces. A reflecting surface is essentially a plane that divides two regions, one air the other concrete. The second region must be thick enough to generate an accurate representation of the backscatter if it was infinitely thick. The surface on the far side of this region is usually completely absorbing. A completely absorbing surface is used in situations where it is determined that particles in this region are unlikely to leave via the open corridor. This includes the walls behind and to the right of the linear accelerator, the inside corridor wall and the bounding surface behind reflecting walls as mentioned.

The code is simplified by the nature of the problem as the roof and floor are sets of reflecting planes at right angles to the walls. While it is necessary to create regions above and below these planes for the purposes of back-scatter (which triples the number of regions required), the connectivity of regions is the same and this information can be evolved from data associated with the central volume.

The program runs large numbers of particles through this geometry and outputs energy fractionation for each of the regions including the maze exit. This fraction can be converted into a fluence by multiplying it by the total energy output of the accelerator and dividing by the surface area of the maze

exit. The program also generates a spectrum at the exit which is useful in determining the thicknesses of radiation protection materials such as a maze door.

4.5 Results for the Varian 600C enclosure

The spectrum generated from scatter at the patient is determined for a 50 cm diameter by 40 cm water phantom, irradiated from the top by a 40x40 cm^2 field generated with a 6 MV x-ray spectrum.

The contributions from back-, forward- and side-scatter components are summed and used as input for the maze simulation. The average energy of the scattered particles is 450 keV. The total proportion of energy re-emitted is 0.384.

Firstly, a calculation of the total weekly accelerator output is required and can be determined from a predicted weekly cumulative dose. The energy fluence rate is found by dividing the in-phantom measure of dose by the mass-absorption coefficient, (μ_{ab}/ρ), for water (i.e. equation 1.2). (μ_{ab}/ρ) equals 0.0026 m^2/kg at an average photon energy of 2 MeV. The largest field size (40x40 cm^2) is used to determine a maximal energy output from the fluence (energy per unit area).

For an 800 Gy/week programme, the nominal (maximal) accelerator output is rate produces a total energy of 4.9×10^4 J per week. This output is somewhat absorbed by the phantom or patient (leaving 38.4%) In the simulation we have considered only the hemisphere facing the corridor which reduces the energy admitted into the calculation by a further factor of two. This figure, 9.4×10^3 J/week is reduced by a factor relating to the fraction of energy exiting the maze, calculated by the Monte Carlo method.

The calculation of the energy fraction at the entrance of the unmodified maze(figure 4.4) procedes as follows. The fraction of energy at the maze entrance is calculated by summing the energy deposited in region 6, a totally absorbing region just outside the maze. A total of 10^6 particles with average energy 450 keV result in 732 particles at the corridor exit (±4% statistical uncertainty) depositing an average energy of 360 keV.

$$\begin{aligned} \text{fraction of energy at exit} &= \frac{.360 \text{ MeV} \times 732 \text{ exiting}}{0.450 \text{ MeV} \times 10^6 \text{ starting}} \\ &= 5.87 \times 10^{-4} \end{aligned} \tag{4.1}$$

The fluence at entrance is derived from the total energy leaving the maze divided by the area of the maze exit.

$$\begin{aligned} \frac{d\Psi}{dt} &= \frac{9.4 \times 10^3 \text{ J/week} \times 5.87 \times 10^{-4}}{9.75 \text{ m}^2} \\ &= 0.566 \text{ Jm}^{-2}\text{/week} \end{aligned} \tag{4.2}$$

The occupational exposure rate is given in units of equivalent dose (Sv) per unit time. The conversion between dose and dose equivalent is unity (photons). The dose is determined in the usual fashion but now the average particle energy is less and therefore more absorbing ((μ_{ab}/ρ) for water is 0.0032 m^2/kg).

$$\begin{aligned} \text{Dose equivalent rate} &= \left(\frac{\mu_{ab}}{\rho}\right)\frac{d\Psi}{dt} \\ &= 1.8 \times 10^{-3} \text{ Jkg}^{-1}\text{/week} \\ &= 1800\,\mu\text{Sv/week} \end{aligned} \tag{4.3}$$

The calculation is performed in the same manner as above for a lintel piece designed to reduce the size of the maze portal. A small adjustment to the coding has been made to eliminate all particles passing into region 4 above a certain height and the dividing wall was added.

The energy deposition at the entrance 1.39×10^{-4} MeV per history with all other considerations being equal the occupational exposure is reduced to 950 μSv/week.

To investigate the effect of the additional wall the calculation required substantial remodelling (see figure 4.5). An examination of the fluence at the elbow of the maze (Region 4 in the original layout - now region 6) was carried out and the calculation performed in two parts. Improvement of the simulation was required particularly the arrangement and reflectivity of the side wall and concrete partition.

The fluence obtained at this point in the arrangement with the lintel, 0.0126 MeV per history, is compared to the fluence obtained with the concrete divider, 0.00036 MeV per history. Therefore an effective dose reduction factor of 0.029 is derived giveing a comparable exposure of 27μSv/week. This arrangement was used in the final design of the accelerator enclosure.

4.6 A method for a general enclosure - MAZE2D

MAZE2D is specialised user-code written for the EGS4 Monte Carlo platform.

The code is portable to a range of computer systems and, here, has been tested on a Sparc-20 running Solaris and SGI/IRIX.

MAZE2D, as suggested by the name, is designed to provide information about radiation transport out and about a generalised enclosure, where the roof and floors can be considered to be a set of parallel planes. The walls are defined as a series of connected vertical planar surfaces. The code is precompiled and the user can specify the conditions of the problem at run-time or in the form of a prepared input file.

MAZE2D has been designed to provide a "front-end" to two-dimensional maze and bunker calculations. The emphasis is therefore on defining geometry and examples are provided. It is possible to employ output from a computer aided design package and indeed the user is encouraged to use such assistance.

EGS4 caters for both photon and electron transports in regions of homogeneous media. The nature of a bunker type geometry affords an interesting simplification to the transport. Because such a geometry is simply connected (i.e. you can walk into it), we need only define a small number of regions for which transport properties are defined. These regions are the interior of the bunker (our air volume), the wall (generally concrete), the roof and the floor. Exceptions to this basic geometry can be included and are prioritised by adding them to the beginning of HOWFAR.

The user is therefore required to enter a series of points that circumscribe the perimeter of the maze. Surfaces are divided into interior and exterior surfaces for the purposes of handling particles when they leave the maze volume. There are several criteria that must be observed when entering coordinates of the interior walls, with regard to the definition of the normal to these surfaces. A right-hand-rule is observed in that travelling from point n to point n+1 the normal points to the left. If this detail is not consistently observed then the code will not be able to determine the appropriateness of a boundary crossing.

Other details of the user inputs are more straight-forward. The format for entry and an example are given in figure 4.6.

A few details are worth mentioning. The graphical interface we have used, called EGS4Windows3.0, provides a convenient means to check that the geometry has been coded appropriately and, indeed, that the user-code itself is performing the appropriate transport. The interface uses two files generated by MAZE2D. One describes the progress of the particles, the other describes the geometry.

A small number of histories are generated (say 1000) and the passage of these particles through the media is outputed to a .gph file. The file is generated from AUSGAB (each time there is an interaction or a boundary crossing)

and contains the current particles charge and region number, its location in coordinates, (x,y,z), and its energy.

A .geom file is generated by MAZE2D on a basis of the user inputs. The points describing the locations of walls and the connectivity of the enclosure are translated into graphical objects such as plane walls.

Obviously greater numbers of histories (say 10^6) are required to get an accurate value for fluence at the exit. Indeed a large number of histories may be required to get even a single particle crossing the exit surface. The graphics output file is generally large, so it is advisable to switch this output off once the geometry and particle transport has been verified.

An interior surface is defined as a surface through which one is interested in continuing to transport the particle. An exterior surface implies that, upon passage through this surface, the particle is discarded.

The point description of the maze walls has number_of_walls + 1 entries, such that each (n+1)th entry describes the second (x,y) coordinate in the wall. As one wall connects to the next in sequence this is all the information required. The two-dimensional layout is simply connected.

The floor marks the $z = 0$ ordinate. but otherwise the placement of the source and the positioning of the maze walls is entirely arbitrary. The exit surface is defined by two points and must obey the same right-hand rule. It can perhaps be viewed as an extension to the wall geometry though it does not necessarily have to be simply connected. In fact the exit may be placed anywhere in the maze and provides a useful tool for exploring fluence levels at different points in the bunker structure. It is advisable, however, that the exit closes off the bunker as particles are not required to stay within the maze. The onus is on the user to ensure that the geometry is ultimately "closed".

The direction of the beam can be set. The vector need not be normalised. Finally the beam can be either mono-energetic or can use a predetermined spectrum[229], as has been discussed.

4.7 Relevance and conclusions

A general code for performing radiation calculations in an enclosure is a very useful tool to a radiation oncology clinic. New radiation devices are regularly commissioned and part of the commissioning process is assessing the radiation protection issues of running such a device in the work place. It may be necessary to plan in advance. A room or bunker may require substantial modifications before the device can be used safely.

A Monte Carlo method is an ideal way of performing these calculations. mathematically, no less cumbersome than a scatter integration method, particularly with public-domain Monte Carlo such as EGS4 readily available. Typically an institution would aim to undercut a radiation occupancy guideline by an order of magnitude. Consequently the calculation will not need to be extremely accurate and the calculation time can be short.

MAZE2D has been designed to read in a generalised enclosure as a series of points that may, for example, be generated by a computer aided design (CAD) package or a digitometer.

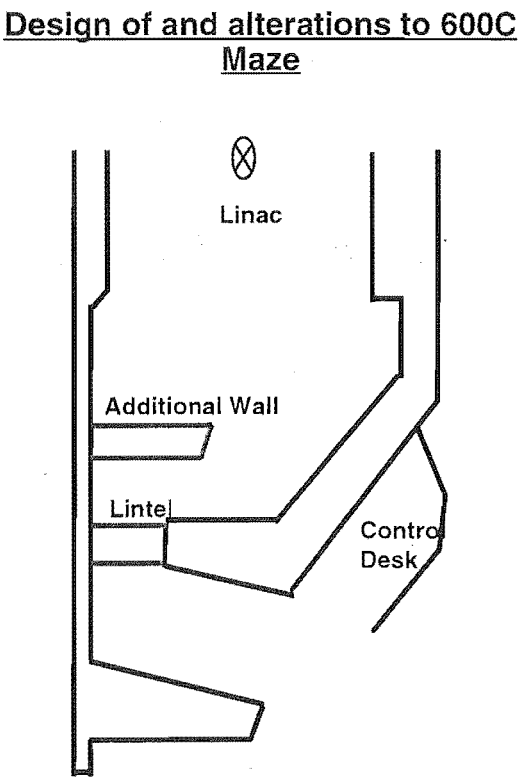

Figure 4.1: The third bunker at Christchurch Oncology service with additional shielding in the form of an extra wall and an overhead lintel.

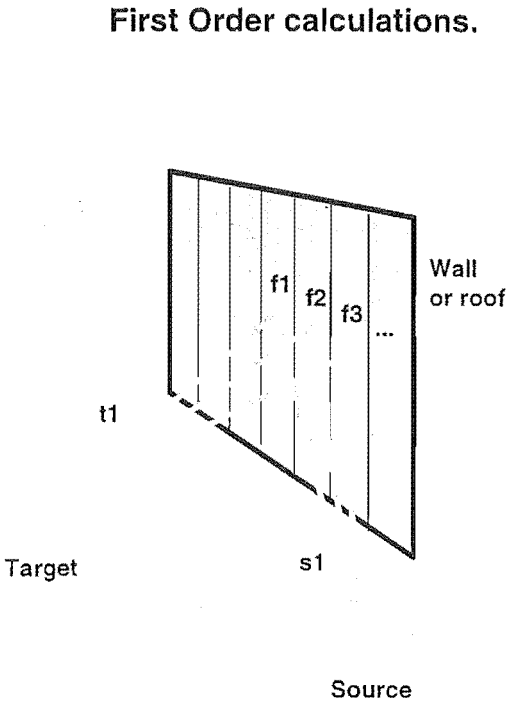

Figure 4.2: A method of determining scattered dose where the walls, floor and ceiling are divided into strips. The distances from the source to the scattering surface, (s1,s2,s3...). and the distances from the scatter to the exterior of the maze or a secondary scattering surface. (t1,t2,t3...) modify the dose according to the inverse square law. The coefficient of scatter or albedo (f1,f2,f3...) can be determined as a function of angle and material.

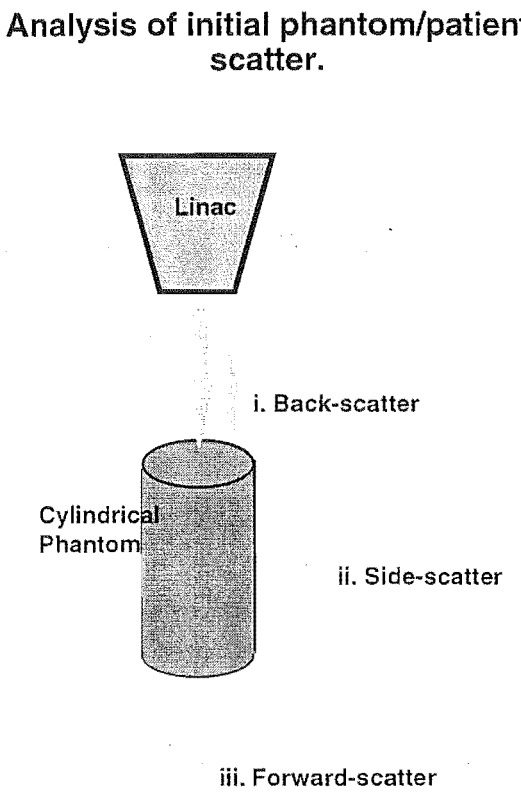

Figure 4.3: Determining the quality of scattered radiation.

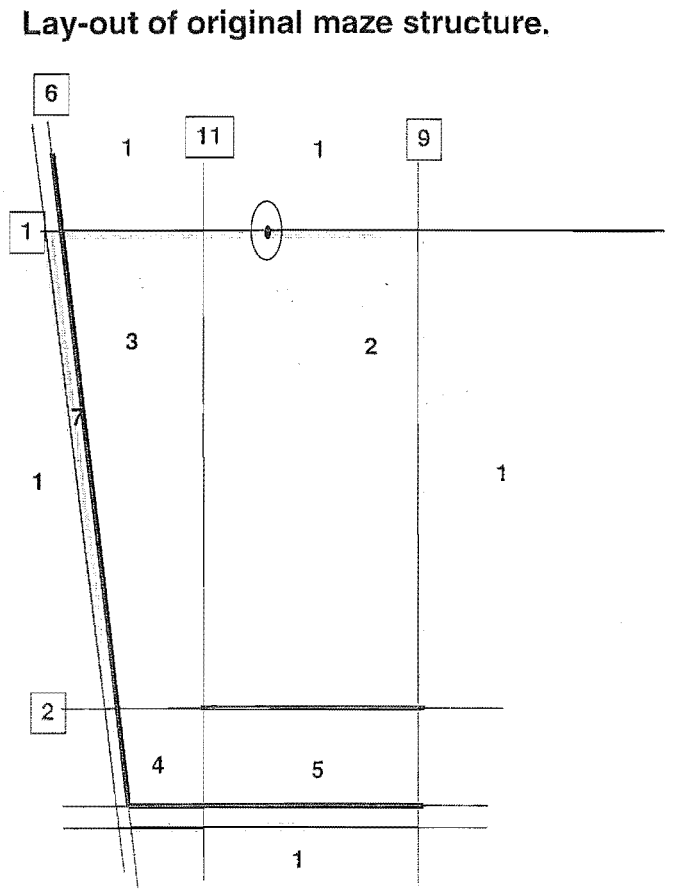

Figure 4.4: Geometrical layout in MAZE600c for the original bunker design.

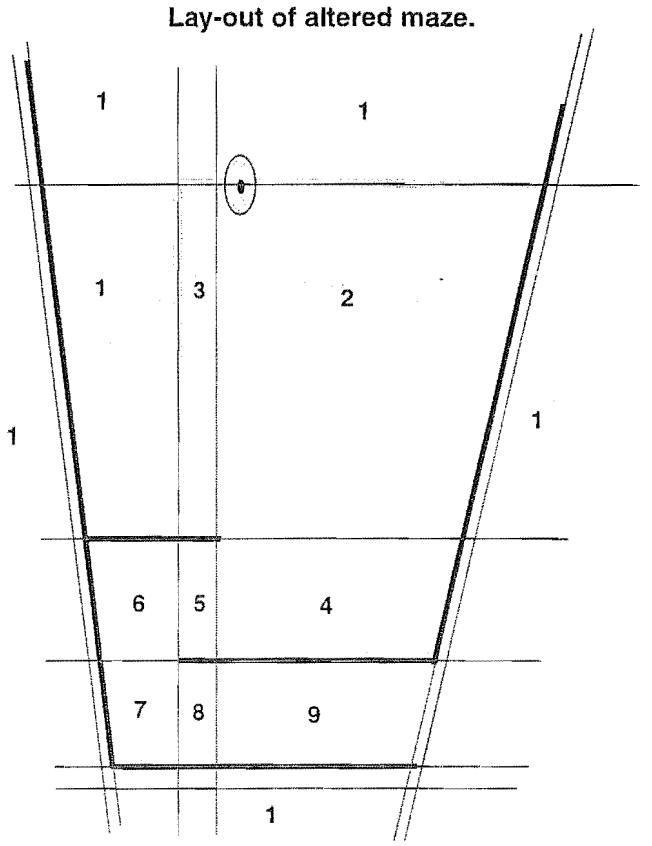

Figure 4.5: Geometrical layout in MAZE600c for the altered bunker design. Planes and the regions between them are labelled and used in the EGS4 HOWFAR and AUSGAB routines for boundary crossings and energy bookkeeping.

Required input	Example
Title	Approx configuration of **Treatment 1**
Number of histories	999
Initial RNG seed	123456789
Graphics file (0 none, 1 photons only, 2 full)	1
Number of media	2
Materials	AIR
	CONCRETE
number of interior surfaces	10
number of exterior surfaces	6
Planar inputs(cm)	320, 780
startx, starty,	640, 440
...	600, 0
	-40, 1
	-200, 160
	60, 580
	320, 360
	321, 200
	360, 201
	410, 460
	160, 700
	-350, 150
	-160, -70
	680, -71
	681, 440
	340, 780
lastx, lasty	320, 780
Ceiling/Floor thickness(cm)	20
Height of ceiling(cm)	300
Exit surface x1,y1,x2,y2	360, 780, 160, 700
Number of vertical structures	0
Direction of beam (0.0,0 for isotropic beam)	0, 0, 0
Source position	40, 390, 100
Particle charge	0
Initial Energy (MeV) (0 requests spectrum)	0
Spectrum input file	mohan10.spectrum

Figure 4.6: The format of the user input file for MAZE2D.

Chapter 5

Monte Carlo methods in the *in vivo* analysis of cisplatin uptake via X-ray fluorescence

5.1 Introduction

The *in vivo* measurement of heavy elements is of significant interest in the area of occupational medicine. The Total Body Burden for elements such as lead, mercury and cadmium may be assessed and an indication of exposure history indicated. Platinum in the form *cisplatin*, a cytotoxic agent, is nephrotoxic. It is therefore also useful to quantify *cisplatin* uptake *in vivo*.

Cisplatin is used in the treatment of several malignancies. X-ray fluorescence provides a means to access the uptake of the compound *in vivo* and specifically to assess renal nephro-toxicity.

5.2 Background

X-ray fluorescence with polarised X-rays is an established method for the *in vivo* measurement of platinum and other elements[128, 129]. Concentration and uptake of *cisplatin* can be inferred from the total platinum with concurrent measurements of cisplatin levels in blood plasma using atomic absorption techniques. Perhaps less well established is the collimator construction details for the source and detector, the optimum filter, and the material and construction of the polarising filter. It is also useful to optimise the peak kilovoltage/filtration in order to keep radiation doses to a minimum and extend the lifetime of the X-ray tube.

The Klein-Nishina cross-section for linearly polarised photons is,

$$\left(\frac{\mathrm{d}\sigma}{\mathrm{d}\Omega}\right) = \frac{1}{4}{r_0}^2 \left(\frac{\varepsilon}{\varepsilon_0}\right)^2 \left(\frac{\varepsilon}{\varepsilon_0} + \frac{\varepsilon_0}{\varepsilon} - 2 + 4\cos^2\Theta\right) \tag{5.1}$$

where r_0 is the classical electron radius, ε_0 and ε are the incident and scattered photon energies and Θ is the angle between the incident and scattered vectors of polarisation.

By considering polarisation vectors parallel and perpendicular to a plane formed by the initial direction of polarisation and the direction of photon scatter and summing the result, a cross-section can be formed in terms of the polar angle, θ, the angle between the direction of incidence and the direction of scatter, and the azimuthal angle, ψ, the angle of rotation of the scattered radiation in relation to the incident angle of the polarisation vector. Hence,

$$\left(\frac{\mathrm{d}\sigma}{\mathrm{d}\Omega}\right) = \frac{1}{2}{r_0}^2\left(\frac{\varepsilon}{\varepsilon_0}\right)^2\left(\frac{\varepsilon}{\varepsilon_0}+\frac{\varepsilon_0}{\varepsilon}-2\sin^2\theta\cos^2\psi\right) \tag{5.2}$$

The cross-section reachs a minimum, for a polar scattering angle of 90^0, when the azimuthal angle is zero. For photons energies in the region of K-fluorescence, where the difference between incident and scattered energies is small, the minimum cross-section is effectively zero.

The azimuthal dependence of Compton scatter for polarised sources of radiation can be used to improve the sensitivity of a detector to fluorescence photons which are produced in an isotropic fashion. Polarised photons can be produced from a number of sources including synchnotron radiation. However, the demands of an *in vivo* method are such that high exposure rates are required. A polarised X-ray source can be generated by scattering the radiation of a, therapy intensity, X-ray source at right angles. According to equations 5.1 and 5.2, the scattered photons will acquire a polarisation that is orthoganal to the angle of scatter. This is the origin of the mutual orthoganal arrangement of source, scatterer, sample and detector. In practice, a minimum of Compton photons, as described above, is not achieved due to multiple Compton scatterings of the photons in the sample.

An X-ray tube has been employed in contrast to radioactive sources such as ^{109}Cd, ^{57}Co and ^{99}Tc. The nearest reactor facility to Christchurch is at Lucas Heights in Australia therefore the cost of using isotopes is prohibitive. A judiciously filtered X-ray source is therefore a preference. The tube, sample and cryogenic germanium detector are fixed in a mutually orthogonal arrangement that minimises the Compton background seen by the detector (figure 5.1).

Further gains can be achieved by choosing a range of incident bremsstrahlung photons that provides an optimum of photoelectric events in the sample while minimising Compton events that will tend to swamp the fluorescent peak.

Initial difficulties in resolving detectable levels of platinum with this method were found to be caused by an inadequate tube voltage and as the transport of particles in the detector arrangement is reasonably complex it was felt that this was a worthy project to apply Monte Carlo methods to. Consequently

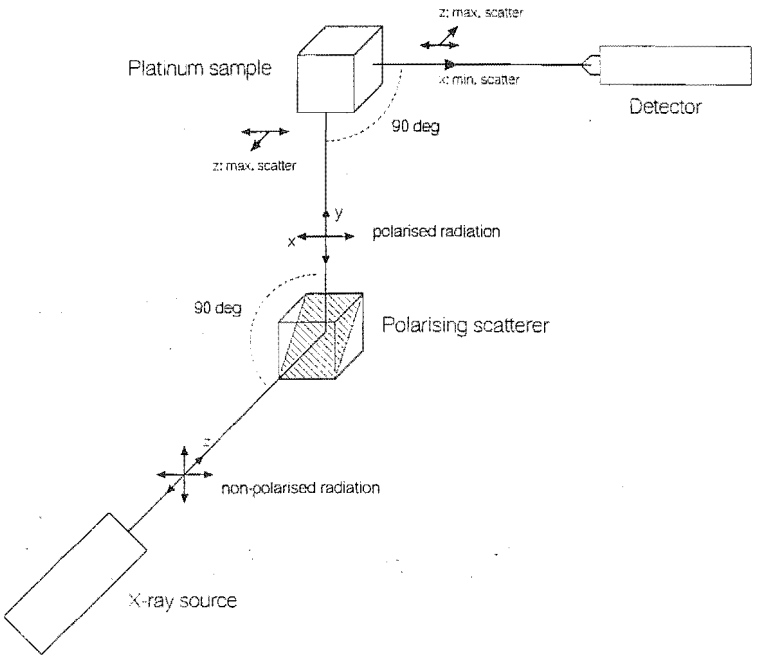

A mutually orthogonal arrangement of X-ray source, scatterer, sample and detector designed to minimise Compton scatter contributions.

Figure 5.1: XRF geometry.

Monte Carlo techniques have been used to examine detection efficiency and to examine the effects of variations in source energy and collimator and filter construction.

The motivation for a Monte Carlo analysis of this problem is that the method enables a number of competing effects to be considered separately, i.e. processes can be switched off. Monte Carlo will also more accurately account for the multiple Compton scattering events that will occur in the medium which will tend to reduce the efficacy of this particular geometrical arrangement.

A recent extension to the EGS4 library of codes, LSCAT[93, 94, 102, 95], enables the effects of polarisation on the Compton component to be considered. This code also resolves a number of low-energy transport issues including account of bound Compton scattering and Doppler broadening. Linear polarisation effects have only recently been included in Monte Carlo analysis of this nature [137, 230]. Fluorescence in multiple element media is enabled using code extensions also to be found in the LSCAT distribution and a simple patch to the single element method[91].

5.3 Implementation

The code referred to as XRFCOMP in this document is a user-code that requires the standard EGS4 distribution plus the LSCAT distribution obtainable from the Japanese high energy facility, KEK. The authors of the LSCAT extension to EGS4 would wish that you contact them. A number of important points, in particular departures from standard EGS4, are described as follows and illustrated in figure 5.2.

In subroutine MAIN, flags are set for linear polarisation and fluorescence. The atomic number of the fluorescing element, Pt (Z=78), is set for the sample region and the subroutine EDGESET is called. The flags IAUSFLG(20) and IAUSFLG(21) are set for exceptional entry into AUSGAB in this case before and after photoelectric events respectively. It is important to distinguish these calls in AUSGAB so that normal energy summation does not occur. Instead the calls are used to exchange medium types for multiple element fluorescence. Hence before a photoelectric event in the sample region a branching ratio is determined for the elements of mixture and the region number is switched to enable PHOTO to determine the appropriate fluorescent product. It is useful to set LATCH at this point if a Pt fluorescence is to occur. After a photoelectric event the second call to AUSGAB switches the region number back to that of the original sample region.

In HOWFAR an improvement in fluorescent photon statistics is achieved by transporting a photon that has LATCH set through the phantom medium to a spherical surface equivalent to the depth of the sample. All photons reaching the surface are counted at the detector because the fluorescence component is isotropic. Figure 5.3 shows the geometrical layout of XRFCOMP.

The two routines COMPT and APHI form the basis of the LSCAT distribution and are to be found in the file LSCAT.MOR. A modified COMPT subroutine handles differences in the way cross-sections are calculated with linear polarisation. APHI is a new routine that handles calculation of azimuth angle depending on the electric field vector and recalculates the scattered photons electric field vector.

Simulations were performed for tube voltages in the range 110 to 150 kVp. These spectra were determined using the method of Birch and Marshall[231]. In this work we wish to determine the size of the platinum K-α peaks in comparison to the Compton background. To perform this calculation spectral data is only required for X-ray photons of this range and higher and is unmodified by the presence of a tungsten peak. A useful approximation is that the intensity at the high end of the spectrum is proportional to $(T - E)/E$ where T is

the kinetic energy of the incident electrons (in most cases approximately the kVp of the tube) and E is the energy of the scattered photon. The effects of filtration are subsequently ignored.

5.4 The minimum detectable concentration

The detection limits for this technique depend on the degree of noise in the continuum and is consequently influenced by the X-ray tube fluence, read-in time and detector efficiency. Ultimately the counts at the detector are limited by a tolerable absorbed dose to the patient although steps can be taken to reduce this (ie the use of a high atomic number filter). These considerations are unrelated to the determination of an optimal detector arrangement, however, it is useful to be able to relate the values obtained in our calculations to actual values of minimum detectable concentration (MDC). This can be achieved in the following method.

Firstly an MDC is determined from experiment[34]. Our Monte Carlo calculations can determine the fraction of fluorescent photons to Compton photons to an arbitrary degree of precision within a particular energy range. If we scale this fraction so that the Compton background is equivalent (note that this relates to an equivalence of absorbed dose) then the MDC is inversely proportional to the size of the photopeak. Hence the MDC can be calculated from a Monte Carlo calculation where the quantity of the fluorescing photons as a fraction of background photons in the specified energy range can be easily determined. We have calculated such values for the two K-α peaks in the energy range 64 to 70 keV.

In an arrangement using a 115 kV_p tube and a cisplatin sample of Pt, concentration 615 ppm ($\mu g\ g^{-1}$), in a small water phantom, an MDC of 50 ppm has been determined. The MDC corresponds to a detectable fraction of one fluorescent photon to 111 background (Compton) photons, in the range specified, per 100 ppm of Pt.

5.5 Variance reduction

The dual scatter arrangement associated with this technique leads to a number of calculational issues relating to the variance of the particle count at the detector surface. The relatively large fluence of the tube is quickly reduced to a small fraction (in our arrangement 5×10^{-8}) at the detector. This poses problems for Monte Carlo routines that can cope adequately with 10^8 photon histories (3-4

hours) but quickly reach an intolerable execution time beyond this. A number of variance reduction techniques can be used including particle splitting. For example in XRFCOMP the small fraction of photons reaching the phantom are split into a more useful number of photons which are subsequently transported through the phantom and sample. Advantage can be made of the inherent geometrical symmetries in this problem. Fluorescing photons in the sample region are produced isotropically and can therefore be transported directly to the phantom surface and accumulated. It is not necessary to transport them to the detector in the usual manner because these photons leave the sample volume in an unbiased manner. On the other hand the partially polarised Compton background is highly spatially dependent although two "detector" surfaces can be employed in the two mutually orthogonal directions improving statistics by a factor of two.

5.6 Results

XRFCOMP has been used to examine the trend in minimum detectable concentrations with tube kV_p. The lack of sufficient high-end contributions in the 115 kV_p spectrum (figure 5.4) demonstrates why XRF is not particularly successful at this tube voltage. The results of comparisons over a range of tube voltages are shown in figure 5.5 and indicate that a substantial improvement in MDC can be achieved by raising the voltage to 150 kV_p. Further increases in kV_p have to be weighted against the corresponding increase in absorbed dose and the code provides facility for analysing this effect. A brief examination of scatterer material supports earlier findings that copper is a superior scatterer material as it leads to improved MDC values for an equivalent level of absorbed dose. These considerations will be influential in designing subsequent manifestations of the detector system.

5.7 Conclusion

The *in-vivo* analysis of cisplatin has been investigated using an extension to the standard EGS4 library of code. Further research will include the application of the technique to the *in vivo* monitoring of the uptake of environmental heavy metals such as lead and cadmium. The code developed is portable and easily modified and will be made freely available to those investigators wishing to perform similar calculations.

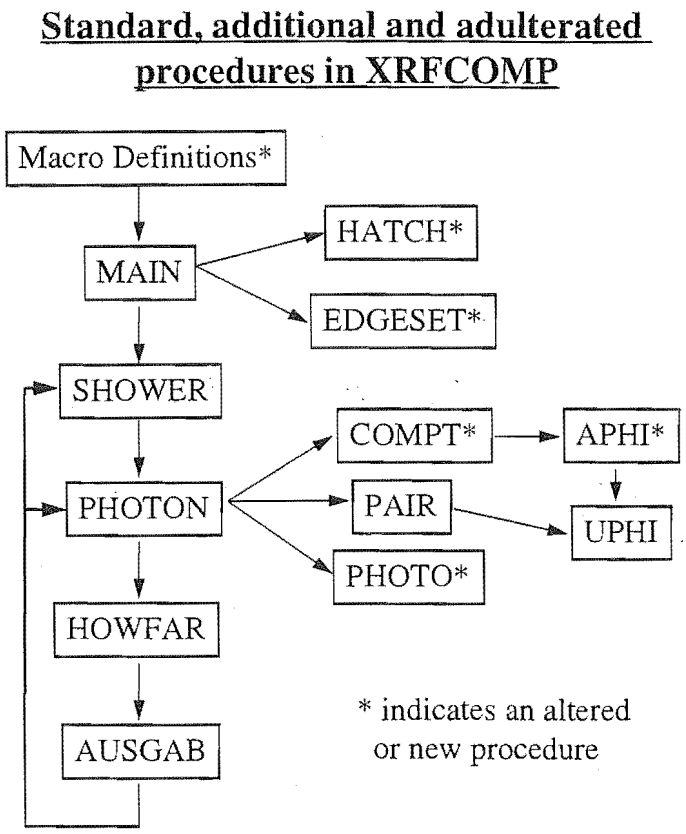

Figure 5.2: Standard, additional and adulterated procedures in XRFCOMP. EDGESET is not standard EGS4 but is necessary for K-fluorescence. APHI stands for anti-uniform phi distribution which depends on the electric field vector used in linear polarisation.

Regional lay-out for XRFCOMP code.

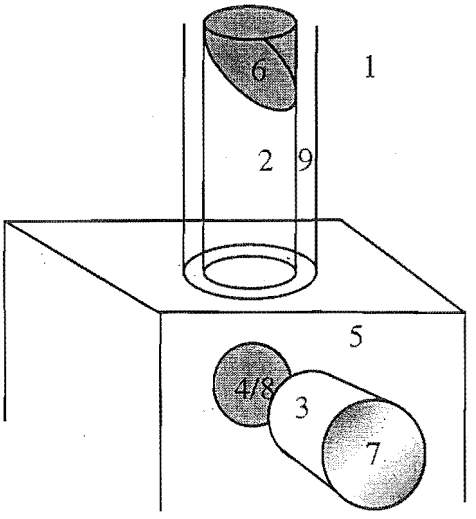

1. Throwaway region
2. Collimator from scatterer
3. Collimator to detector
4. Sample region
5. Phantom
6. Scatterer
7. Detector surface
8. Alternative fluorescing region
9. Brass collimator

Figure 5.3: Regions in XRFCOMP.

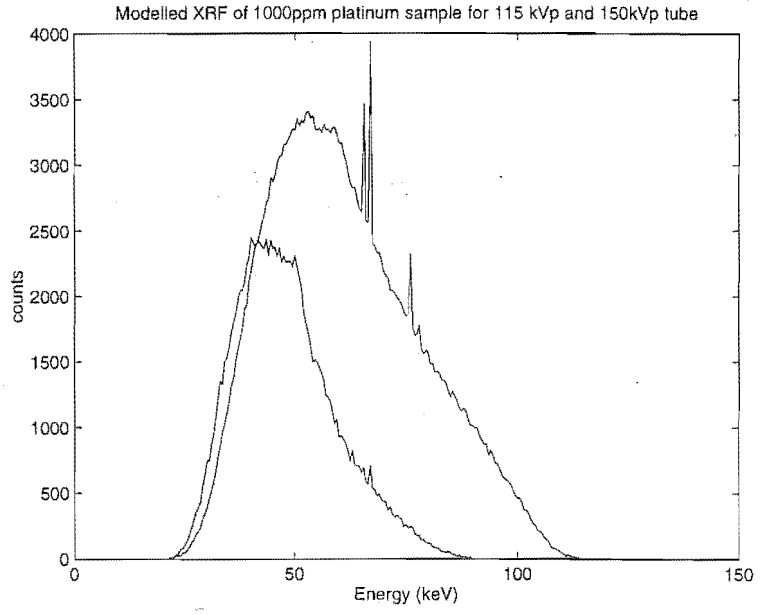

Figure 5.4: Modelled X-ray fluorescence of a 1000ppm platinum sample for a 115 kV_p and a 150 kV_p tube.

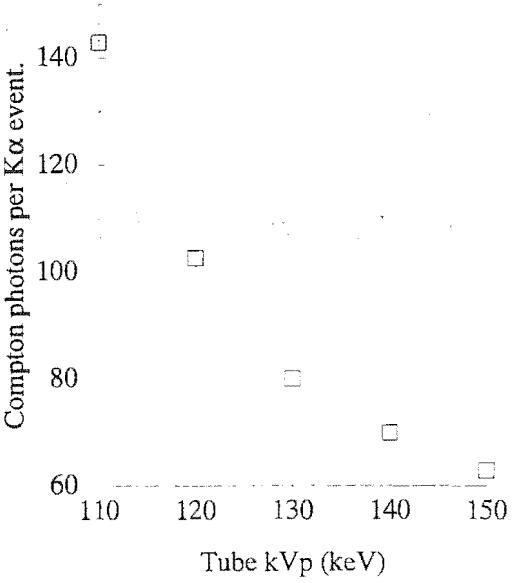

MC determined trend of Compton background events in the range 64keV to 70keV to fluorescent events at the detector with tube kVp. For a given Compton background this is proportional to the MDC.

Figure 5.5: Monte Carlo determination of the minimum detectable concentration.

Chapter 6

Monte Carlo based dosimetry for superficial X-ray therapy and brachytherapy.

6.1 Introduction

In this chapter Monte Carlo based methods of determining dose distributions and back-scatter factors for superficial therapy dosimetry and brachytherapy dosimetry are considered.

Dosimetry practices in the superficial therapy regime have come under recent scrutiny[232, 233] and recommendations for appropriate methods of measuring absolute dose have been forthcoming. In Nahum (1996) superficial modalities are divided into two groupings. "low-energy X-rays" and "very low-energy X-rays".

"Low-energy X-rays" are generated by tube potentials between 50 and 160 kV_p. The recommended procedure for the determination of absolute dose at these energies is to use a cross calibrated thimble chamber and to perform the tube output measurement in air. To determine the dose to the surface of a phantom or patient it is necessary to multiply the output by a backscatter factor. These factors are tubulated for ranges of tube voltages or half-value layers (HVL).

Tube voltages between 8 and 50 kV_p are said to generate "very low-energy X-rays". This energy range is sometimes called the Grenz-ray region[234]. Due to a substantial energy dependence in cylindrical chambers at this energy it is now not considered practical to use these chambers for cross calibration at these energies and instead it is recommended that a parallel plate chamber such as the Markus or NACP chamber be used. These chambers have quite a significant material supporting structure which will produce back-scatter into the dose sensitive region and as such are really designed for in-phantom measurements.

6.2 Determination of spectra for superficial X-rays

We have set about determining backscatter factors for the full range of modalities found on the Philips RT100 unit at the Christchurch Oncology Service namely 20 , 37 , 55, 85 and 100 kV_p. This is in contrast to the recent recommendations.

Other means of determining spectra in this energy regime are attenuation methods[235, 236, 237, 238, 239, 240], indirect scattering methods[241] and semi-analytical constructions[231, 242, 243, 244].

The results of simulations in semi-infinite homogeneous phantoms are compared with depth-dose curves from the literature. Two methods of direct measurement have been investigated at Christchurch Hospital, namely thermoluminescent dosimeters in a water phantom and radiochromic films in a plastic (PMMA) phantom[43]. Absolute dose at the surface is calculated from in-air ionisation-chamber measurements and used to calibrate the dosimeters for the range of modalities. Tabulated values of back-scatter factors are therefore examined and a Monte Carlo method is used to complement literature values for the range of spectra examined. Careful consideration has been made of the lower energy contributions to the spectrum, such that reliable back-scatter factors are determined. Finally, information about the beam spectrum can be used to predict the variation in detector response with beam energy can be used to infer the change in response with depth.

6.2.1 Acquisition of incident spectra from a germanium detector

It is our aim to use the Monte Carlo method to determine the dose distribution and back-scatter factors associated with these therapies. To do so it is necessary to determine a source spectrum. It would also be useful to know the distribution of particle trajectories emerging from the source. The combined information is often referred to as the phase-space distribution of the source. In chapter seven we will introduce a notation that enables such a fuller analysis. However, in this chapter we restrict ourselves to an analysis of source spectrum only and make certain assumptions about the beam cross-section.

The source spectrum for each superficial modality has been determined with a high-purity germanium detector (Model GLP-36385/10-P).

The high flux of the the unmodified beam has to be reduced with a combination of increased source to detector distance and fine collimation with lead sheets[140, 141]. The processes of in-air attenuation, collimator perturbation, K-edge and Compton loses at the detector, cause perturbations in the measu-

red spectrum.

6.2.2 Conversion of raw to real spectra

The usual manner of converting measured pulse-height distributions into real spectra is called stripping[139, 142, 144]. Interactions in the intervening media and scattering within the scintillating crystal lead to energy loses. Consequently particles originating at the high end of the spectrum acquire a lower energy signature that is characteristic for that energy. It is therefore possible to correct the pulse height distribution starting at the uppermost energy and subtracting (or stripping) those contributions at a lower energy that are due to this higher energy event. The algorithm proceeds downwards through the pulse-height distribution subtracting the lower contribution and re-appropriating the events to the upper end of the spectrum. An example of a stripping algorithm is presented by Seelentag and Panzer[142].

If we were to represent this procedure in a matrix form there are some rather interesting properties. We define the incident spectrum by a vector, $\mathbf{s}$. The incident spectrum is related to the measured spectrum, $\mathbf{b}$, by the processes of radiation transport and loss, represented by a matrix M, where

$$M\mathbf{s} = \mathbf{b}. \tag{6.1}$$

The matrix, M, can be determined and in our case we have used the Monte Carlo method. A column element of M is the theoretical deposition of energy in the crystal (the pulse-height distribution) due to a single energy of incident photon represented by a row position in the columnar matrix, $\mathbf{s}$.

To determine the incident spectrum, $\mathbf{s}$, matrix M is inverted, ie.,

$$\mathbf{s} = M^{-1}\mathbf{b}. \tag{6.2}$$

As has been stated, the measured events form a distribution that lies below and includes the incident energy therefore the matrix M has upper triangular form and is easily inverted. In fact the process of inversion for a matrix of Row-Echelon form such as this is a back-substitution. The back-substitution procedure is formally equivalent to the process of stripping described above.

Where it is the goal of a calculation to determine a quantity such as the incident spectrum from an indirect measurement it is necessary to determine an inversion of the physical processes can contribute to the physical measurement. Chandrasekhar observers "that it is the Fourier transform of the probability

function, rather than the function itself that has a more direct relation to the physical situation"[47]. More will be said about this paper in chapter seven.

This technique has been implemented in the Monte Carlo user-code, GE, the matrix manipulation was performed using MATLAB. In the code, GE, the measured spectrum is used as an approximation to the real spectra and transported through the germanium crystal. The dimensions of the crystal are used but a wide tolerance for crystal dimension can be demonstrated. The crystal is 13 mm thick and 36 mm in diameter. The detector has a beryllium window of thickness 0.254 mm. The absorption due to the window places a lower limit on the photon energies observed. A 3 keV photon suffers one HVL through the window whereas a 1 keV photon would need to traverse 28 HVLs and is not likely to be seen by the detector.

Figure 6.1 graphically represents the matrix, M, determined for the 100 kV_p modality.

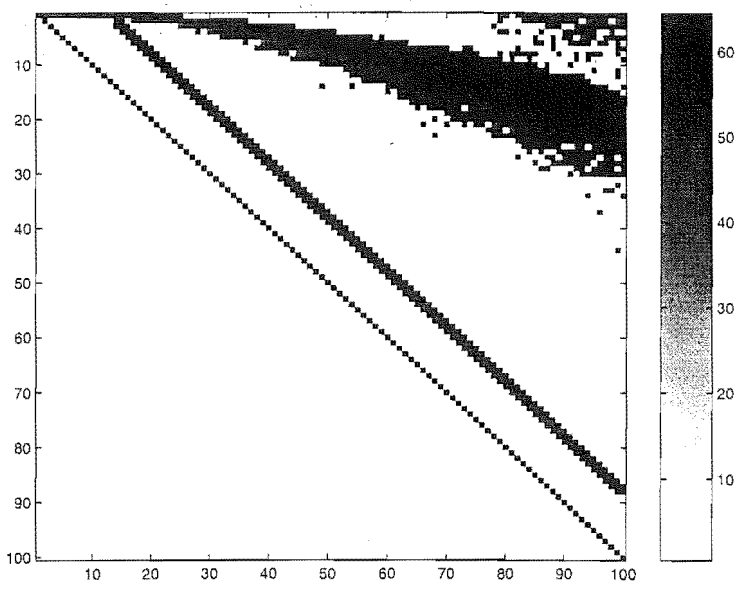

Figure 6.1: Representation of the matrix, M, for the 100 kV_p modality on a Philips RT100. The intensities in the graph are a logarithm of the values in the matrix.

Columns of the matrix indicate the deposition of energy. The central diagonal represents the main photopeak. A single K-fluorescence within the germanium detector that subsequently escapes leads to a band of lower contribution with the energy of the incident particle less that of the K photon. Compton scattering out of the detector occurs over a broad range but as most escaping photons must be either backscattered generating a moderate energy electron

or highly forward scattered depositing only a residual energy. Multiple scattering processes are also inclined to occur and can be observed in contributions above the Compton edge.

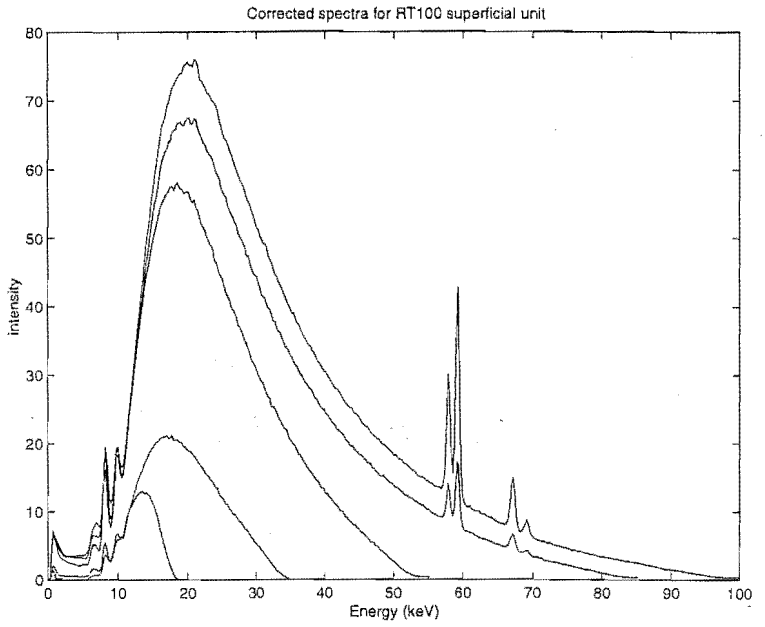

Figure 6.2: Corrected unfiltered spectra from a Philips RT100 measured with a high-purity germanium detector.

Figure 6.2 shows the corrected spectra for the RT100 unit.

6.3 Forward Monte Carlo calculations

Monte Carlo methods are an appropriate method of dosimetry at superficial energies. The calculations are fast as it is tolerable to exclude the transport of secondary electrons. Certainly for less regular dosimetry such as the determination of depth dose curves in homogeneous phantoms, Monte Carlo provides a useful supporting role.

6.3.1 Backscatter factors

Back-scatter factors are generally obtained from published sources of backscatter factor versus the field size and half-value-layers for a range of therapy units. There are also published tabulated depth-doses for ranges of superficial energy. To calculate a backscatter factor it is useful to consider a primary then

secondary scatter approximation. The multiple scattering solution is calculated appropriately using the Monte Carlo method.

The determination of a back-scatter factor proceeds with the measurement of the mass absorption coefficient, μ_{ab}/ρ, which is the transfer of photon energy to absorbed dose in the medium. Tables of μ_{ab}/ρ as a function of photon energy for each of the principle interactions are well established and can be considered to be accurate[245, 246]. The values in these tables are measured under strict experimental conditions. If tables of μ_{ab}/ρ are used then the spectrum must be known with accuracy. Particularly at the lower (sub 10 keV) end of the spectrum the value of μ_{ab}/ρ tends asymptotically towards infinity. The trend is a reflection of the high degree of absorption at these lower energies. It is therefore paramount that an accurate representation of the lower energy component be determined.

A backscatter factor is the ratio of the absorbed dose in a semi-infinite phantom (a combination of primary and scattered radiations) over the absorbed dose to an isolated material of infinitesimal mass at the same geometrical point in space.

$$B = \frac{P+S}{P} \tag{6.3}$$

In a semi-infinite phantom full scatter conditions occur in the forward direction. If we exclude the scatter contribution the minimum value that a backscatter factor can take is unity.

Primary and scatter doses are related to the incident and backscatter differential fluences, $d\phi_0/dE$ and $d\phi_m/dE$ (spectra) in accordance with the usual definition

$$\begin{aligned} P &= \int_0^{E\max} \frac{d\phi_0}{dE} E \left(\frac{\mu_{ab}(E)}{\rho}\right) dE \\ S &= \int_0^{E\max} \frac{d\phi_m}{dE} E \left(\frac{\mu_{ab}(E)}{\rho}\right) dE \end{aligned} \tag{6.4}$$

where μ_{ab} is a linear transfer attenuation coefficient and is a function of the absorbing material as well as the energy[153].

A single scatter approximation to the scatter contribution can be determined as a function of Compton and Rayleigh cross-sections and is again a lower limit to the backscatter factor. Here we will examine the multiple scatter limit to the scatter contribution using Monte Carlo. Two methods are available to us. We can determine a back-scatter fluence and use equations 6.3 and 6.4. Alternatively we can use Monte Carlo to determine primary and primary plus

scatter doses within a limiting volume. In fact we have done both. Further the same calculation will give us a dose versus depth relationship.

6.3.2 Monte Carlo calculations

A user-code, SUPERBS, has been designed to use the incident superficial spectra measured and corrected in the previous section. The code determines the ratio of absorbed dose for primary and for full scatter conditions at the same time. The primary dose is determined from the energy deposited in the first interaction and subsequently ignored.

This method is a very simple example of a correlated sampling technique[247] where a quantity, often the ratio of two doses, is calculated for each history, with the same starting conditions and sequence of random numbers. The variance in the quantity is less than if the radiations were transported independently.

While the primary absorbed dose is easily determined, using equation 6.4 and the incident spectrum, this method does not appear to be particularly advantageous. However the effort required to determine a scatter contribution justifies the small overhead required to determine the primary contribution on-the-fly.

The scatter contribution is determined in a small limiting volume. The consequence for a Monte Carlo calculation is that large numbers of particles must be generated over a broad spatial range and and after transport has occured accumulated in a infinitesimal volume leading to poor statistics or long calculation times. The reciprocity theorem provides a means to improve the statistics.

The reciprocity theorem states that the dose deposited in a small volume within a semi-infinite phantom by a broad parallel beam is equivalent to the dose deposited by a small field within a broad detector volume.

The width of the "detector" volume becomes the beam width. In the calculation the thickness of the detector volume is reduced asymptotically to zero. This can be achieved by performing the calculation in a multiple layered geometry with the width of each layer a value deemed small enough. A plot of the backscatter factor versus detector thickness can be constructed and the limiting value can be determined by extrapolation to zero. This method is similar to that of Patrocinio *et al*[153].

We use a geometry consisting of ten 1 mm semi-infinite slabs and a region below the slabs of infinite thickness. Depth-dose curves for each modality are determined and shown in figure 6.4

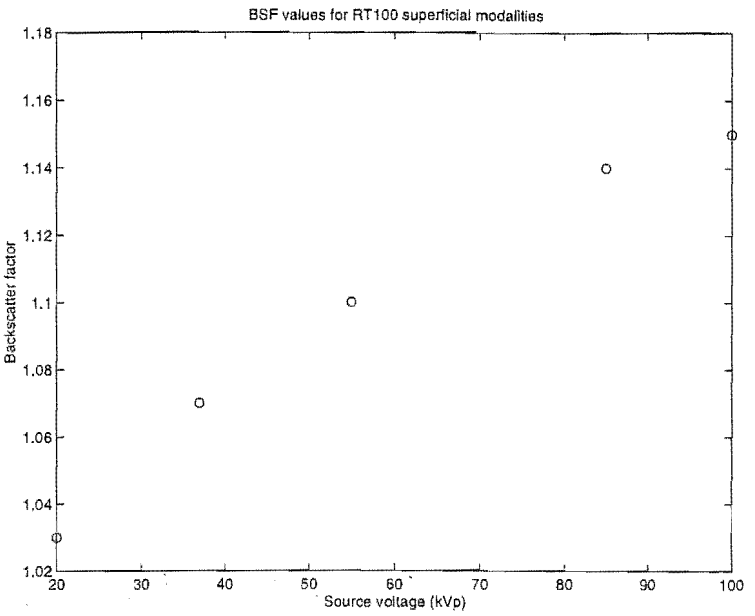

Figure 6.3: Backscatter factors determined for the Philips RT100 superficial X-ray unit. A Monte Carlo method is used incorporating Compton, Rayleigh and Photoelectric cross-sections with photons transported down to 1 keV. The X-ray source spectra were determined with a germanium detector.

Backscatter factors are determined for each modality and shown in figure 6.3. Percentage depth-dose curves (figure 6.4) are generated from the same Monte Carlo calculations. They have been normalised to the dose at the surface using the back-scatter factors from the figure and a primary (surface) dose determined using equation 6.4. The mass transfer coefficients were obtained from Johns and Cunningham[14]. The degree of mismatch between the depth doses and the surface doses is not entirely due to the variance (approximately 1% in the backscatter factors).

It is possible to check photon attenuation coefficients that are pre-calculated by EGS4 using the program EXAMINE. Comparing these tables would be useful. However there is now good indication that standard EGS4 is not particularly accurate in this energy range. The next step would be to include the KEK extensions to EGS4 used in chapter four.

Some discussion has recently been raised about the quality of the various tables of attenuation data available[246]. The photoelectric cross-sections in EGS4 have been taken from Storm and Israel[245]. Comparison with the Lawrence Livermore National Laboratory demonstrate an average difference over of 2.7% for the mass transfer coefficient, μ_{ab}, used here. Water (our basis

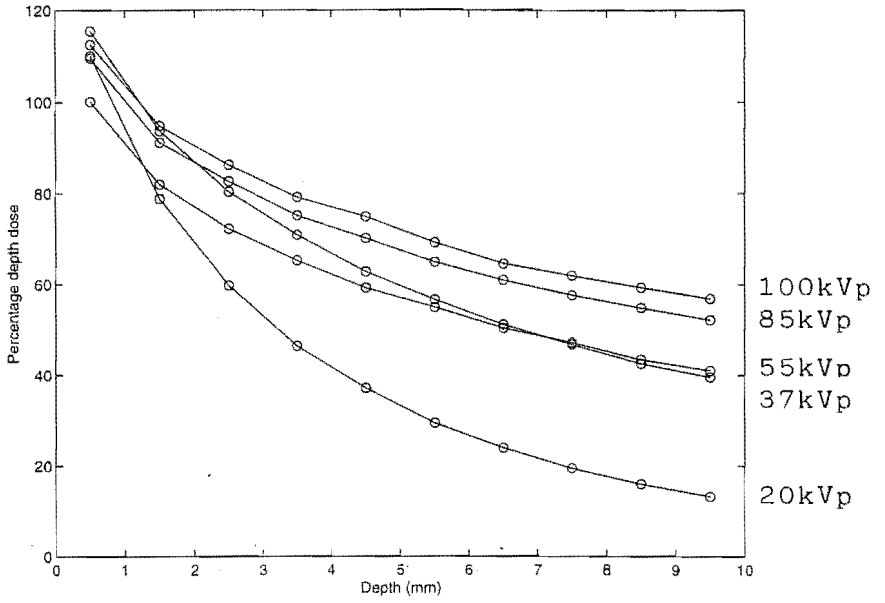

Figure 6.4: Percentage depth doses determined for the Philips RT100 superficial X-ray unit. A Monte Carlo method is used incorporating Compton, Rayleigh and Photoelectric cross-sections with photons transported down to 1 keV. The X-ray source spectra were determined with a germanium detector.

for dosimetry) is typical.

6.4 Conclusion

In this chapter we have discussed a method of dosimetry for superficial therapy. Firstly an inverse method is used to "tune" a measured data set in an effort to determine a physical quantity. The physical quantity is the spectrum and is essential for a forward calculation of a theoretical nature such as Monte Carlo. In fact, the conversion of a pulse height distribution in a germanium detector to a spectrum is reasonably trivial, at least in terms of equation we are inverting. None-the-less, this a perfectly reasonable example of a dosimetry that requires both forward and inverse methods.

A number of workers have determined superficial and diagnostic energy spectra using attenuation methods in a manner first described by Silberstein[235]. Here is a case where inversion techniques are absolutely required. The resulting spectrum is adequate for characterising beams but certainly much better results are obtained using a germanium detector. Boone[242], however, ar-

gues in support of such techniques, as attenuation in tissue is the important parameter in the clinical setting.

As it has been possible to determine good quality spectra from our RT-100 superficial unit, this is an interesting exercise. The back-scatter factors and depth-dose data presented here are for the unfiltered beam and would need to be modified for clinical application which uses a range of filters. Monte Carlo is of course an excellent way to simulate the effects of filters, of treatment cones and of tissue inhomogeneities.

In chapter seven we will be examining a method of determining electron spectra and we will find that the same arguments apply. We propose a method that is similar to the attenuation technique, in that it uses in-phantom measurements of dose. This method has a significant historical precedent, in that most megavoltage photon and electron dosimetry proceeds with measurements in a water tank.

Chapter 7

Stochastic methods for the reconstruction of electron therapy beams

7.1 Introduction

In this chapter we examine the use of Monte Carlo simulation for predicting electron distributions in number of patient treatment scenarios. In the same manner as in chapter six we look at the determination of incident beam information. Whereas with superficial X-rays it is possible to perform a reasonably direct measurement of the spectrum, with electron beams this is more difficult. To achieve this several workers have used a magnetic spectrometer[248, 249, 250, 251]. In general this equipment is not available to oncology departments and alternative methods are required.

To demonstrate the need for accurate spectral information for Monte Carlo based dosimetry, figure 7.1 shows a depth-dose curve calculated using EGS4 for a 20 MeV monoenergetic electron beam. This is compared to depth-dose data for the 20 MeV modality on a Varian 2100C linear accelerator with a 10x10 applicator setting and depth-dose for the same collimator jaws setting (14x14) but minus applicators. The difference between the monoenergetic depth dose and the standard clinical setting is substantial. indicating the need to use carefully determined spectra in Monte Carlo based treatment calculations. The difference between the applicator and non-applicator depth-dose indicates the deposition of secondary scatter electrons at the central axis originating in the electron applicator cones. A significant difference between the Monte Carlo generated depth-dose and the applicatorless measurement suggests a broadening and softening of the incident electron beam in the collimators and other head componentry.

The interest in electron dosimetry at this energy arose from concerns associated with the use of electron beams to treat deep seated tumours. As has been mentioned, therapy electrons suffer a high degree of scatter in air. The applicator cones (see appendix two) are designed to redefine the electron beam close to the patient and often "cut-outs" are used to define a specific beam

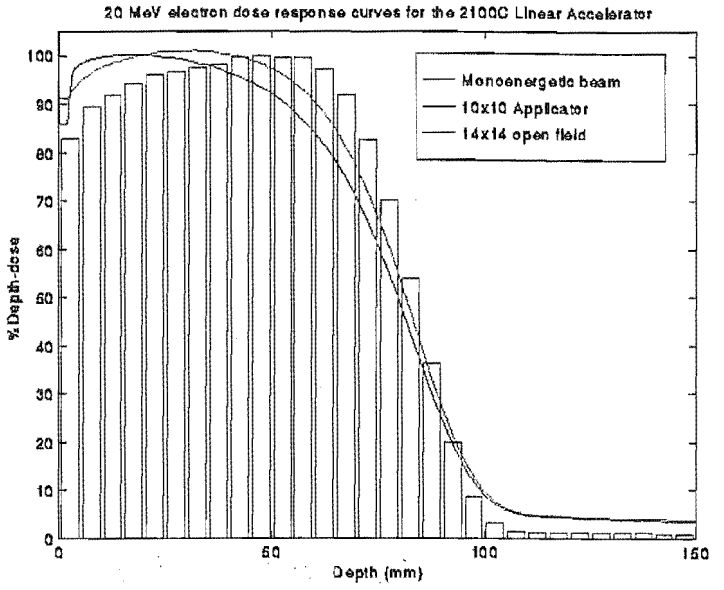

Figure 7.1: Depth-dose curves for 20 MeV electron monoenergetic source (histogram) calculated using EGS4, the 20 MeV modality on the Varian 2100C linear accelerator with a 10 cm × 10 cm applicator cone (upper continuous line) and without the applicator cone (lower continuous line). The accelerator jaw setting is 14 cm × 14 cm. The measurements were performed in a water phantom using a Markus chamber.

shape. The cut-outs are fashioned from cerrobend, a low melting point, high density, eutectic compound. With the 20 MeV electrons modality there has been some concern that the cut-outs were not eliminating the electron beam at the edge of the defined field. Monte Carlo calculations with monoenergetic beams were found to be inadequate as is demonstrated in figure 7.1.

7.2 The inverse Monte Carlo method

The inverse Monte Carlo method was introduced by Dunn[145]. He was able to demonstrate some useful applications to the design of photon beam compensating filters[146]. The method has been used in SPECT (single photon emission CT) reconstructions[252, 253, 254, 255]. Lind and Brahme suggest the method for inverse planning[256]. The method has similarities to a variance reduction method called importance sampling[82].

Importance sampling is used, for example, in photon transport problems where it may be desirable to force an interaction to occur within a certain

volume. The distance between interactions is given by $s = -\lambda \ln[1 - \xi]$ where ξ is a uniform probability distribution in the interval $(0, 1)$. To force an interaction to occur within a range, Δ, the probability distribution is multiplied by a factor $(1 - e^{\Delta/\lambda})$ as is the weighting on the particle.

The reader has been introduced briefly to the inverse Monte Carlo method in the previous chapter. In that case the relationship between a measured quantity (the pulse-height distribution) and a theoretical quantity (spectrum) was straightforward. With the case of electron therapy dosimetry we are interested in determining spectral information from in-phantom measurements. This technique has been used by several workers[257, 258, 259] but it is surprising, given the radiation properties of electrons, that the technique has not been more widely applied.

The monoenergetic electron dose distribution has a rather interesting mathematical property, unlike the photon dose deposition it has a finite range. The physical reason for a finite range has been discussed in the introduction. If in the same manner as the previous chapter we construct a matrix where each column represents the relationship between the incident energy of a single electron and its subsequent deposition in-phantom we would find that the distribution is also upper-triangular in form. The implication is that a solution will be easily formed.

The first of our examples examines the depth-dose curves of a 20 MeV modality electron beam for a 10 cm $\times$ 10 cm applicator cone. Depth doses were measured with a Markus chamber in Solid Water[216]. Sets of monoenergetic 10 cm diameter electron beams were simulated using EGS4 and the PRESTA extension[89]. The data set is presented in figure 7.2 and is approximately of an upper-triangular matrix form.

The central-axis depth dose is given by,

$$\mathrm{DD}_{modality}(z) = \int_0^{E_{nominal}} \mathrm{DD}_{\bar{e}}(E, z) \frac{d\Psi(E)}{dE} dE + \Gamma(z). \tag{7.1}$$

where $d\Psi_{\bar{e}}(E)/dE$ is the incident electron spectra (a differential fluence). The bremsstrahlung component, $\Gamma(z)$, is removed by fitting an exponential to the tail. This equation is of the same form as considered in the previous chapter. The depth-dose as a function of energy and depth forms a matrix.

In this problem and in others like it, a solution can not be determined by matrix inversion. The difficulty arises because dose contributions are always additive whereas a matrix inversion will generate positive and negative contributions.

The inversion is carried out by determining a best fit of the monoenergetic contributions to the measured data. A combination of simulated annealing and

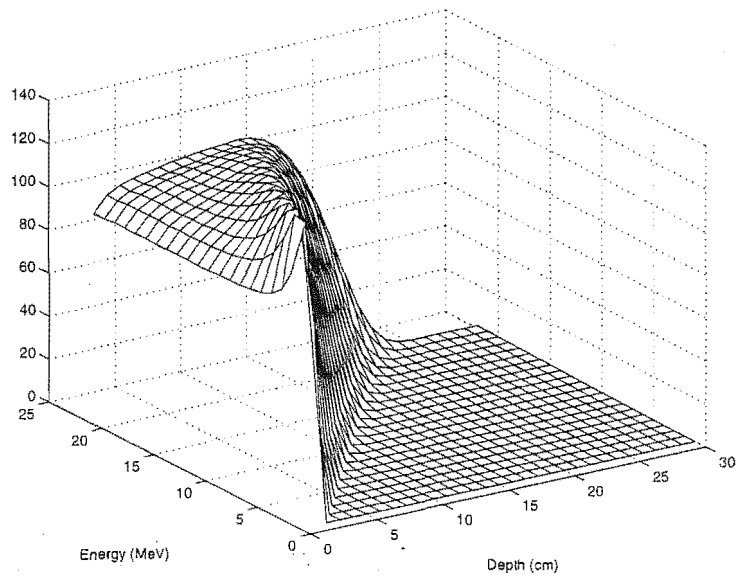

Figure 7.2: A set of depth-dose curves for 1 through 20 MeV monoenergetic beams calculated using Monte Carlo. 10000 histories gave a peak variance of 0.5%. A line source impinges on a semi-infinite water phantom and the dose is accumulated in a 10 cm radius cylinder of thickness 1 cm.

simplex minimisation techniques[260, 261] were used in this case to acquire a best-fit. Given the level of uncertainty in both the measurement and calculations (though technically we should eliminate uncertainties in the model being used) it is appropriate to accept a range of best-fits.

The spectrum determined using this technique is shown in figure 7.3. The broadening demonstrated in the main energy range of the beam and contributions at lower energies are features that cannot be ignored.

This result indicates the presence of several distinct lower energy contributions in the electron fluence. As these contributions are well defined it indicates that the beam exterior to the defined beam is being incompletely attenuated in the cone. This argument has been backed up by explicit modelling by Kassaee *et al*[208] comparing the old style of applicator upon which our measurements were performed and recent modifications to the Varian electron applicators.

7.3 Markov chain Monte Carlo

The second example we will consider is the resolution of two monoenergetic beam elements using a variation on inverse Monte Carlo, sometimes called the

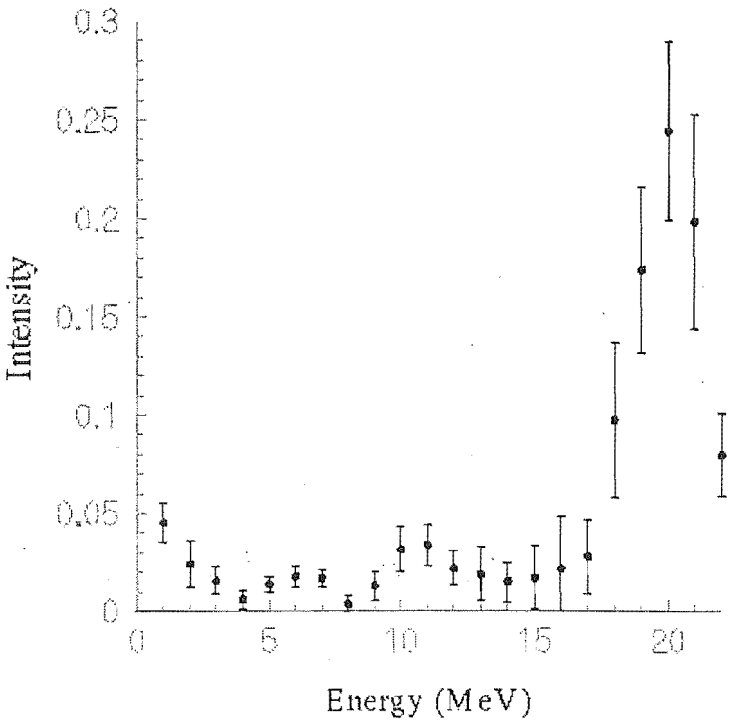

Figure 7.3: A spectrum determined for the 20 MeV electron modality on the Varian 2100C. An inverse-Monte Carlo method is used and described in the text. The energy ordinate can really only be regarded as an effective energy for obliquely incident contributions cannot be distinguished from low-energy contributions by this method.

method of Markov[47].

The distinction between this method and forward Monte Carlo is that a solution is iteratively obtained in the course of the sampling procedure. Much has been written in recent years about Markov chain methods[262, 263, 203]. The method is also useful in image processing[264] and is often used in solid state physics[265, 266], where a final state in a crystal lattice is achieved by consecutively smaller perturbations of the components. This procedure is, in fact, the basis of the Metropolis algorithm[48] and the simulated annealing method both of which are Markov chain methods.

We use a similar concept in that electron energies and trajectories are sampled from a range of sensible possibilites and dose distribution summed. A parameter is used to accept or reject contributions to the dose distribution on a basis of comparison with a measured set of data. The acceptance/rejection criterion is initially a relaxed condition but as the number of histories ap-

proaches that necessary to achieve a variance comparable to the measurement uncertainty the criterion is increasingly restrained.

Following the example of the Metropolis algorithm a Boltzmann type schedual, $e^{-\chi^2/kT}$, is used where the comparison between the measured and calculated sets is according to the statistical χ^2. Once the χ^2 parameter has fallen below the natural variance in the experimental data then acceptance/rejection criterion is maintained at that level and the particle fluence distribution is sampled until an adequate variance is obtained.

Before demonstrating this technique it is worth pointing out several advantages that this method has over the "non-iterative" inverse Monte Carlo method described above.

Firstly, as has already been argued in the introduction, the advantage of a Monte Carlo method is the avoidance of having to choose a grid. Although practically it is often necessary to form statistical groupings (bins) to obtain useful information, it is a fundamental distinction that the Monte Carlo method has to other forms of numerical quadrature. In this example we sample the electron energy from a continuous domain. It is even possible to determine χ^2 contributions with each discrete interaction and energy deposition.

Secondly, problems in higher dimensions are intractable using standard matrix manipulations. This we will see later in the chapter when the problem is defined in more general terms.

The Markov chain Monte Carlo has been implemented within the MAIN routine of the user-code MCMC1. To briefly illustrate how the method is implemented, the algorithm is described as follows.

The incident energy, ε, is sampled from a range of possible values The electron is transported and its energy deposition stored in a discrete array $D_\varepsilon(z_l) = D_{\varepsilon,l}$ and normalised to a total energy of 1. z_l is a point (a depth) in the dose scoring array. $l = 1, 2, ..., l_{\max}$. Where $l_{\max}$ is the size of the array. A parameter, t=min($\chi^2_{\min}$,$e^{-kn/N}$), is determined for the nth history of a total number of histories, N. A small perturbative element, ξ is sampled in the range $(1-\delta, 1+\delta)$. The χ^2 is determined as a sum over the dose scoring array comparing the accumulated dose $T(z_l) = T_l$ with an array of measurements $M(z_l) = M_l$ of size $l_{\max}$.

$$\chi^2 = \sum_{l=1}^{l_{\max}} (T_l(1 - t\xi) + D_{\varepsilon,l} t\xi - M_l)^2 / M_l^2 \tag{7.2}$$

If χ^2 is less than the parameter, t, or less than the previous successful value of χ^2 then $D_{\varepsilon,l}$ is added to T_l for all values of l in the same manner i.e.,

$$T_l = T_l(1 - t\xi) + D_{\varepsilon,l} t\xi \tag{7.3}$$

and the values of t and ε are outputed.

This is the entire procedure. Note that from a performance point of view the summations over the dose scoring array are costly and a χ^2 determined at each energy deposition (in, say, AUSGAB) would be preferable.

There are three parameters in this algorithm that need to be chosen, k, χ^2_{min} and δ. It is the need for special parameters in Markov chain algorithms that often generates criticism. The χ^2_{min} quantity establishes a lower bound to anticipated χ^2 values. When experimental uncertainty is to be considered then this will automatically set a minimim value to sensible close approximations. The random ξ element is not necessarily required but without it the algorithm struggles to find lower χ^2 values. We have used a value $\delta = 0.1$. The "cooling" parameter, k, should not cause too many problems but must be determined by trial. It is sensible to reduce the χ^2 as quickly as possible to χ^2_{min}. This process is called the "burn-in" period. Once a set of ε has been accumulated, placing the sampled set, T, within this range of uncertainty from the measured set, M, the algorithm will simply continue to generate hits and misses at a steady rate.

The rate of hits depends entirely on how fine a solution is able to be determined given the measurement set. If a result is highly peaked and the energy is being sampled over a much wider range then the hit rate will be low.

The results of running this algorithm for a beam consisting of a 9 MeV and 11 MeV electrons is presented. Figure 7.4 shows the spectrum calculated for a grid size of 20, 0.5 cm thick, slabs.

A second result (figure 7.5) is for a finer dose scoring array, 200 slabs of 0.05 cm thickness. Many more histories are required to obtain adequate statistics. There is no real demonstration of a resolution of the two energies in either example suggesting that a resolution of 2 MeV, at best, is possible using a broad beam source and depth-dose data. Interestingly the analysis is reminescent of spectroscopy

The "burn in" period and χ^2_{min} are demonstrated in figure 7.6 for the second, higher resolution dose grid calculation. The value of $k = 69$, $\chi^2_{\text{min}} = e^{-11.9}$.

7.4 A general stochastic method for the determination of phase space elements from in-phantom dose distributions

In this section we will present general formalism for determining phase-space elements of an electron therapy beam from a set of in-phantom measurements.

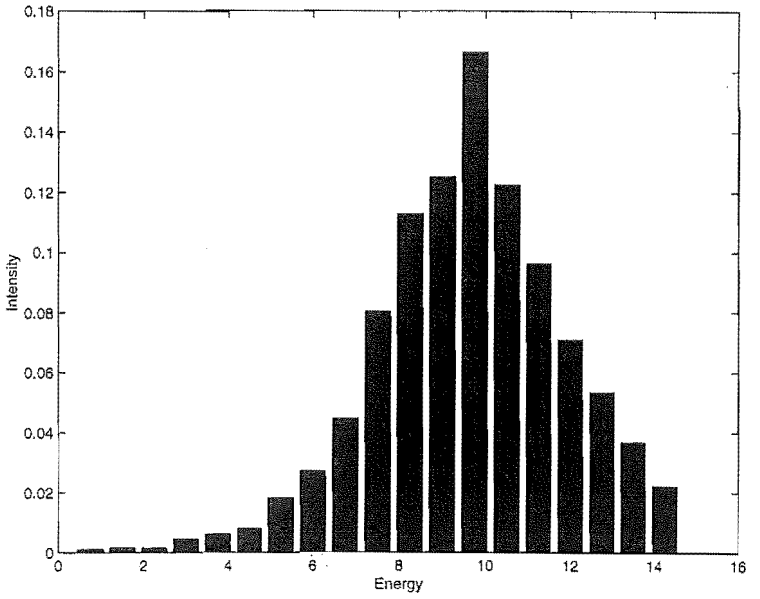

Figure 7.4: A spectrum determined using the Markov-chain Monte Carlo method from a dose-deposition of a theoretical beam with two monoenergetic broad-beam electron contributions at 9 and 11 MeV. The dose scoring array is formed from 20 slabs of 0.5 cm thickness.

This dose distribution in a semi-infinite homogeneous phantom is the integral of a set of kernels, $G(\mathbf{x})$, and need not be mono-energetic but of one angle of incidence. A set of kernels, $G_{\mathbf{p}}(\mathbf{x})$. are defined for the range of energy and trajectories in the problem. $\mathbf{p}$ is the energy-momentum 4-vector describing the energy and direction of the initial trajectory of a single electron. The contribution of each element of energy and momentum in the distribution is the phase-space distribution $P^{\{\mathbf{p}\}}$. The total dose is therefore,

$$D(\mathbf{x}) = \int_S \Phi(\mathbf{x}' \in S) G_{\{\mathbf{p}\}}(\mathbf{x}' - \mathbf{x}) P^{\{\mathbf{p}\}}(\mathbf{x}' \in S) dS \tag{7.4}$$

where a sum over the elements of P is implied. We would attempt to solve this equation for the distribution, $P^{\{\mathbf{p}\}}(\mathbf{x})$.

Monte Carlo can be used to generate kernels (consider figure 7.7 for example) over the range of $\mathbf{x}$, and $\mathbf{p}(\mathbf{x}')$. It is also feasible to measure the dose distribution of such a set of kernels. The kernels are weighted by best fit to the measured dose distribution giving spectral and angular distribution characteristics of the beam. A suitable means of fitting is a least-squares stochastic search. This method provides not only a fit but also a measure of the diver-

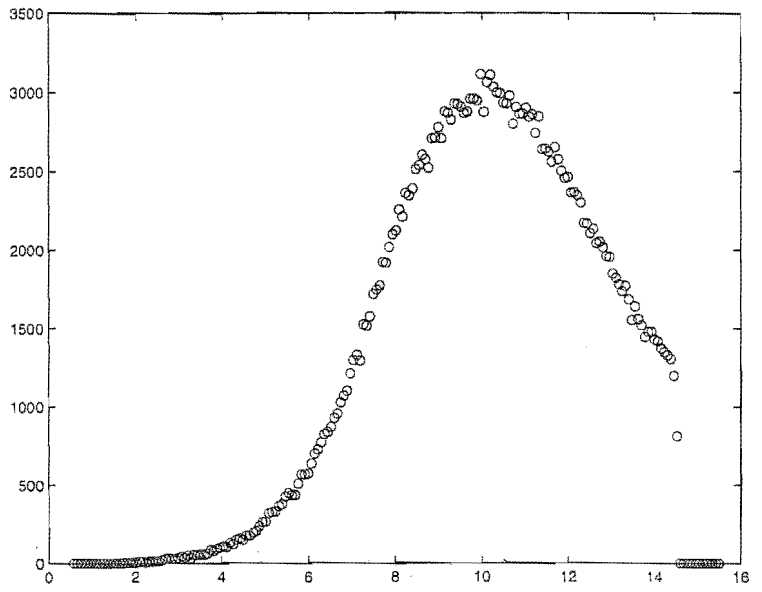

Figure 7.5: A spectrum determined using the Markov-chain Monte Carlo method from a dose-deposition of a theoretical beam with two monoenergetic broad-beam electron contributions at 9 and 11 MeV. The dose scoring array is formed from 200 slabs of 0.05 cm thickness.

gence and in this sense can also be described as a Monte Carlo method. It would be advantagous in terms of efficiency and implementation to combine these two procedures as in the Markov chain method of the second example given above.

The two special cases of the point source and of the broad beam give some insight into how this calculation is achieved and will be discussed, as will the manner in which we might treat the more general problem.

Under broad beam conditions, $\Phi(\mathbf{x})$ constant and $P^{\{\mathbf{p}\}}$ is independent of $\mathbf{x}$. A broad beam may contain an angular component. If we assume it is also parallel then $P^{\{\varepsilon\}}$ is the simply the spectrum.

$$D(\mathbf{z}) = \int D_{\{\varepsilon\}}(z) P^{\{\varepsilon\}} \mathrm{d}\varepsilon \tag{7.5}$$

$$\text{where } D_{\{\epsilon_i\}}(z) = \int_S \Phi G_{\{\epsilon_i\}}(\mathbf{x}' - \mathbf{x}) dS \tag{7.6}$$

which is, of course, equation 7.1.

A second example to consider is the pencil beam or aperture where $\Phi(\mathbf{x} \in$

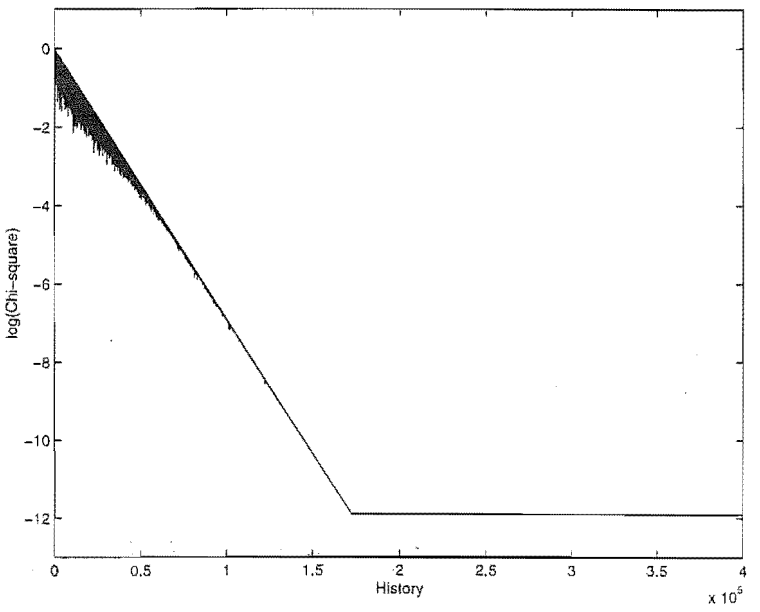

Figure 7.6: Schedual for log χ^2 values for a Markov chain Monte Carlo method to determine the spectra from a broad-beam dose distribution. $k = 69$. $\chi^2_{\min} = e^{-11.9}$ and $\delta = 0.1$. The "burn-in" period is 17% of the total histories.The hit-rate is approximately 30%.

$S) = \Phi_0 \delta(\mathbf{x} \in \mathbf{S})$. Therefore the incident electron is restricted to the origin and the momentum 4-vector $\mathbf{p} = \{\varepsilon, 0.0.1\}$. There is a radial distribution of dose. Hence,

$$D(\theta, z) = \Phi_0 G_{\{\varepsilon\}}(\theta, z) P^{\{\varepsilon\}}. \tag{7.7}$$

An aperture provides more information about the spectrum than a broad beam and can be obtained by measuring the radial dose distribution and performing an inversion using either of two methods presented. It appears that a method is required to determine the dose kernel and in the next section we look at two possible ways of acquiring this information.

If we write equation 7.7 in terms of a sum of elements, we see that the measurement itself is a matrix of values. The kernel must be represented by a thrid order tensor where each element in the incident spectrum gives a matrix. We would represent this problem in the following manner,

$$D^{z,\theta} = M^{z,\theta;\varepsilon} S_{\varepsilon}. \tag{7.8}$$

In the case of a generalised beam, the dose, $D^{x,y,z}$, is measured in three dimensions the incident beam is comprised of a spatial distribution of spectral

and angular components, $P_{x,y;\varepsilon,\theta,\phi}$, and the tensor kernel we would wish to invert, $M^{x,y,z}_{x',y';\varepsilon,\theta,\phi}$, has eight indices.

This problem seems intractable. However, the Markov chain method works well under these circumstances. An analogy is the efficiency of Monte Carlo methods in higher dimensional problems. If the dose distribution demonstrates consistancies then these will aid the generation of a solution. The time taken to perform the inversion relates not to the dimensionality of the problem but to the coherency.

7.5 Radiochromic film and Fricke dosimetry techniques

Radiochromic film can be sandwiched between sheets of PMMA. The radiation properties of PMMA and of the film[267, 268, 269, 43] closely approximate that of water. The simulated dose deposition can simply be calculated for the most desirable phantom materials.

An example of a beam slit cast into a PMMA phantom and measured with radiochromic film is presented (figure 7.8). Clearly a good deal of information can be obtained about the quality of the beam from such a measurement.

Recently attempts have been made to get this sort of information out of Fricke gel phantoms. The advantage of these techniques is the quantity of data (information) that can be obtained. By working with large depth-dose data sets we can get a good handle on the uncertainty and good statistics even for relatively noisy data aquisitions.

Fricke dosimetry is based on the radiosensitivity of ferrous ions. Ferrous ions are oxidised to ferric ions and the change in the solvation of these ions can be read out using MRI. The advantage of a Fricke technique over all other methods is the ability to determine a full three-dimensional data-set. Fricke is also relatively water equivalent[270, 271]

Other methods of data aquisition will be useful including diode and Markus chamber measurements in a water tank. In either case it is important to have good appreciation of the energy response and directional response. Simple models of detectors can be drawn up and examined using Monte Carlo. The detector response can be "hard-wired" into the inverse problem in a manner such as demonstrated in the previous chapter.

7.6 Conclusion

The measurements on the Varian 2100c and the mathematical models presented verify the success of this method applied to electron dosimetry. We are able to determine reasonably accurate spectra from the analysis of depth dose. It appears that more accurate spectra will be obtained by performing the same analysis on pencil beam or line source distributions.

With a combination of these types of measurement it may be possible to infer radial distribution. It may for example be possible to derive angular data given the depth dose for series of increasing field sizes. These investigations have begun and a set of depth-dose measurements have been determined over a range of field sizes using an NACP chamber mounted in a RFA-300 water tank.

The inverse calculation does not appear to be easily optimised. It is clear from the brief analysis given in this chapter that the method deserves further attention, though fundemental results such as those demonstrating resolution of the data aquisition methods will be of interest and should be publishable in the near future.

A final point about the use of such techniques. Clearly there are circumstances where it is desireable to use forward Monte Carlo calculations to determine incident beam parameters. The brachytherapy problem provides a good example as the source spectrum is well defined. Some work has been done in simulating the effects of the applicator cones. In this case the physicist is able to obtain geometric information about the cones easily. Forward Monte Carlo[208, 272] and scatter methods[273, 274] have been used with success. The methods described in this chapter are a practical way to get information about the source energy which are required by these sorts of calculations. This is a more sensible solution to the problem of determining incident source spectra than either full-detail Monte Carlo simulations of the internal workings of an accelerator or a complete inverse method. The inverse methods presented in this and the previous chapter are an efficient means of putting the experimental measurement back into Monte Carlo dosimetry.

Potentially the method described in this chapter could be used as a measurement based planning algorithm. The method offers a means to extrapolate from measured sets of data to *in vivo* dose distributions. Potential sources of variability in dose such as tissue inhomogeneity, irregular field shapes and surface angulation can be applied as perturbations to the measured data. If these perturbations are small with respect to the total dose then an algorithm should demonstrate high levels of efficiency. With a conventional, determi-

nistic, algorithm there seems no obvious way to detect such short cuts and vast integrations will have to be performed in circumstances that may even be identical to the original measured data. A Monte Carlo based perturbation method will fair better in these circumstances as the algorithm will stop when an adequate variance is achieved.

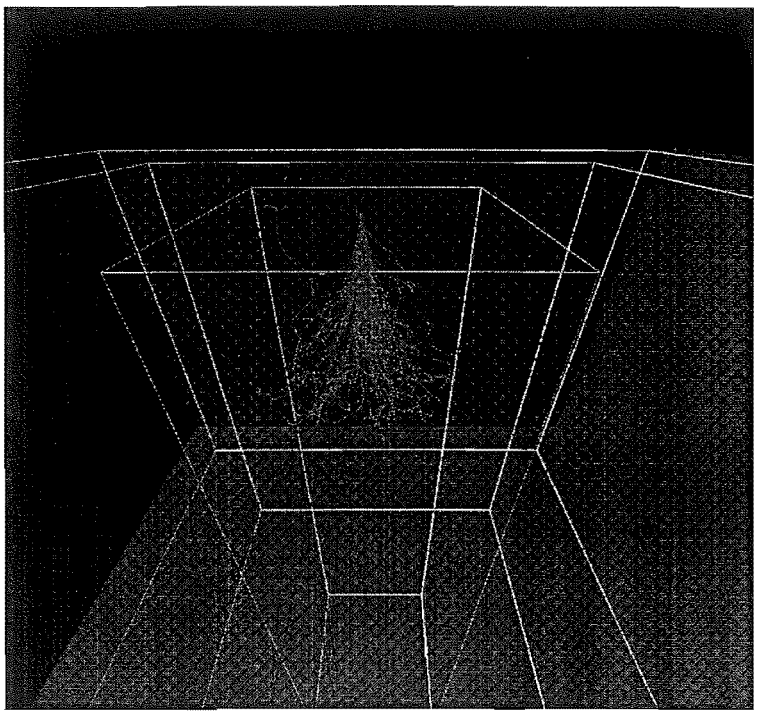

Figure 7.7: The phase-space output from an EGS4 simulation of a 9 MeV electron pencil beam in a water phantom. While statistically poor it is visually rich. Generated from the transport of position vector, x, and outputed at each call to AUSGAB. It is displayed using the EGS4Windows3.0 interface.

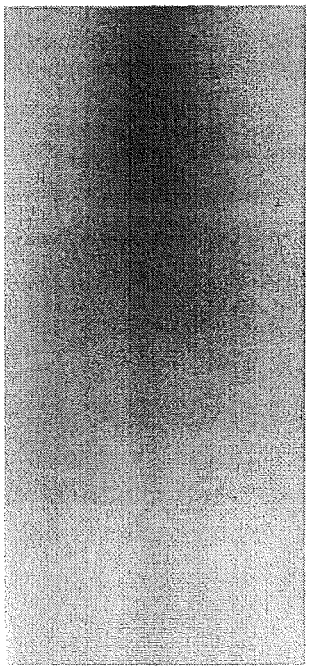

Figure 7.8: A line electron source generated with the Varian 2100C 20 MeV electron modality with one set of collimator jaws set to 0.5 cm width and no applicator cone. Radiochromic film is used to image the dose distribution. The digitometry has been performed using a document scanner.

Chapter 8

Conclusion

Physicists have an active role in the radiation oncology treatment planning process, as it is their responsibility to determine the "dose". Many commercial planning systems are now available for determining dose distributions in a human anatomy, over a wide of range of modalities and radiation energies. Historically, planning has been based on experimental measurements of the dose distribution in a water or water equivalent phantom. The ion-chamber, cross-calibrated with a primary standard chamber, is the conventional means by which the dose has been determined[217].

In chapter two we have examined a total skin electron therapy (TSET) for the treatment of mycosis fungoides. The dosimetry requirements are met with the use of a parallel plate chamber in a Solid Water phantom. We are able to demonstrate the tissue equivalence of Solid Water in the energy range by comparison with measurements in a water tank. Film and thermoluminescent dosimeters, embedded in PMMA, are used to simulate the cylindrical cross section of the patient. An anthropomorphic phantom enables the verification of these measurements in a more anatomically correct situation.

A novel method of total body irradiation has been investigated in chapter three using dynamic control of the beam delivery. A large uniform distribution is generated which is necessary in the preparation of a patient for bone marrow transplant. The dose rate is varied to compensate for variation in the source to patient distance as the beam gantry rotates across the patient. Dose profiles and depth distributions have been determined with ion-chamber measurements in Solid Water. Methods of determining the optimum beam control are examined for a range of patient scenarios and a method of conformal therapy is proposed.

In recent years technology gains, particularly in the computer industry, have meant more physically precise algorithms such as the Monte Carlo method are tending to be employed and certainly much research has been invested into algorithms that will challenge the current level of technology. The rest of the thesis has examined the use of the Monte Carlo method.

Calculations are presented in chapter four to aid in the determination of

radiation shielding and bunker design. A code has been written that enables the point-by-point entry of an enclosure design and can determine the radiation fluence at the exit on a basis of the source intensity and energy. The code can be interfaced with a computer aided design package and can output a graphical representation of a small number of histories superimposed on the enclosure plan for verification.

The *in vivo* x-ray fluorescence technique is a promising diagnostic and therapy aid. The method can be used to measure industrial heavy metal uptake and to image chelated chemotherapy cytotoxins such as cisplatin. In chapter five we examine the use of polarised photons to improve sensitivity. Monte Carlo methods are used to examine Compton scatter with linear polarisation and to determine optimum source voltages for the production of fluorescence in phantom.

Monte Carlo based treatment planning is much sought after and already there are a number of currently available planning systems boasting Monte Carlo generated kernels. Monte Carlo has been used to determine backscatter factors[149, 150, 151, 152, 153], brachytherapy dose distributions[159, 160, 161, 162, 163, 164, 165, 166, 167, 168] and electron stopping powers[275, 276] for purposes of treatment planning. An example of this type of calculation is demonstrated in chapter six for superficial therapy planning. We also demonstrate how source information can be obtained from measurements with a high-purity germanium detector.

Monte Carlo is now being applied more rigorously to therapy planning particularly in electron therapy planning and several important optimisations are now able to be used in the clinical setting[277, 278]. Such methods require the determination of incident beam spectra, angular distribution and spatial profiles, collectively known as phase-space information. This problem has been discussed at length in the course of this thesis and we have examined several measurement techniques for determining this information.

Full detail Monte Carlo simulation of the treatment head [205] has provided much information about the spectral and angular content of electron beams. Simulation of the treatment head is a technique that will become increasingly popular, particularly if general purpose code such as BEAM [206] are widely available.

Manufacturers may issue head designs to workers to enable such calculations. However, there is no guarantee that component positions and dimensions are not significantly different from factory settings particularly when post-installation tweaking is performed to bring monitor units (MU) into line with the cGy and to correct for asymmetries in the profile.

This lesson has been learned recently with the discovery that the two versions of the Varian 2100c electron applicator cones produce rather different combinations of central-axis dose contributions[208]. The finding confirms a similar result from our own examinations of electron therapy beams, in chapter seven, using the inverse Monte Carlo method.

The inverse Monte Carlo method and Markov-chain Monte Carlo provide a potential solution. Certainly some experimental information is necessary for the treatment planning algorithm to accurately reflect the state of the radiation unit. Dose distributions determined using a stripped back head with a small aperture gives much information about the quality of the beam. It is then entirely appropriate to simulate the details of scatter in the electron applicators and cut-outs.

In this year of the centenary of the discovery of the electron by J.J. Thomson at Cambridge University, electron therapy is an increasingly used modality and an increasingly well understood dosimetry. As a good contender for Monte Carlo based treatment planning, this area is worthy of our efforts.

Chapter 9

Acknowledgements

This thesis is the result of a collaboration with the Department of Medical Physics and Bioengineering at Christchurch Hospital. Dr Richard Tremewan is thanked for his early guidance and good advice.

The bulk the programme has involved the Christchurch Oncology Service, their equipment and resources and I especially thank Dr Chris Atkinson for his support and interest in my work.

The research has been funded by the Canterbury-West Coast of the Cancer Society and I am grateful for the support of Mrs Pamela Williams and its members.

Finally I thank my supervisors, Dr Phil Butler and Mr John Turner, for their support and efforts on my behalf.

References

[1] W R Nelson, H Hirayama, and D W O Rogers. *The EGS4 code system, rep. SLAC-265.* Stanford Linear Accelerator Center, California, 1985.

[2] D I Thwaites, D T Burns, S C Klvenhagen, A E Nahum, and W G Pitchford. The ipemb code of practice for electron dosimetry for radiotherapy beams of initial energy from 2 to 50 MeV based on an air kerma calibration. *Phys. Med. Biol.*, 41:2557–2603, 1996.

[3] M Pla, G C Stafford, and E B Podgorsak. Total body irradiation with a sweeping beam. *Int. J. Radiation Oncology Biol. Phys.*, 9:83–89, 1983.

[4] Clarkson. A note on the depth doses in fields of irregular shape. *Br. J. Radiol.*, 14:265, 1941.

[5] T G H Rogers and T M Peters. Christchurch hospital interactive radiation treatment planning system. Technical report, Christchurch Public Hospital, Christchurch, New Zealand, 1976.

[6] D I Armstrong. Computer programs for treatment planning and treatment dose prescription. Technical report, Christchurch Public Hospital, Christchurch, New Zealand, 1980.

[7] J Milan and R E Bentley. The storage and manipulation of radiation dose data on a small digital computer. *Br. J. Radiol.*, 47:115, 1974.

[8] R H T Bates and T M Peters. Towards improvements in tomography. *New Zealand J. Science*, 14:883–896, 1971.

[9] P R Smith, T M Peters, and R H T Bates. Image reconstruction from finite numbers of projections. *J. Phys. A: Math. Nucl. Gen.*, 6:361–382, 1973.

[10] R N Tremewan, T M Peters, P Bones, and J J Tait. A low resolution CT scanner in radiotherapy. *Australasian Physical and Engineering Sciences in Medicine*, 10(4):196–200, 1987.

[11] R N Tremewan, T M Peters, P Bones, and J J Tait. Computed tomography in radiotherapy treatment planning. *Australasian Radiology*, 32(1):50–56, 1988.

[12] R N Tremewan, B R Mentink, and D A Pinchin. Integration of CT images into radiotherapy treatment planning using a Commodore Amiga personal computer. *Medical and Biological Engineering and Computing*, 27(3):325–327, 1989.

[13] J R Cunningham. Scatter-air ratios. *Phys. Med. Biol.*, 17:42–51, 1972.

[14] H E Johns and J R Cunningham. *The Physics of Radiology.* Thomas, Illinois, 4th edition, 1983.

[15] D J Perry and J G Holt. A model for calculating the effects of small inhomogeneities on electron beam dose distributions. *Med. Phys.*, 7:207–215, 1980.

[16] K R Hogstrom, M D Mills, and P R Almond. Electron beam dose calculations. *Phys. Med. Biol.*, 26(3):445–459, 1981.

[17] A Brahme, I Lax, and P Andreo. Electron beam dose planning using discrete Gaussian beams: mathematical background. *Acta Radiologica Oncology*, 20:147–158, 1981.

[18] B L Werner, F M Khan, and F C Deibel. A model for calculating electron beam scattering in treatment planning. *Med. Phys.*, 9(2):180–187, 1982.

[19] Bruinvis I A D, Van Amstel A, Elevelt A J, and Van der Laarse R. Calculation of electron beam dose distributions for arbitrarily shaped fields. *Phys. Med. Biol.*, 28(6):667–683, 1983.

[20] D C Murray, P W Hoban, W Round, I D Graham, and O Y de Vel. Radiotherapy treatment planning using transputers. *New Zealand Journal of Computing*, 1(2):30–38, 1989.

[21] I D Graham, D C Murray, P W Hoban, and W H Round. Transputer radiotherapy computations. In *4th Proceedings Australian Transputer and OCCAM Group*, Canberra, 1991.

[22] D C Murray, P W Hoban, W Round, and I D Graham. Superposition on a multicomputer system. *Med. Phys.*, 18(3):468–473, 1991.

[23] A F Bielajew and D W O Rogers. A standard timing benchmark for EGS4 Monte Carlo calculations. *Med. Phys.*, 19:303–304, 1992.

[24] M Caon, G Bibbo, and J Pattison. Running the EGS4 Monte Carlo code with Fortran 90 on a Pentium computer. *Australasian Physical and Engineering Sciences in Medicine*, 19(3):201–203, 1996.

[25] J R Turner, R P Hugtenburg, and C J Wynne. Total skin electron therapy at two energies on a linear accelerator. *Australasian Physical and Engineering Sciences in Medicine*, 18(4):208–220, 1995.

[26] R P Hugtenburg, J R Turner, S P Baggerley, D A Pinchin, N A Oien, C H Atkinson, and R N Tremewan. Total-body irradiation on an isocentric linear accelerator: A radiation output compensation technique. In *Annual Conference, New Zealand branch, Australasian College of Physical Scientists and Engineers in Medicine*, Auckland, 1993.

[27] R P Hugtenburg, J R Turner, S P Baggerley, D A Pinchin, N A Oien, C H Atkinson, and R N Tremewan. Total-body irradiation on an isocentric linear accelerator: A radiation output compensation technique. In *Engineering and the Physical Sciences in Medicine*, Perth, Australia, 1994. Australasian College of Physical Scientists and Engineers in Medicine.

[28] R P Hugtenburg, J R Turner, S P Baggerley, D A Pinchin, N A Oien, C H Atkinson, and R N Tremewan. Total-body irradiation on an isocentric linear accelerator: A radiation output compensation technique. In *45th Annual Scientific Meeting, Royal Australasian College of Radiologists*, Christchurch, New Zealand, 1994.

[29] R P Hugtenburg, J R Turner, S P Baggerley, D A Pinchin, N A Oien, C H Atkinson, and R N Tremewan. Total-body irradiation on an isocentric linear accelerator: A radiation output compensation technique. *Phys. Med. Biol.*, 39(5):783–793, 1994.

[30] P A Love. *In vivo* sarcomere length measurement and total body irradiation. Master's thesis, University of Canterbury, 1996.

[31] R P Hugtenburg, J R Turner, and P H Butler. A Monte Carlo approach to accelerator maze design. In *Annual Conference, New Zealand branch, Australasian College of Physical Scientists and Engineers in Medicine*, Wellington, 1994.

[32] A J Faid and R P Hugtenburg. Bunker design of a 10 MV linear accelerator using Monte Carlo. Technical report, Christchurch Hospital, 1996.

[33] J R Turner, D M Mannering, R P Hugtenburg, and B A Robinson. Measurement of platinum in patients receiving chemotherapy: work in progress to date. In *Annual conference New Zealand branch*. Wellington, 1994. Australasian College of Physical Scientists and Engineers in Medicine.

[34] D M Mannering. X-ray fluorescence. Masters thesis, University of Otago, 1996.

[35] R P Hugtenburg, J R Turner, D M Mannering, and B A Robinson. Monte Carlo methods for the *in vivo* analysis of cisplatin using X-ray fluorescence. In *4th International Symposium on In Vivo Body Composition Studies*, Malmo, Sweden, 1996.

[36] R P Hugtenburg, J R Turner, D M Mannering, and B A Robinson. Monte Carlo methods for the *in vivo* analysis of cisplatin using X-ray fluorescence. *Int. J. Appl. Radiat. Isotopes.*, 49:673–676, 1997.

[37] A F Bielajew. Monte Carlo modelling with external electron-beam radiotherapy - why leave it to chance? In *Proc. Int. Conf. Comp. Radiat. Ther. XI*, pages 2–5, Manchester, 1994.

[38] J Williams. Megavoltage bremsstrahlung spectra from therapeutic linear accelerators. Undergraduate project report, University of Canterbury, 1994.

[39] A P H Butler and J R Turner. Measurement of superficial X-ray spectra using a high purity germanium detector. Technical report, Christchurch Hospital, 1995.

[40] R P Hugtenburg, J R Turner, P H Butler, A P H Butler, and M A Stevens. Monte Carlo based radiotherapy planning. In *Engineering and the Physical Sciences in Medicine*, page 81, Queenstown, New Zealand, 1995. Australasian College of Physical Scientists and Engineers in Medicine.

[41] M A Stevens. Fricke dosimetry in gels. Undergraduate project report, University of Canterbury, 1995.

[42] M A Stevens. High resolution dosimetry for oncology. Fricke dosimetry in gels. Master's thesis, University of Canterbury, 1996.

[43] M A Stevens, J R Turner, R P Hugtenburg, and P H Butler. High resolution dosimetry using radiochromic film and a document scanner. *Phys. Med. Biol.*, 41:2357–2365, 1996.

[44] S P Baggerley, D M Mannering, R P Hugtenburg, and J R Turner. Field size dependence of effective source distance and field factors of a 9 MeV electron beam. *Australian Physical and Engineering Sciences in Medicine*, 17(2):84–87, 1994.

[45] R P Hugtenburg. Spectral reconstruction of electron therapy beams for use in Monte Carlo simulation. In *Engineering and the Physical Sciences in Medicine*, page 105, Perth, 1994. Australian College of Physical Scientists in Medicine.

[46] R P Hugtenburg, J R Turner, and P H Butler. Numerical reconstruction of electron therapy beams. In *Röntgen Centenary Congress*, Birmingham, UK, 1995. British Institute of Radiology. Work in progress.

[47] S Chandrasekhar. Stochastic problems in physics and astronomy. *Revs. Mod. Phys.*, 15(1):1–89, 1943.

[48] N Metropolis, A W Rosenbluth, M N Rosenbluth, A H Teller, and E Teller. Equation of state calculations by fast computing machines. *J. Chem. Phys.*, 21(6):1087–1092, 1953.

[49] C J Karzmark. Advances in linear accelerator design for radiotherapy. *Med. Phys.*, 11(2):105–128, 1984.

[50] G W Sherouse, J L Naves, M A Varia, and J Rosenman. A spreadsheet program for brachytherapy planning. *Int. J. Radiation Oncology Biol. Phys.*, 13:639–646, 1987.

[51] G W Sherouse and E L Chaney. The portable virtual simulator. *Int. J. Radiation Oncology Biol. Phys.*, 21:475–482, 1991.

[52] ICRU. *Report 35. Radiation dosimetry: Electron beams with energies between 1 and 50 MeV.* International Commission on Radiation Units and Measurement, 1984.

[53] H H Rossi and W C Roesch. Field equations in dosimetry. *Radiat. Res.*, 16:783, 1962.

[54] E C Vonderheid and B Micaily. Cutaneous t-cell lymphoma. In C A Perez, L W Brady, and J B Lippincolt, editors, *In principles and Practices of Radiation Oncology*, pages 395–405. Philadelphia, 1987.

[55] J R Turner, C Wynne, and F Woodham. *Total skin electron therapy procedure manual.* Internal report: Christchurch Hospital Oncology Service, 1992.

[56] C J Karzmark, R Loevinger, R E Steele, and M Weissbluth. A technique for large field superficial electron therapy. *Radiology*, 74:633–644, 1960.

[57] R T Hoppe, R S Cox, Z Fuks, N M Price, M A Bagshaw, and E M Farber. Electron-beam therapy for mycosis fungoides: The Stanford University experience. *Cancer Treatment Reports*, 63:691–700, 1979.

[58] R S Cox, R J Heck, P Fessenden, C J Karzmark, and D C Rust. Development of total skin electron therapy at two energies. *Int. J. Radiation Oncology Biol. Phys.*, 18:659–669, 1989.

[59] I J Das, K P McGee, and C-W Cheng. Electron-beam characteristics at extended treatment distances. *Med. Phys.*, 22(10):1667–1674, 1995.

[60] J G Holt and D J Perry. Some physical considerations in whole skin electron beam therapy. *Med. Phys.*, 9(5):769–776, 1982.

[61] P J Tetenes and P N Goodwin. Comparative study of superficial whole-body radiotherapeutic techniques using a 4-MeV nonangulated electron beam. *Radiology*, 122:219–226, 1977.

[62] T G H Rogers, D I Armstrong, and H W J Fox. A twelve field method for whole-skin electron therapy. *NZ Medical Physics and Biomedical Engineering*, 7(2), 1980.

[63] L D Mattsson, K A Johansson, and H Svensson. Calibration and use of plane-parallel ionization chambers for the determination of absorbed dose in electron beams. *Acta Radiologica Oncology*, 20(6):385–399, 1981.

[64] A E Nahum and D I Thwaites. Use of plane parallel plate chambers for dosimetry of electron beams in radiotherapy. In *Working material: Review of data and methods recommended in the international code of practice*, number 277, pages 47–65. IAEA, 1993.

[65] F M Khan, K P Doppke, K R Hogstrom, G J Kutcher, R Nath, S C Prasad, J A Purdy, and M Rozenfeld. Clinical electron-beam dosimetry: Report of AAPM radiation therapy committee task group no. 25. *Med. Phys.*, 18(1):73–109, 1991.

[66] D I Thwaites. Charge storage effect on dose in insulating phantoms irradiated with electrons. *Phys. Med. Biol.*, 29(9):1153–1156, 1984.

[67] E El-Khatib, J Antolak, and J Scrimger. Evaluation of film and thermoluminescent dosimetry of high-energy electron beams in heterogeneous phantoms. *Med. Phys.*, 19(2):317–323, 1992.

[68] F T Serota, E D Burkey, C S August, and G J D'Angio. Total body irradiation as preparation for bone marrow transplantation in treatment of acute leukemia and aplastic anemia. *Int. J. Radiation Oncology Biol. Phys.*, 9:1941–1949, 1983.

[69] D A Fraass. The development of conformal radiation therapy. *Med. Phys.*, 22(11):1911, 1995.

[70] U Quast. Physical treatment planning of total-body irradiation: Patient translation and beam-zone technique. *Med. Phys.*, 12(5):567–574, 1985.

[71] L H Gerig, J Szanto, T Binchay, and P Genest. A translating-bed technique for total-body irradiation. *Phys. Med. Biol.*, 39:19–35, 1994.

[72] P Metcalfe, T P Y Wong, and P W Hoban. Radiotherapy X-ray beam inhomogeneity corrections: The problem of lateral electronic disequilibrium. *Australasian Physical and Engineering Sciences in Medicine*, 16(4):155–167, 1993.

[73] T Knöös, A Ahnesjö, P Nilsson, and L Weber. Limitations of a pencil beam approach to photon dose calculations in lung tissue. *Phys. Med. Biol.*, 40:1411–1420, 1995.

[74] W Jackson. Surface effects of high-energy X-rays at oblique incidence. *Br. J. Radiol.*, 44:109–115, 1971.

[75] B J Gerbi, A S Meigooni, and F M Khan. Dose buildup for obliquely incident photon beams. *Med. Phys.*, 14(3):393–399, 1987.

[76] S Dupont, J C Rosenwald, and H Beauvais. Convolution calculations of dose in the buildup regions for high energy photon beams obliquely incident. *Med. Phys.*, 21(9):1391–1400, 1994.

[77] M J Butson, M D Perez, J N Mathur, and P E Metcalfe. 6 MV X-ray dose in the build-up region: Empirical model and incident angle effect. *Australasian Physical and Engineering Sciences in Medicine*, 19(3):74–82, 1996.

[78] R P Hugtenburg. Training programme for the dynamic beam delivery toolbox. Varian Inc., Palo Alto., Technical report, Christchurch Hospital, November 1996.

[79] D E Raeside. Monte Carlo principles and applications. *Phys. Med. Biol.*, 21:181–197, 1976.

[80] T M Jenkins, W R Nelson, and A Rindi, editors. *Monte Carlo transport of electrons and photons*. Plenum Press, 1988.

[81] F James. Monte Carlo theory and practice. *Rep. Prog. Phys.*, 43:1145–1189, 1980.

[82] P Andreo. Monte Carlo techniques in medical radiation physics. *Phys. Med. Biol.*, 36(7):861-920, 1991.

[83] D C Murray. Technical report: Using EGS4 Monte Carlo in medical radiation physics. *Australasian Physical and Engineering Sciences in Medicine*, 13(3):132-147, 1990.

[84] V G Smyth, A C McEwan, A F Bielajew, and D W O Rogers. Interface artifacts in Monte Carlo calculations. *Phys. Med. Biol.*, 31(3):299–300, 1986.

[85] P Andreo, J Medlin, and A F Bielajew. Constraints on the multiple scattering theory of Molière in Monte Carlo simulations of the transport of charged particles. *Med. Phys.*, 20:1315–1325, 1993.

[86] B A Faddegon and D W O Rogers. Comparisons of thick-target bremsstrahlung calculations for EGS4/PRESTA and ITS version 2.1. *Nucl. Inst. Meth. A*, 327:556–565, 1993.

[87] D W O Rogers. How accurately can EGS4/PRESTA calculate ion-chamber response? *Med. Phys.*, 20(2):319–323, 1993.

[88] A F Bielajew and D W O Rogers. Effects of the Möller cross section error in the EGS4 code. *Med. Phys.*, 23:1153, 1996. (abstract).

[89] A F Bielajew and D W O Rogers. PRESTA: The parameter reduced electron-step transport algorithm for electron Monte Carlo transport. *Nucl. Instrum. Meth. B*, 18:165–181, 1987.

[90] A F Bielajew, R Mohan, and C S Chui. Improved bremsstrahlung photon angular sampling in the EGS4 code system. *Med. Phys.*, 17:552, 1990.

[91] A Del Guerra, W R Nelson, and P Russo. A simple method to introduce K-edge sampling for compounds in the code EGS4 for x-ray element analysis. *Nucl. Instrum. Meth. A*, 306:378–385, 1991.

[92] C M Ma and A E Nahum. A new algorithm for EGS4 low-energy electron transport to account for the change in discrete interaction cross-section with energy. *Nucl. Inst. Meth. B*. 72:319–330, 1992.

[93] Y Namito, S Ban, and H Hirayama. Implementation of linearly-polarized photon scattering into the EGS4 code. *Nucl. Instrum. Meth. A*, 332:277–283, 1993.

[94] Y Namito, S Ban, and H Hirayama. Implementation of the Doppler broadening of a Compton-scattered photon in the EGS4 code. *Nucl. Instrum. Meth. A*, 349:489–494, 1994.

[95] Y Namito, S Ban, H Hirayama, N Nariyama, H Nakishima, Y Nakane, Y Sakamoto, N Sasamoto, Y Asano, and S Tanaka. Compton scattering of 20- to 40-keV photons. *Phys. Rev. A*. 51(4):3036–3043, 1995.

[96] P C Lauterbur. Image formation by induced local interactions: Examples employing nuclear magnetic resonance. *Nature*. 242:190–191, 1973.

[97] D R White. An analysis of the Z-dependence of photon and electron interactions. *Phys. Med. Biol.*, 22(2):219–228, 1977.

[98] N C Yang and P K Leichner. Effective atomic numbers for low-energy total photon interactions in human tissues. *Med. Phys.*, 14(5):759–766, 1987.

[99] D R Chettle. Photoelectron bremsstrahlung - analytical possiblities. *Phys. Med. Biol.*, 35:259–264, 1990.

[100] G Harding and D Chettle. Comments on the article "photoelectron bremsstrahlung - analytical possibilities. *Phys. Med. Biol*, 40:471–476, 1995.

[101] J A Cook. *Mortran3 User's Guide.* Stanford Linear Accelerator Center, Stanford, California, 1982.

[102] Y Namito, S Ban, and H Hirayama. *LSCAT: Low-energy photon-scattering expansion for the EGS4 code.* KEK, National Laboratory for High Energy Physics, Japan, 1995.

[103] D E Knuth. The art of computer programming. In *Seminumerical algorithms*, volume 2, pages 1–170. Addison-Wesley, Reading, MA. 2nd edition, 1969.

[104] F James. A review of pseudorandom number generators. *Comput. Phys. Commun.*, 60:329–344, 1990.

[105] N A Frigerio and N Clark. A random number set for Monte Carlo computations. *Trans. Am. Nucl. Soc.*, 22:283–284, 1975.

[106] G Marsaglia. Random numbers fall mainly in the planes. *Proc. Nat. Acad. Sci.*, 61:25–28, 1968.

[107] M Luscher. A portable high-quality random number generator for lattice field theory simulations. *Comp. Phys. Comm.*, 79:100–110, 1994.

[108] M J Berger. Monte Carlo calculation of the penetration and diffusion of fast charged particles. In B Alder, S Fernbach, and M Rotenberg, editors, *Methods in Computational Physics*, volume 1, pages 135–215. Academic Press, 1963.

[109] Y C Lo. Albedos for 4-, 10-, and 18-MV bremsstrahlung X-ray beams on concrete, iron, and lead - normally incident. *Med. Phys.*, 19(3):659–666, 1992.

[110] P H McGinley, M S Miner, and M L Mitchum. A method for calculating the dose due to capture gamma rays in accelerator mazes. *Phys. Med. Biol.*, 40:1467–1473, 1995.

[111] P J Biggs. Calculation of shielding door thicknesses for radiation therapy facilities using the its Monte Carlo program. *Health Physics*. 61(4):465–472, 1991.

[112] J A Halbleib, T A Mehlhorn, and R P Kensek. *ITS version 2.1, the integrated TIGER series of coupled electron/photon transport codes.* Radiation Shielding Information Centre, Oak Ridge National Laboratory: CCC-467. Oak Ridge TN, 1987.

[113] B L Berman. Photoneutron cross sections. *Atomic Data and Nucleur Data Tables*, 15(4):319–390, 1975.

[114] P D Allen and M A Chaudhri. The dose contribution due to photonuclear reactions during radiotherapy. *Med. Phys.*, 9(6):904–906, 1982.

[115] H Ing, W R Nelson, and R A Shore. Unwanted photon and neutron radiation resulting from collimated photon beams interacting with the body of radiotherapy patients. *Med. Phys.*, 9(1):27–33, 1982.

[116] H Ing and R A Shore. Unwanted radiation produced by leakage neutrons from medical electron accelerators. *Med. Phys.*, 9(1):34–36, 1982.

[117] J R Plata, K R Hogstrom, and C Tannanonta. Neutron leakage measurements from a medical linear accelerator. *Med. Phys.*, 11(4):498–501, 1984.

[118] Y Uwamino, T Nakamura, and T Ohkubo. Measurement and calculation of neutron leakage from a medical electron accelerator. *Med. Phys.*, 13(3):374–384, 1986.

[119] B Forkman and R Peterson. *Handbook on nuclear activation data*. IAEA, 1987.

[120] P D Allen and M A Chaudhri. Neutron yields from selected materials irradiated with high energy photons. *Phys. Med. Biol.*, 36(12):1653–1663, 1991.

[121] I M Borchardt, J R Patterson, A H Beddoe, and G C Sorell. An investigation of photonuclear reactions in cerrobend eutectic material with an 18 MV linac. *Phys. Med. Biol.*, 36(5):649–653, 1991.

[122] P H McGinley. Photoneutron fields in medical accelerator rooms with primary barriers constructed of concrete and metal. *Health Physics*, 63(6):698–702, 1992.

[123] P H McGinley. Photonneutron production in the primary barriers of medical accelerator rooms. *Health Physics*, 62(4):359–362, 1992.

[124] R P Hugtenburg and J R Turner. Investigation of photoactivation in the therapeutic linear accelerator. In *Annual Conference, New Zealand branch, Australasian College of Physical Scientists and Engineers in Medicine*, Dunedin, 1991.

[125] R Metzger, R Richardson, and K A van Riper. A Monte Carlo model for retrospective analysis of shield design in a diagnostic X-ray room. *Health Physics*, 65(2):164–171, 1993.

[126] J F Briesmeister. *MCNP - a general Monte Carlo N-particle transport code, version 4A*. Los Alamos National Laboratory, report LA-12625 edition, 1993.

[127] J F Tinney. *In Vivo* X-ray fluorescence analysis - concepts and equipment. In Hoffer, Beck, and Gottschalk, editors, *The role of semiconductor detectors in the future of nuclear medicine*, pages 214–229. Soc. Nuclear Med., 1971.

[128] W D Morgan, A M El-Sharkawi, M B M Jaib, C J Evans, S Cobbold, A Sivyer, B N C Littlepage, and J Dutton. X-ray fluorescence technique for *in vivo* analysis of "natural" and administered trace elements. In K J Ellis, S Yasumura, and W D Morgan, editors, *In-vivo body composition Studies*, chapter 52, pages 318–324. IPSM, London, 1987.

[129] R Jonson, S Mattson, and B Unsgaard. A method for *in vivo* analysis of platinum after chemotherapy with cisplatin. *Phys. Med. Biol.*, 33(7):847–857, 1988.

[130] L Wielopolski, J F Rosen, D N Slatkin, R Zhang, J A Kalef-Ezra, J C Rothman, M Maryanski, and S T Jenks. *In vivo* measurement of cortical bone lead using polarised X-rays. *Med. Phys.*, 16(4):521–528, 1989.

[131] A C Todd, D R Chettle, M C Scott, and L J Somervaille. Monte Carlo modelling of *in vivo* X-ray fluorescence of lead in the kidneys. *Phys. Med. Biol.*, 36(4):439–448, 1991.

[132] J D Wallace. The Monte Carlo modelling of in-vivo X-ray fluorescence measurements in lead in tissue. *Phys. Med. Biol.*, 39:1745–1756, 1994.

[133] J Börjesson, L Barregœrd, G Sällsten. A Schüz, R Jonson, and M Alpsten. *In vivo* XRF analysis of mercury: the relation between concentrations in the kidney and the urine. *Phys. Med. Biol.*, 40:413–426, 1995.

[134] J Christoffersson and S Mattson. Polarised X-rays in XRF-analysis for improved *in vivo* detectability of cadmium in man. *Phys. Med. Biol.*, 28(10):1135–1144, 1983.

[135] R W Ryon. The use of polarised X-rays for improved detection limits in energy dispersive X-ray spectrometry. *Adv. X-ray analysis*, 28:63–73, 1985.

[136] R B Strittmatter. X-ray fluorescence of intermediate- to high-atomic-number elements using polarised X-rays. *Adv. X-ray analysis*, 28:75–79, 1985.

[137] D G Lewis. Optimization of a polarized source for *in vivo* X-ray fluorescence analysis of platinum and other heavy metals. *Phys. Med. Biol.*, 39:197–206, 1994.

[138] D G Lewis, A Kilic, and C A Ogg. Adaptation of the EGS4 Monte Carlo code for the design of a polarized source for X-ray fluorescence analysis of platinum and other heavy metals *in vivo*. *Adv. X-Ray Analysis*, 38:579–585, 1995.

[139] C D Zerby. A monte Carlo calculation of the response of gamma-ray scintillation counters. In B Alder, S Fernbach, and M Rotenberg, editors. *Methods in Computational Physics*, volume 1, pages 89–134. Academic Press, 1963.

[140] L H J Peaple and A K Burt. The measurement of spectra from X-ray machines. *Phys. Med. Biol.*, 14(1):73–85, 1969.

[141] W W Seelentag and W Panzer. Lightly filtered X-ray bremsstrahlung spectra generated at 200 to 300 kV. *Radiat. Res.*, 80:409–422, 1979.

[142] W W Seelentag and W Panzer. Stripping of X-ray bremsstrahlung spectra up to 300 kV_p on a desk type computer. *Phys. Med. Biol.*, 24(4):767–780, 1979.

[143] C S Chen, K Doi, C Vyborny, H-P Chan, and G Holje. Monte Carlo simulation studies of detectors used in the measurement of diagnostic X-ray spectra. *Med. Phys.*, 7(6):627–635, 1980.

[144] J Laban. Correcting measured X-ray spectra for the effects of pulse pile-up and the detector response function. Technical Report 8, National Radiation Laboratory, Christchurch, New Zealand, 1996.

[145] W L Dunn. Inverse Monte Carlo analysis. *J, Comp. Phys.*, 41:154–166, 1981.

[146] W L Dunn, V C Boffi, and F O'Foghludha. Applications of the inverse Monte Carlo method in photon beam physics. *Nucl. Instrum. Meth. A*, 255:147–151, 1987.

[147] R M Harrison. Backscatter factors for diagnostic radiology (1–4 mm Al HVL). *Phys. Med. Biol.*, 27(12):1465–1474, 1982.

[148] S C Klevenhagen. Experimentally determined backscatter factors for X-rays generated at voltages between 16 and 140 kV. *Phys. Med. Biol.*, 34(12):1871–1882, 1989.

[149] H-P Chan and K Doi. Monte Carlo simulation studies of backscatter factors in mammography. *Radiology*, 139:195–199, 1981.

[150] B Grosswendt. Backscatter factors for X-rays generated at voltages between 10 and 100 kV. *Phys. Med. Biol.*, 29(5):579–591, 1984.

[151] B Grosswendt. Dependence of the photon backscatter factor for water on source-to-phantom distance and irradiation field size. *Phys. Med. Biol.*, 35:1233–1245, 1990.

[152] B Grosswendt. Dependence of the photon backscatter factor for water on irradiation field size and source-to-phantom distances between 1.5 and 10 cm. *Phys. Med. Biol.*, 38(305–310), 1993.

[153] H J Patrocinio, J-P Bissonnette, Marc R Bussière, and L J Schreiner. Limiting values of backscatter factors for low-energy X-ray beams. *Phys. Med. Biol.*, 41:239–253, 1996.

[154] L Stanton, S D Brattelli, J L Day, R E Stanton, and T Villafana. Measurements of diagnostic X-ray backscatter by a novel ion chamber method. *Med. Phys.*, 9(1):121–130, 1982.

[155] S C Klevenhagen, R J Aukett, J E Burns, R M Harrison, R T Knight, A E Nahum, and K E Rosser. Report of the IPSM working party on low- and medium-energy X-ray dosimetry. *Phys. Med. Biol.*, 36(8):1027–1038, 1991.

[156] S C Klevenhagen, R J Aukett, J E Burns, R M Harrison, R T Knight, A E Nahum, and K E Rosser. Memorandum from the IPSM: Back-scatter and F-factors for low- and medium-energy X-ray beams in radiotherapy. *Br. J. Radiol.*, 64:836–841, 1991.

[157] S C Klevenhagen, D D'Souza, and I Bonnefoux. Complications in low energy X-ray dosimetry caused by electron contamination. *Phys. Med. Biol.*, 36(8):1111–1116, 1991.

[158] R M Harrison. Central-axis depth dose data for diagnostic radiology. *Phys. Med. Biol.*, 26:671–691, 1981.

[159] R G Dale. A Monte Carlo derivation of parameters for use in the tissue dosimetry of medium and low energy nuclides. *Brit. J. Radiol.*, 55:748–757, 1982.

[160] R G Dale. Some theoretical derivations relating to the tissue dosimetry for brachytherapy nuclides, with particular reference to ^{125}I. *Med. Phys.*, 10(2):176–183, 1983.

[161] G S Burns and D E Raeside. Monte Carlo simulation of the dose distribution around ^{125}I seeds. *Med. Phys.*, 13:420–424, 1987.

[162] G Herbold, G Hartmann, H Treuer, and W J Lorenz. Monte Carlo calculation of energy build-up factors in the range from 15 keV to 100 keV, with special reference to the dosimetry of ^{125}I seeds. *Phys. Med. Biol.*, 33(9):1037–1053, 1988.

[163] J F Williamson. Monte Carlo evaluation of specific dose constants in water for ^{125}I seeds. *Med. Phys.*, 15(5):686–694, 1988.

[164] J F Williamson and F J Quintero. Theoretical evaluation of dose distributions in water about models 6711 and 6702 ^{125}I seeds. *Med. Phys.*, 15(6):891–897, 1988.

[165] G Luxton. Comparison of radiation dosimetry in water and in solid phantom materials for I-125 and Pd-103 brachytherapy sources: EGS4 Monte Carlo study. *Med. Phys.*, 21(5):631–641, 1994.

[166] E E Furhang, G Sgouros, and C-S Chui. Radionuclide photon dose kernels for internal emitter dosimetry. *Med. Phys.*, 23(5):759–764, 1996.

[167] R Wang and R S Sloboda. EGS4 dosimetry calculations for cylindrically symmetric brachytherapy sources. *Med. Phys.*, 23(8):1459–1465, 1996.

[168] K Weaver, C Hartmann Siantar, W Chandler, and R M White. A source model for efficient brachytherapy computations with Monte Carlo. *Med. Phys.*, 23(12):2079–2084, 1996.

[169] C C Ling, E D Yorke, I J Spiro, D Kubiatowicz, and D Bennet. Physical dosimetry of ^{125}I seeds of a new design for interstitial implant. *Int. J. Radiation Oncology Biol. Phys.*, 9:1747–1752, 1983.

[170] G Luxton, M A Astrahan, P E Liggett, D L Neblett, D M Cohen, and Z Petrovich. Dosimetric calculations and measurements of gold plaque ophthalmic applicators using iridium-192 and iodine-125 seeds. *Int. J. Radiation Oncology Biol. Phys.*, 15:167–176, 1988.

[171] M A Astrahan, G Luxton, G Jozsef, T D Kampp, P E Liggett, M D Sapozink, and Z Petrovich. An interactive treatment planning system for ophthalmic plaque radiotherapy. *Int. J. Radiation Oncology Biol. Phys.*, 18(3):679–687, March 1990.

[172] M A Astrahan, G Luxton, G Jozsef, P E Ligget, and Z Petrovich. Optimization of ^{125}I ophthalmic plaque brachytherapy. *Med. Phys.*, 17(6):1053–1057, 1990.

[173] J F Williamson and R Nath. Clinical implementation of AAPM Task Group 32 recommendations on brachytherapy source strength specifications. *Med. Phys.*, 18(3):439–448, 1991.

[174] A S Meigooni and R Nath. A comparison of radial dose functions for ^{103}Pd, ^{125}I, ^{125}I, ^{145}Sm, ^{241}Am, ^{169}Yb, ^{192}Ir and ^{137}Cs brachytherapy sources. *Int. J. Radiation Oncology Biol. Phys.*, 22:1125–1130, 1992.

[175] L Sakelliou, K Sakellariou, K Sarigiannis, A Angelopoulos, A Perris, and G Zarris. Dose rate distributions around ^{60}Co, ^{137}Cs, ^{198}Au, ^{192}Ir, ^{241}Am, ^{125}I (models 6702 and 6711) brachytherapy sources and the nuclide ^{99}Tc^{m}. *Phys. Med. Biol.*, 37(10):1859–1872, 1992.

[176] J A Dreesen, D I Dumitru, T C Fearon, and D C Kushner. Photon absorbed fractions for cylindrical geometry: Homogeneous nonradioactive cylinder containing a homogeneous cylindrical distribution of activity. *Med. Phys.*, 23(8):1447–1457, 1996.

[177] G Luxton and M A Astrahan. Output factor constituents of a high-energy photon beam. *Med. Phys.*, 15(1):88–91, 1988.

[178] G Luxton, M A Astrahan, and Z Petrovich. Backscatter measurements from a single seed of ^{125}I for ophthalmic plaque dosimetry. *Med. Phys.*, 15(3):397–400, 1988.

[179] S T Chiu-Tsao, L L Anderson, K O'Brien, L Stabile, and J C Liu. Dosimetry for ^{125}I seed (model 6711) in eye plaques. *Med. Phys.*, 21(5):651–657, 1994.

[180] A de la Zerda, S Chiu-Tung, J Lin, L L Boulay, I Kanna, J H Kim, and H S Tsao. ^{125}I eye plaque dose distribution including penumbra characteristics. *Med. Phys.*, 23(3):407–418, March 1996.

[181] P J Muench, A S Meigooni, R Nath, and W L McLaughlin. Photon energy dependence of the sensitivity of radiochromic film and comparison with silver halide film and LiF TLDs used for brachytherapy dosimetry. *Med. Phys.*, 18(4):769–775, 1991.

[182] S T Chiu-Tsao, A de la Zerda, J Lin, and J H Kim. High-sensitivity GafChromic film dosimetry for ^{125}I seed. *Med. Phys.*, 21(5):651–657, 1994.

[183] T Kron and J M Pope. Dose distribution measurement in superficial x-ray beams using NMR dosimetry. *Phys. Med. Biol.*, 39:1337–1349, 1994.

[184] I J Das and K L Chopra. Backscatter dose perturbation in kilovoltage photon beams at high atomic number interfaces. *Med. Phys.*, 22(6):767–773, 1995.

[185] I J Das, G E Desobry, and C J Soares. Back-scatter dose perturbation with a small high-Z inhomogeneity in kilovoltage beams (abstract). *Med. Phys.*, 22(6):965, 1995.

[186] A S Meigooni and R Nath. Tissue inhomogeneity correction for brachytherapy sources in a heterogeneous phantom with cylindrical symmetry. *Med. Phys.*, 19(2):401–407, 1992.

[187] Z Li, J F Williamson, and H Perera. Monte Carlo calculation of kerma to a point in the vicinity of media interfaces. *Phys. Med. Biol.*, 38:1825–1840, 1993.

[188] J F Williamson, H Perera, and Z Li. Comparison of calculated and measured heterogeneity correction factors for ^{125}I, ^{137}Cs and ^{192}Ir brachytherapy sources near localized heterogeneities. *Med. Phys.*, 20(1):209–222, 1993.

[189] S C Klevenhagen. *Physics of electron beam therapy.* Number 13 in Medical physics handbooks. Adam Hilger Ltd, Bristol, England, 1985.

[190] Rustgi S N and Rodgers J E. Analysis of the bremsstrahlung component 6-18 MeV electron beams. *Med. Phys.*, 14(5):884–888, 1987.

[191] B B Socini, S Hyödynmaa, and A Brahme. The role of phantom and treatment head generated bremsstrahlung in high-energy electron beam dosimetry. *Phys. Med. Biol.*, 41:2657–2677, 1996.

[192] H A Bethe, M E Rose, and L P Smith. The multiple scattering of electrons. *Proc. Am. Phil. Soc.*, 78(4):573–585, 1938.

[193] B Rossi. *High energy particles.* Prentice-Hall, Englewood cliffs, New Jersey, 1952.

[194] H A Bethe. Molière's theory of multiple scattering. *Phys. Rev*, 89(6):1256–1266, 1953.

[195] R M Sternheimer. Multiple scattering correction for counter experiments. *Rev. Sci. Instrum.*, 25(11):1070–1075, 1954.

[196] W T Chu, A Ludewigt, and T R Renner. Instrumentation for treatment of cancer using proton and light-ion beams. *Rev. Sci. Instrum.*, 64(8):2055–2122, 1993.

[197] U Schneider and E Pedroni. Proton radiography as a tool for quality control in proton therapy. *Med. Phys.*, 22(4):353–363, 1995.

[198] K R Russell, E Grusell, and A Montelius. Dose calculations in proton beams: range straggling corrections and energy scaling. *Phys. Med. Biol.*, 40:1031–1043, 1995.

[199] N Blais and E B Podgorsak. The mass scattering power method for determining the kinetic energy of clinical electron beams. *Phys. Med. Biol.*, 37(10):1931–1942, 1992.

[200] B B Sorcini, P Andreo, A F Bielajew, S Hvödynmaa, and A Brahme. An improved energy-range relationship for high-energy electron beams based on multiple accurate experimental and Monte Carlo data sets. *Phys. Med. Biol.*, 40:1135–1159, 1995.

[201] X A Li and D W O Rogers. Electron mass scattering powers: Monte Carlo and analytical calculations. *Med. Phys.*, 22(5):531–541, 1995.

[202] R D Evans. *The atomic nucleus.* McGraw-Hill, New York, 1955.

[203] J Besag, P Green, D Higdon, and Kerrie Mengersen. Bayesian computation and stochastic systems. *Statistical Science*, 10(1):3–66, 1995.

[204] M Udale. A Monte Carlo investigation of surface doses for broad electron beams. *Phys. Med. Biol.*, 33(8):939–953, 1988.

[205] M Udale-Smith. Monte Carlo calculations of electron beam parameters for three Philips linear accelerators. *Phys. Med. Biol.*, 37(1):85–105, 1992.

[206] D W O Rogers, B A Faddegon, G X Ding, C M Ma, J Wei, and T R Mackie. Beam: A Monte Carlo code to simulate radiotherapy treatment units. *Med. Phys.*, 22(5):503–524, 1995.

[207] M A Ebert, P W Hoban, and P J Keall. Modelling clinical accelerator beams: A review. *Australasian Physical and Engineering Sciences in Medicine*, 19(3):131–150, 1996.

[208] A Kassaee, M D Altschuler, S Ayyalsomayajula, and P Bloch. Influence of cone design on the electron beam characteristics on clinical accelerators. *Med. Phys.*, 21(11):1671–1676, 1994.

[209] W L McLaughlin. Dosimetry: new approaches. *Radiat. Phys. Chem.*, 41(1-2):45–56, 1993.

[210] M Farahani, F C Eichmiller, and W L McLaughlin. Measurement of absorbed doses near metal and dental material interfaces irradiated by X- and gamma-ray therapy beams. *Phys. Med. Biol.*, 35(3):369–385, 1990.

[211] T D Solberg, K S Iwamoto, and A Norman. Calculation of radiation dose enhancement factors for dose enhancement therapy of brain tumours. *Phys. Med. Biol.*, 37(2):439–443, 1992.

[212] S Uehara, H Nikjoo, and D T Goodhead. Cross-sections for water vapour for the Monte Carlo electron track structure code from 10 eV to the MeV region. *Phys. Med. Biol.*, 37:1841–1858, 1992.

[213] A V Lappa, E A Bigildeev, D S Burmistrov, and O N Vasilyev. "trion" code for radiation action calculations and its application in microdosimetry and radiobiology. *Radiat. Environ. Biophys.*, 32:1–19, 1993.

[214] American Association of Physicists in Medicine. *Total Skin Electron Therapy: Technique and Dosemetry. Report of Task Group 30 Radiation Therapy Committee. Report no. 23.* Am. Inst. of Phys., 1988.

[215] P R Almond. Total-skin/electron irradiation technique and dosimetry. In J G Kereiakes, H R Elson, and C G Born, editors, *Radiation Oncology Physics. Medical Physics Monograph no. 15*, pages 296–332. American Association of Physicist in Medicine, 1986.

[216] C Constantinou, F H Attix, and B R Palliwal. A solid water phantom material for radiotherapy X-ray and X-ray beam calibrations. *Med. Phys.*, 9(436–441), 1982.

[217] Absorbed dose determination in photon and electron beams: An adaptation of the IAEA international code of practice. National Radiation Laboratory, Christchurch, New Zealand, May 1989.

[218] F W Wittkamper, H Thierens, A van der Plaetsen, C de Wagter, and B Mijnheer. Perturbation correction factors for some ionization chambers commonly applied to electron beams. *Phys. Med. Biol.*, 36:1639–1652, 1991.

[219] B E Bjängard, G T Y Chen, R W Piontek, and G K Svensson. Analysis of dose distributions in whole body superficial electron therapy. *Int. J. Radiation Oncology Biol. Phys.*, 2(3,4):319–324, 1977.

[220] S C Klevenhagen. An algorithm to include the bremsstrahlung contamination in the determination of the absorbed dose in electron beams. *Phys. Med. Biol.*, 39:1103–1112, 1994.

[221] P M Ostwald and T Kron. Surface does measurements for highly oblique electron beams. *Med. Phys.*, 23(8):1413–1420, 1996.

[222] J Van Dyk, J M Galvin, G P Glasgow, and E B Podgorsak. *The physical aspects of total and half body photon irradiation. Report by Task Group 29 of the Radiation Therapy Committee of the American Association of physicists in medicine*, volume AAPM report no. 17. American Institute of Physics, 1986.

[223] J R Cunningham and D J Wright. A simple facility for whole-body irradiation. *Radiology*, 78:941–949, 1986.

[224] E Browne, R N Tremewan, and C I Watson. Total body irradiation using a temporarily modified theratron 780 co-60 unit. *Australasian Physical and Engineering Sciences in Medicine*, 11(4):162–168, 1988.

[225] J M Jensen, F Brix, and P Kohr. General and specific aspects of experimental dose measurement in total body irradiation (TBI). *Strahlentherapie und Onkologie*, 178:250–253, 1986.

[226] British Institute of Radiology. Central axis depth dose data for use in radiotherapy - suppl. 17, 1983.

[227] E B Podgorsak, C Pla, M Pla, P Y Lefebvre, and R Heese. Physical aspects of a rotational total skin electron irradiation. *Med. Phys.*, 10(2):159–168, 1983.

[228] J Van Dyk. Dosimetry for total body irradiation. *Radiation and Oncology*, 9:107–118, 1987.

[229] R Mohan, C Chui, and L Lidofsky. Energy and angular distribution of photons from medical linear accelerators. *Med. Phys.*, 12(5):592–597, 1985.

[230] J E Fernández, J H Hubbel, and A L Hanson. Polarization effects on multiple scattering gamma transport. *Radiat. Phys. Chem.*, 41:579–630, 1993.

[231] R Birch and M Marshall. Computation of bremsstrahlung X-ray spectra and comparison with spectra measured with a ge(li) detector. *Phys. Med. Biol*, 24(3):505–517, 1979.

[232] A E Nahum. Perturbation effects in dosimetry: Part I. Kilovoltage X-rays and electrons. *Phys. Med. Biol.*, 41:1531–1580, 1996.

[233] S C Klevenhagen, R J Aukett, R M Harrison, C Moretti, A E Nahum, and K E Rosser. The IPEMB code of practice for the determination of the absorbed dose for X-rays below 300kv generating potential (0.035 mm al- 4 mm Cu HVL; 10-300kV generating potential. *Phys. Med. Biol.*, 41:2605–2625, 1996.

[234] R Loevinger and S S Yaniv. Absorbed dose determination for X-rays in the Grenz-ray region (5 to 20 keV quantum energy). *Phys. Med. Biol.*, 10(2):213–227, 1965.

[235] L Silberstein. Determination of the spectral composition of X-ray radiation from filtration data. *J. Opt. Soc. Am.*, 22:265–280, 1932.

[236] L Silberstein. Spectral composition of an X-ray radiation determined from its filtration curve. *Philos. Mag.*, 15:375–394, 1933.

[237] J D Henderson and A H Beddoe. Measurement of X-ray spectra. *NZ Phys. Bio. Eng.*, 7(1):5–12, Mar 1980.

[238] B R Archer and L K Wagner. A Laplace transform pair model for spectral reconstruction. *Med. Phys.*, 9(6):844–847, 1982.

[239] P H Huang, T S Chen, and K R Kase. Reconstruction of diagnostic X-ray spectra by numerical analysis of transmission data. *Med. Phys.*, 13(5):707–710, 1986.

[240] J M Boone. X-ray spectral reconstruction from attenuation data using neural networks. *Med. Phys.*, 17(4):647–654, 1990.

[241] E R Epp and H Weiss. Spectral fluence of scattered radiation in a water medium irradiated with diagnostic X-rays. *Radiat. Res.*, 30:129–139, 1967.

[242] J M Boone. The three parameter equivalent spectra as an index of beam quality. *Med. Phys.*, 15:304–310, 1988.

[243] D M Tucker, G T Barnes, and D P Chakraborty. Semiempirical model for generating tungsten target X-ray spectra. *Med. Phys.*, 18(2):211–218, 1991.

[244] J-P Bissonnette and L J Screiner. A comparison of semiempirical models for generating tungsten target X-ray spectra. *Med. Phys.*, 19(3):579–582, 1992.

[245] E Storm and H I Israel. Photon cross sections from 1 keV to 100 MeV for elements Z=1 to Z=100. *Nucl. Data Tables A*, 7:565–681, 1970.

[246] J M Boone and A E Chavez. Comparison of X-ray cross sections for diagnostic and therapeutic medical physics. *Med. Phys.*, 23(12):1997–2005, 1996.

[247] C-M Ma and A E Nahum. Calculation of absorbed dose ratios using correlated Monte Carlo sampling. *Med. Phys.*, 20(4):1189–1199, 1993.

[248] Johnsen S W, LaRiviere P D, and Tanabe E. Electron depth-dose dependence on energy spectral quality. *Phys. Med. Biol.*, 28(12):1401–1407, 1983.

[249] J O Deasy, P R Almond, and M T McEllistrem. The spectral dependence of electron central-axis depth-dose curves. *Med. Phys.*, 21(9):1369–1376, 1994.

[250] J O Deasy, P R Almond, M T McEllistrem, and C K Ross. A simple magnetic spectrometer for radiotherapy electron beams. *Med. Phys.*, 21(11):1703–1714, 1994.

[251] J O Deasy, P R Almond, and M T McEllistrem. Measured electron energy and angular distributions from clinical accelerators. *Med. Phys.*, 23(5):675–684, 1996.

[252] C E Floyd. Inverse Monte Carlo: A unified reconstruction algorithm for SPECT. *IEEE Trans. Nucl. Sci*, NS-32(1):779–785, 1985.

[253] C E Floyd, FR J Jaszczak, S H Mangloos, K L Greer, and R E Coleman. Improved SPECT reconstruction using inverse Monte Carlo. *SPIE (Physics and Engineering of Computerized Multidimensional Imaging and Processing)*, 671:206–213, 1986.

[254] C E Floyd, FR J Jaszczak, K L Greer, and R E Coleman. Inverse Monte Carlo as a unified reconstruction algorithm for ECT. *J. Nucl. Med.*, 27:1577–1585, 1986.

[255] K F Koral, X Wang, K R Zasadny, N H Clinthorne, W L Rogers, C E Floyd Jr, and R J Jaszczak. Testing of local gamma-ray scatter fractions determined by spectral fitting. *Phys. Med. Biol.*, 36(2):177–190, 1991.

[256] B K Lind and A Brahme. Optimisation of radiation therapy dose distributions using scanned electron and photon beams and multileaf collimators. In *The use of computers in radiation therapy*, pages 235–239. Elsevier, Amsterdam, 1987.

[257] M D Altschuler, P Bloch, E L Buhle, and S Ayyalasomayajula. 3D dose calculations for electron and photon beams. *Phys. Med. Biol.*, 37(2):391–411, 1992.

[258] R Martinelli, G Ghiso, P Boccacci, F Foppiano, and L Andreucci. Determination of the energy of the electrons incident upon a water phantom to build composite energy beam kernels for 3D dose calculation. In *Proc. Int. Conf. Comp. Radiat. Ther. XI.* pages 124–125, Manchester, 1994.

[259] R P Hugtenburg, J R Turner, and P H Butler. Numerical reconstruction of electron therapy beams. *Med. Phys.*, 22(6):948, 1995.

[260] W H Press. *Numerical recipes: the art of scientific computing.* Cambridge University Press, New York, 1986.

[261] A G Ferreira and J Žerovnk. Bounding the probablity of success of stochastic methods for global optimization. *Computers Math. Applic.*, 25:1–8, 1993.

[262] A Frigessi, P di Stefano, C-R Hwang, and S-J Sheu. Convergence rates of the gibbs sampler, the metropolis algorithm and other single-site updating dynamics. *J. R. Statist. Soc. B*, 55(1):205–219, 1993.

[263] G O Roberts and N G Polson. On the geometrical convergence of the Gibbs sampler. *J. R. Statist. Soc. B*, 56(2):377–384, 1994.

[264] J Besag. On the statistical analysis of dirty pictures. *J. R. Statist. Soc.*, 48(3):259–302, 1986.

[265] V Gerold and J Keen. The determination of atomic interaction energies in solid solutions from short range order coefficients - an inverse Monte Carlo method. *Acta Metall.*, 35(2):393–399, 87.

[266] D A Keen and R L McGreevy. Structural modelling of glasses using reverse Monte Carlo simulation. *Nature*, 344:423–425, 1990.

[267] W L McLaughlin and L Chalkley. Low atomic numbered dye systems for ionizing radiation measurements. *Photo. Sci. Eng.*, 9:159–165, 1965.

[268] J A Sayeg and R C Gregory. A new method for characterizing beta-ray ophthalmic applicator sources. *Med. Phys.*, 18(3):453–461, 1991.

[269] A S Meigooni, M F Sanders, and G S Ibbott. Dosimetric characteristics of an improved radiochromic film. *Med. Phys.*, 23(11):1883–1888, 1996.

[270] M F Chan and K Ayyangar. Verification of water equivalence of FeMRI gels using Monte Carlo simulation. *Med. Phys.*, 22(4):475–478, 1995.

[271] T Kron, P Metcalfe, and J M Pope. Investigation of the tissue equivalence of gels used for NMR dosimetry. *Phys. Med. Biol.*, 38:139–150, 1993.

[272] M A Ebert and P W Hoban. A Monte Carlo investigation of electron beam applicator scatter. *Med. Phys.*, 22:1431–1435, 1995.

[273] M A Ebert and P W Hoban. A model for electron beam applicator scatter. *Med. Phys.*, 22:1419–1429, 1995.

[274] M A Ebert and P W Hoban. The energy and angular characteristics of the applicator scattered component of an electron beam. *Australasian Physical and Engineering Sciences in Medicine*, 19(3):151–159, 1996.

[275] C Malamut, D W O Rogers, and A F Bielajew. Calculation of water/air stopping-power ratios using EGS4 with explicit treatment of electron-positron differences. *Med. Phys.*, 18(6):1222–1228, 1991.

[276] G X Ding, D W O Rogers, and T R Mackie. Calculation of stopping-power ratios using realistic clinical electron beams. *Med. Phys.*, 22:489–501, 1995.

[277] H Neuenschwander and E R Born. A macro Monte Carlo method for electron beam dose calculations. *Phys. Med. Biol.*, 37:107–125, 1992.

[278] P J Keall and P W Hoban. Super-Monte Carlo: A 3-D electron beam dose calculation algorithm. *Med. Phys.*, 23(12):2023–2034, 1996.

[279] S J Thomas. Virtual source distances for electron beams between 5 and 20 MeV. *Phys. Med. Biol.*, 33(11):1325–1328, 1988.

[280] B J McParland. A parameterization of the electron beam output factors of a 25 MeV linear accelerator. *Med. Phys.*, 14(4):665–669, 1987.

[281] B J McParland. An analysis of equivalent fields for electron beam central-axis dose calculations. *Med. Phys.*, 19(4):901–906, 1992.

[282] M D Mills, K R Hogstrom, and P R Almond. Prediction of electron beam output factors. *Med. Phys.*, 9(1):60–68, 1982.

Published paper. Physics in Medicine and Biology, September 1996

Appendix A

High resolution dosimetry using radiochromic film and a document scanner

[Film dosimetry using a document scanner]
M A Stevens†, J R Turner‡, R P Hugtenburg† and P H Butler†
† Department of Physics and Astronomy, University of Canterbury, Christchurch, New Zealand.
‡ Department of Medical Physics and Bio-Engineering, Christchurch Hospital, Christchurch, New Zealand.

A method of reading exposed radiochromic film is described which has significant advantages over conventional densitometry. The method employs a document scanner and associated software for imaging the film. The resulting images are easily analysed using standard software to yield high resolution dose maps. A calibration was performed which relates scanner signal to dose, allowing for the determination of dose at any point on an exposed film. Results obtained using a broadband densitometer are compared to those where the scanner has been used. The technique was used to measure the dose distribution around a COMS–type ophthalmic applicator.

A.1 Introduction

Conventional silver halide film has a highly non-linear photon energy response, especially at low energies. It has radiation interaction properties markedly different to those of tissue. Along with variations introduced by the necessary post-irradiation processing, this type of film is extremely difficult to use for accurate analytical dosimetry.

The concept of radiochromic film was first proposed by McLaughlin and Chalkley (1965). In the last few years, technological advances in the manufacturing process have increased its sensitivity to the point where it can now be used for high resolution quantitative dose mapping of clinical radiation sources. Radiochromic film has significant advantages over silver halide film: it has a relatively flat energy response (Muench *et al* 1991), it is self–developing so eliminates variations introduced by the processing step, it is insensitive to visible

light allowing for ease of handling, and the film is fabricated from low atomic number materials (Sayeg and Gregory 1991) so does not perturb the radiation beam to the same degree as silver halide film. The response of the film has been shown to be independent of dose rate (Saylor *et al* 1988). The uniformity of the film (Chu *et al* 1990) means that no background measurements need to be taken prior to irradiation.

Conventionally, the optical density of exposed silver halide film is measured by absorption densitometry. A spot of light is applied to the film and the amount of light transmitted is recorded. The very dark colouration of exposed silver halide film makes this technique suitable for its analysis.

Un-exposed radiochromic film is transparent with a light blue hue, while film which has been exposed to ionizing radiation is dark blue. The blue colouration means that the broad-band light source of a conventional densitometer is only attenuated in the red part of the spectrum. This leads to an overall reduction in the light intensity which is quite small and so the resulting measurements have a low signal to noise ratio. Densitometers employing a He-Ne laser, which emits light at 633 nm, close to the peak at about 660 nm in the absorption spectrum of the film, have been used by several workers (Muench *et al* 1991. Chiu-Tsao *et al* 1994, Sayeg and Gregory 1991). This improves the sensitivity and the linearity of the dose response. While these densitometers can make measurements with resolutions up to 0.3 μm (Sayeg and Gregory 1991), they are expensive.

The extremely high resolution of radiochromic film warrants a method of reading which can extract all the available data. Modern scanners, often used for scanning photographs for desktop publishing purposes, offer high resolution images which are easily and quickly obtained. The use of one of these scanners was investigated for analysing exposed radiochromic film.

A.2 Materials and Methods

The scanner used was a Hewlett Packard ScanJet IIcx. This scanner offers a user defined resolution up to about 60 dots/mm. with various colour and black and white imaging modes. The software package HP DeskScan II (version 2.3) for Windows was used to drive the scanner. The film employed for these experiments was GafChromic dosimetry media. type MD-55. model 37-041, Lot # 940818 (GAF Chemicals Corp.. New Jersey. USA). The resolution of this film is 1200 lines/mm (distributor's product notes). The film is supplied in square sheets approximately 12 cm on a side. The film was stored at 4 °C in a light proof envelope until just prior to use. The densitometer used was

a Therados RFA 300 (Scanditronix, Uppsala, Sweden). The spot size of this densitometer is approximately 2 mm^2, the step between adjacent measurements was chosen to be 0.1 mm, the smallest possible.

The scanner has the capability of producing colour images consisting of three components: red, green and blue. The intensity of the red component varies most with dose, as expected, due to the absorption peak of the film in the red part of the spectrum. The relationships between dose and intensity of each of the colour components, and of the scanner signal for black and white images, were compared. The variation of scanner signal with dose for black and white images was found to be smoother than any of the colour components. Therefore a black and white photograph imaging mode was used for all subsequent scans. This mode uses a 256 element gray-scale, with a scanner signal of 256 for a white object and 1 for a black object. The automatic contrast and brightness enhancement functions in the software used to drive the scanner were turned off.

The images produced by the scanner were loaded into the software package MATLAB (The Mathworks, Inc., version 4.2c). This allows for the representation of the image as a matrix which may be manipulated for the purposes of image enhancement, enlargement, and mapping of isodoses or depth doses.

A calibration to convert from raw scanner-signal to dose was done. This was achieved by placing 12 mm by 30 mm pieces of film on the surface of a 10 cm thick Perspex phantom of dimensions 20 cm by 20 cm, and irradiating them to doses in the range 0–95 Gy with a Philips RT-100 superficial X-ray machine (55 kV_p, 0.78 mm Al HVL, 5 cm diameter field, 10 cm SSD). This radiation quality was chosen because the film and scanning technique are to be used for examining dose distributions around ophthalmic applicators loaded with ^{125}I seeds. The mean energy of ^{125}I emissions is about 27 keV, close to the mean energy of the 55 kV_p X-ray beam (Muench *et al* 1991).

To ensure that a uniform dose had been delivered to the calibration films, scanner signal profiles across the width and length of the films were examined. Across the 12 mm width and 30 mm length of the films the profiles were flat and there was no detectable variation of scanner signal with position, apart from the digital noise inherent in any scan. A portion of each calibration film 12 mm wide and approximately 7 mm in length was reserved for handling and film identification. This portion was not included in the region of interest, which was then approximately 12 mm by 23 mm.

The dose at the surface of Perspex was calculated from a measurement of the absolute exposure in air, in accordance with the IAEA protocol (IAEA 1987). The exposure was measured with a type 2532/3 0.03 cm^3 soft X-ray

parallel plate ionization chamber (NE Technology Ltd., Reading, England) calibrated in air against a primary national standard. A Farmer electrometer (NE Technology Ltd., Reading, England) was used to measure the charge collected by this chamber. The weighted mean value of the ratio of mass energy absorption coefficients of Perspex to air was determined to be $[\overline{\mu}_{en}/\rho]^{P}_{a} = 0.622$. This value applies for the spectrum produced by the Philips RT-100 operating at 55 kV_p. The 55 kV_p X-ray spectrum used to calculate the weighted mean had previously been measured with a high purity liquid nitrogen cooled germanium detector (EG&G ORTEC, Tennessee, USA). The measurement was performed with multiple collimations of the beam and at an FSD of 8 m. The backscatter factor for Perspex for an HVL and field size equivalent to that used in the film calibration was calculated by Grosswendt (1984) to be 1.17 and measured by Stanton *et al* (1982) to be 1.18. A Monte Carlo simulation employing the EGS4 package (Nelson *et al* 1985) was used to calculate the value of BSF for Perspex as 1.17. Using these dosimetry factors, the dose rate at the surface of the Perspex was calculated to be 6.80 Gy/min. Combining the uncertainties for the dosimetry factors lead to an uncertainty of 3% in the dose rate at the surface of Perspex.

The calibration films were scanned at a resolution of 10 dots/mm. The resulting scanner signal matrix for each film contained approximately 25 000 elements which were averaged to find the mean scanner signal corresponding to the applied dose. The standard deviation of each element of the scanner signal matrix is approximately 2. For each matrix element, the variation about the mean is caused by digital noise, resulting from the rounding of the scanner signal so that it takes on an integer value.

The calibration films were scanned several times in the three weeks after the initial scan. The mean value of the scanner signal for a uniformly irradiated film varied by up to 2% from the value found in the first scan. The standard deviation of the values of individual scanner signal matrix elements did not vary significantly from 2. Therefore 2% was taken as the uncertainty in scanner signal for the calibration films.

The net optical density, OD, of a point on the film is given by the equation:

$$OD = \log_{10}\left(\frac{S_0}{S}\right) \tag{A.1}$$

where S_0 is the 'dark current', i.e. the scanner signal for an unexposed film, and S is the scanner signal for the film at the point of interest. Chiu-Tsao *et al* (1994) found that the optical density of radiochromic film analysed with a broad band densitometer is best modelled by a power function of dose. Follo-

wing this method, we took the optical density to be dependent on the dose D in the following way:

$$\log_{10}\left(\frac{S_0}{S}\right) = aD^{\alpha} \tag{A.2}$$

where a and α are constants. These constants are determined by taking the log of equation A.2, resulting in:

$$\ln\left[\log_{10}\left(\frac{S_0}{S}\right)\right] = \ln(a) + \alpha\ln(D). \tag{A.3}$$

A plot of $\ln\left[\log_{10}\left(\frac{S_0}{S}\right)\right]$ against $\ln(D)$ produces a straight line with slope α, intercept $\ln(a)$ and linear regression coefficient $r = 0.999$. A least-squares linear fit to the calibration data yielded the constants: $\alpha = 0.719$ and $a = 0.0180$. A.2 is solved for dose and becomes. after substitution of the constants:

$$D = \left[55.6\log_{10}\left(\frac{S_0}{S}\right)\right]^{1.39}. \tag{A.4}$$

This expression for dose in terms of the measured scanner signal is applied to each element of the matrix of scanner signal data, converting it to a dose matrix. The dependence of optical density on dose is shown in figure A.1 with equation A.2 represented by the solid line. Our value of the exponent in the power function of dose is 0.719, in comparison to the value 0.858 obtained by Chiu-Tsao *et al* (1994) for radiochromic film irradiated with ^{125}I . The curve we obtained to describe the variation of optical density with dose appears to be in good agreement with the curve obtained by Chiu-Tsao *et al* (1994) for an equivalent radiation energy.

The uncertainty in the dose at a point on a non-uniformly irradiated film is determined by the standard deviation of the value of the scanner signal matrix element corresponding to that point. Assigning the minimum detectable dose as corresponding to three standard deviations away from the zero dose scanner signal put the minimum detectable dose at 0.7 Gy.

The standard deviation of elements in a scanner signal matrix is independent of the resolution of the scan. Therefore if high resolution scans are acquired. averaging of adjacent matrix elements may be done. resulting in a reduction of the noise. If an initial scan of sufficiently high resolution is taken. the reduction in resolution caused by averaging adjacent matrix elements will not be a problem except for cases where very steep dose gradients are present.

Several workers (Chiu-Tsao *et al* 1994. Chu *et al* 1990) recommend that radiochromic film be left for a period after irradiation to allow the colour

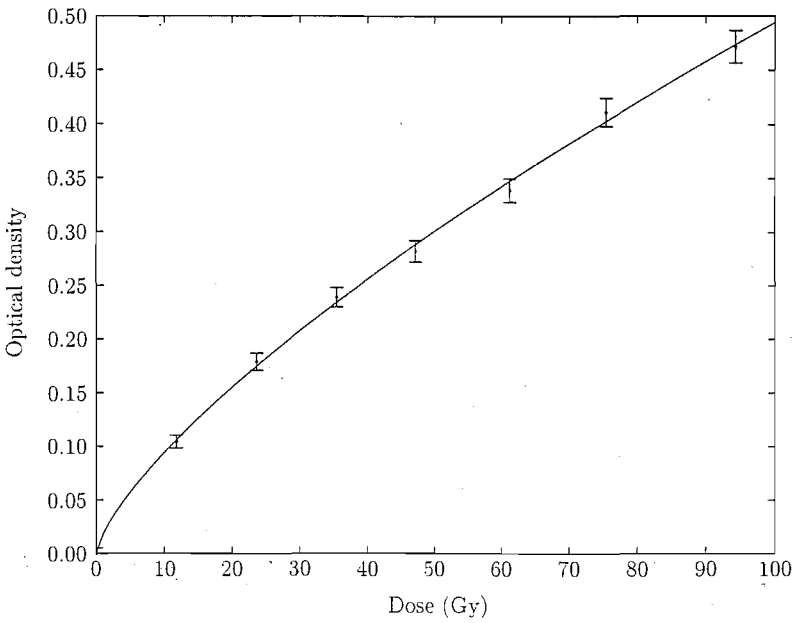

Figure A.1: Curve showing the dependence of optical density on dose. The data points corresponding to the optical density of films uniformily irradiated to doses in the range 0-95 Gy with 55 kV_p X-rays at the surface of a Perspex phantom. The error bars demonstrate the level of uncertainty in the optical density, based on the uncertainty in measurements of scanner signal. The solid line shows how the model represented by equation A.2 fits the experimental data.

change to stabilize. It is shown (Chu *et al* 1990) that the optical density can change by 16% in the 24 hr immediately after irradiation, but in the following 24 hr the colour change is less than 1%. Saylor *et al* (1988) showed that over a period of 41 days, the colour change in the exposed film was significant only in the 48 hr after irradiation. Because of these findings we recommend that measurement films be scanned with the same post-irradiation delay as the calibration films to eliminate errors due to colour development with time. For all the experiments described here, a waiting period of 48 hr was observed between irradiation and scanning. During this waiting period, the exposed film was stored at room temperature and away from light. Three weeks after the initial post-irradiation scan, the calibration films were scanned again. The scanner signals obtained in this later scan showed no deviation, within the limits of uncertainty, from the scanner signals acquired in the first scan. During this three week period, the film was stored at room temperature and away from light.

Since the film is sensitive to ultraviolet light with photon energies greater than 4 eV (Sayeg and Gregory 1991), the possibility that the lamp in the scanner may expose the film and alter its colour was investigated. Five scans of a single 12 mm by 30 mm piece of unirradiated film were taken in quick succession, allowing no time for the lamp to cool down between each scan. Each scan took approximately three seconds to acquire. A waiting period of five minutes was then observed before a second set of five scans was taken. Based on the physical dimensions of the lamp, five minutes was assumed to be sufficient time for the lamp to cool to near room temperature. The process was repeated until a total of twenty scans had been done, in four sets of five. This regime was used to ascertain whether there was any variation in readings for scans taken in quick succession due to the lamp heating up, and also to investigate the variation of measured signal as a function of the the total number of scans.

To illustrate the higher signal to noise ratio of the scanner, the central axis depth dose for 55 kV_p X-rays (0.78 mm Al HVL, 5 cm diameter field, 10 cm SSD) in Perspex was measured using both broad band densitometry and by scanning at a resolution of 10 dots/mm. A piece of radiochromic film approximately 5 cm by 6 cm was placed between two large slabs of Perspex and irradiated.

The depth dose measured with the scanner was produced by plotting the single column of the dose matrix which coincided with the central axis of the radiation distribution. This column represents a strip of film 0.1 mm wide. The depth dose data from the densitometer was found by taking measurements along the central axis of the radiation distribution. Due to the size of the spot of light used by the densitometer, this depth dose is effectively measuring the average optical density of a strip of radiochromic film about 1 mm wide. The results for both measurements are shown in figure A.2.

The spatial flatness of the scanner response was determined by taking a scan with no film in place. This scan covered the whole scanner bed (i.e. the glass sheet of dimensions 230 mm × 370 mm, on which objects to be scanned are placed) and showed that around the edges of the bed there was a significant amount of leakage of ambient light but within 2 mm from the edge of the bed, the ambient light contribution to the signal fell to zero. The signal within the region not affected by ambient light was found to have no variation with position. This is an important finding as it allows for scans of large pieces of exposed film to be taken. The size of the scanner bed allows for full sheets of radiochromic film to be analysed.

Measurements of the calibration films were also made with a Hewlett

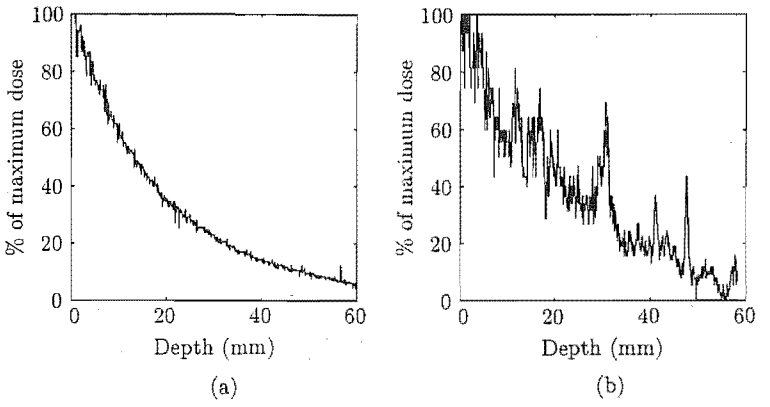

Figure A.2: Comparison between central axis depth doses for 55 kV_p X-rays (0.78 mm Al HVL. 5 cm diameter field, 10 cm SSD) obtained from a scan of radiochromic film exposed to this radiation field; (b) broad-band densitometry measurement of the central axis of the dose distribution, taken from the same film used in (a).

Packard ScanJet 4c, driven using the software package HP DeskScan II (version 2.3) for Windows. The mean scanner signals for each calibration film were found to be up to 8% higher than the values found using the Hewlett Packard ScanJet IIcx. This indicates that a separate calibration needs to be done for every scanner.

To demonstrate the applicability of this technique to brachytherapy, the dose distribution around a 15 mm COMS-type ophthalmic applicator (Radiation Oncology Physics and Engineering Services (ROPES), NSW, Australia), loaded with ten type 6702 ^{125}I seeds (Amersham International plc, Buckinghamshire, England) was measured. A Perspex phantom was made with a dome shaped protrusion having the same radius of curvature as the concave applicator. The phantom was made in two halves. The film was cut to the shape of the dome and placed between the two halves of the phantom. With the applicator placed on top of the dome, the film was flush against its inner surface and so measured the dose distribution in the eye-shaped phantom. The film was exposed for 24 hr, resulting in a maximum dose to the film of about 100 Gy. Because of the steep dose gradients found around the ophthalmic applicator, the film was scanned at a resolution of 20 dots/mm.

A.3 Results

Although the mean scanner signal for a particular film can vary by up to 2% for scans taken on different days, the multiple scan experiment, where scans were taken in quick succession with no more than five minutes between each, showed that the mean scanner signal for a uniformly irradiated film varied by no more than 0.3% from the value for any other scan taken in the multiple scan experiment. When five scans were taken in quick succession, it was found that the mean scanner signal for the fifth scan was up to 0.3% higher than the mean value of the first scan of that set of five. After the five minute waiting period, the scanner signal had dropped to close to its value in the first scan of the set. This effect is thought to be due to the lamp warming up when scans are taken in quick succession, changing the light intensity.

The reading from the first scan of each set, taken after the five minute waiting period, decreased as the number of scans increased. The reading for the first scan of the last set (i.e. the sixteenth scan) was 0.08% lower than for the first scan of the first set. The standard deviation of individual scanner signal matrix elements about the mean value, caused by digital noise, was about 2. The uncertainty in the mean scanner signal value was taken to be this standard deviation divided by the square root of the number of elements in the matrix from which the mean was found. The scanner signal matrix contained approximately 25 000 elements, so the uncertainty in the mean signal was ± 0.02. The unirradiated film used in the experiment had a mean scanner signal of approximately 198, so the relative uncertainty is $\pm 0.01\%$. The experiment indicates that multiple scans do expose the film, but that the effect is small. It also shows that multiple scans should be taken at least five minutes apart, allowing the lamp to return to near room temperature.

From figure A.2 it can be seen that the scanner produces data with considerably less noise than the densitometer. The resolution of the scan is approximately two orders of magnitude lower than the resolution of the film and so the value of each $0.01\,\mathrm{mm}^2$ pixel in the image matrix should not contain any random fluctuations due to the film. Therefore the noise in this depth dose is due to the scanner rather than the film. The noise can be reduced by averaging several columns of the dose matrix about the central axis of the dose distribution.

The dose distribution around the COMS-type ophthalmic applicator, recorded with radiochromic film, is shown in figure A.3. The overlayed isodose contour lines, given as percentage of maximum dose, were calculated using the dose matrix. The contribution from individual ^{125}I seeds can clearly be seen

in four regions near the surface of the dome, next to where the seeds were held by the applicator. The isodose contours show that the contribution from individual seeds only effects the top 2 mm of the film, demonstrating the dose which would be given to the sclera of the eye.

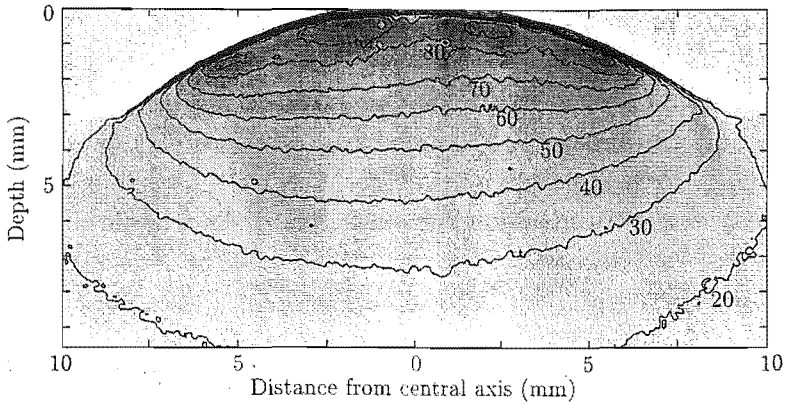

Figure A.3: Image and isodose contours obtained from GafChromic film measurement of the dose distribution around a 15 mm COMS-type ophthalmic applicator, loaded with ^{125}I seeds. The dose distribution was measured in a Perspex dome-shaped phantom. The film was scanned at a resolution of 20 dots/mm. The isodose contours are labbled as a percentage of the maximum dose.

A.4 Conclusions

The high resolution of radiochromic film makes it useful for measuring dose distributions which are difficult to determine by conventional means. The combination of the film and scanning technique, which takes advantage of the resolution of the film, is a powerful one. The relatively flat energy response of the film and its low effective atomic number makes it appropriate for the measurement of low energy radiation.

The ability of the scanner to respond to a large dynamic range in contrast over small distances means that small-scale dose distributions can be visualised. In particular, the steep dose gradients found around brachytherapy sources can easily be mapped. Conventional types of dosimeter, which often have dimensions of the same scale or larger than the dose distribution in question, are poorly suited to such measurements. Investigations of the dose distribution around ophthalmic applicators and the seeds which they are loaded with have been made by various means. Large arrays of small thermo-

luminescent dosimeters (de la Zerda *et al* 1996, Hartmann *et al* 1983), analytic models (Luxton *et al* 1988) and Monte Carlo simulations (Burns and Raeside 1987, Herbold *et al* 1988, Sakelliou *et al* 1992) have all been used. Radiochromic film analysed with a high resolution scanner has the advantage of simplicity and speed over these techniques.

The scanning technique provides more information on the dose distributions than can be obtained with the low resolution broad–band densitometer used in these experiments and common in many hospitals. Scanning the films is a fast and simple process which requires relatively inexpensive off-the-shelf technology with which many hospitals will already be equipped.

Dosimetry protocols for measurement of X-rays with energies in the range 150 - 400 kV_p (e.g. IPEMB, IAEA) will require dose measurements at depth in a water phantom. The combination of high resolution film and scanning is ideal for assessing percent depth doses so that surface dose may be calculated from a measurement done at depth.

A.5 Acknowledgements

This research has been supported in part by the Health Research Council of New Zealand and by the Canterbury-West Coast Division of the Cancer Society of New Zealand.

References

[1] Burns G S and Raeside D E 1987 Monte Carlo simulation of the dose distribution around ^{125}I seeds *Med. Phys.* **13** 420-4

[2] Chiu-Tsao S, de la Zerda A, Lin J and Kim J H 1994 High-sensitivity GafChromic film dosimetry for ^{125}I seed *Med. Phys.* **21** 651-7

[3] Chu R D H, Van Dyk G, Lewis D F, O'Hara K P J, Buckland B W and Dinelle F 1990 GafChromic dosimetry media: A new high dose, thin film routine dosimeter and dose mapping tool *Radiat. Phys. Chem.* **35** 767-73

[4] de la Zerda A, Chiu-Tsao S, Lin J, Boulay L L, Kanna I, Kim J H and Tsao H S 1996 ^{125}I eye plaque dose distribution including penumbra characteristics *Med. Phys.* **23** 407-18

[5] Grosswendt B 1984 Backscatter factors for X-rays generated at voltages between 10 and 100 kV *Phys. Med. Biol.* **29** 579-91

[6] Hartmann G H, Schlegal W and Scharfenberg H 1983 The three-dimensional dose distribution of ^{125}I seeds in tissue *Phys. Med. Biol.* **28** 693-9

[7] Herbold G, Hartmann G, Treuer H and Lorenz W J 1988 Monte Carlo calculation of energy built-up factors in the range from 15 keV to 100 keV, with special reference to the dosimetry of ^{125}I seeds *Phys. Med. Biol.* **33** 1037-53

[8] IAEA 1987 Absorbed dose determination in photon and electron beams *Technical Report Series 277* (Vienna: IAEA)

[9] Luxton G, Astrahan M A, Liggett P E, Neblett D L, Cohen D M and Petrovich Z 1988 Dosimetric calculations and measurements of gold plaque ophthalmic applicators using iridium-192 and iodine-125 seeds *Int. J. Radiat. Oncol. Biol. Phys.* **15** 167-76

[10] McLaughlin W L and Chalkley L 1965 Low atomic numbered dye systems for ionizing radiation measurements *Photo. Sci. Eng.* **9** 159-65

[11] Muench P J, Meigooni A S, Nath R and McLaughlin W L 1991 Photon energy dependence of the sensitivity of radiochromic film and comparison with silver halide film and LiF TLDs used for brachytherapy dosimetry *Med. Phys.* **18** 769-75

[12] Nelson W R, Hirayama H and Rogers D W O 1985 The EGS4 Code System *Stanford Linear Accelerator Center Report* SLAC-265

[13] Sakelliou L, Sakellariou K, Sarigiannis K, Angelopoulos A, Perris A and Zarris G 1992 Dose rate distributions around ^{60}Co, ^{137}Cs, ^{198}Au, ^{192}Ir, ^{241}Am, ^{125}I (models 6702 and 6711) brachytherapy sources and the nuclide ^{99}Tc^{m} *Phys. Med. Biol.* **37** 1859-72

[14] Sayeg J A and Gregory R C 1991 A new method for characterizing beta-ray ophthalmic applicator sources *Med. Phys.* **18** 453-61

[15] Saylor M C, Tamargo T T, McLaughlin W L, Khan H M, Lewis D F and Schenfele R D 1988 A thin film recording medium for use in food irradiation *Radiat. Phys. Chem.* **31** 529-36

[16] Stanton L, Brattelli S D and Day J L 1982 Measurements of diagnostic X-ray backscatter by a novel ion chamber method *Med. Phys.* **9** 121-31

Published paper - Australasian Physical and Engineering Sciences in Medicine

Appendix B

Field Size Dependence of Effective Source Distance and Field Factors of a 9 MeV Electron Beam

Sháun P. Baggarley, Diana M. Mannering, Richard P. Hugtenburg and John R. Turner
Department of Medical Physics and Bioengineering, Christchurch Hospital, Christchurch, New Zealand.

Abstract

Effective source distances and field factors were measured for a number of square and rectangular fields using a 9 MeV electron beam from a Varian 2100-C linear accelerator. Mathematical relationships between effective source distance and field size, and field factor and field size were derived. For 9 MeV electrons, effective source distance is dependent on the field area and applicator cone, while field factors are dependent on the elongation of the field, the field area and applicator cone. Measured field factor data for rectangular fields were compared to field factors obtained using the "square root" method and found to agree to within 0.5%. In some instances, field factors can vary up to 10% for the same field size in different electron applicator cones.

B.1 Introduction

At the time of commissioning of the Varian 2100-C linear accelerator, field factors and effective source distances in air were measured for the square field sizes of the electron applicator cones. The "in-air" effective source distances were obtained using the method described by Thomas[7]. Field factors and effective source distances for other field sizes, both square and rectangular, were determined from linear interpolation of the commissioning data. Tables of electron field factors for various combinations of energy and applicator size were constructed.

At a later date when square and rectangular cerrobend cut-outs were fa-

bricated for patients it was wrongly assumed that interpolation between applicator sizes would be adequate.Subsequent direct measurements showed up the discrepancies between interpolated and actual data, particularly for 9 MeV electrons.This instigated detailed measurements of field factor with varying field size and applicator cone. Repeat measurements of effective source distances in a phantom were also made. Two methods have been investigated for the calculation of rectangular field factors - the effective field size technique and the "square root" method.

B.2 Method

Measurements were made for the 6× 6, 10×10, 15×15 and 20× 20 cm^2 applicator cones with various square and rectangular cerrobend cut-outs. Measurements were not made for the 25× 25 cm^2 applicator as it is rarely used clinically.

Field factors were determined by dividing the measured output at dose maximum for a given field and applicator cone by the measured output at dose maximum for a 10×10 cm^2 field using a 10×10 cm^2 applicator cone.

Effective source distances were found from measurements of the variation in dose with varying isocentre to chamber distance using the method described by the AAPM Task Group 25[65]. To measure the dose variation we used a PTW Markus parallel plate ionisation chamber in a Solid Water phantom. The chamber was positioned at the depth of dose maximum (1.5 cm) for the 9 MeV electron beam. Output measurements were made with the surface of the phantom 2 cm above isocentre, at isocentre and 5, 10, 15 and 20 cm below isocentre, see figure B.1. The average of each set of measurements was normalised to the average of the measurements made at isocentre. The square root of the reciprocal of the normalised measurements was plotted against the isocentre to phantom distance of each measurement. This is related by the following equation

$$\frac{Do}{Dg} = \frac{(ESD + d + g)^2}{(ESD + d)^2} \tag{B.1}$$

and can be rearranged as

$$\left(\frac{Do}{Dg}\right)^{\frac{1}{2}} = \frac{g}{(ESD + d)} + 1 \tag{B.2}$$

where Do is the measured dose with the phantom surface at isocentre and Dg is the measured dose for a distance g between the isocentre and phantom

surface. The chamber is positioned in the phantom at a depth d and ESD is the effective source distance. If the dose reduction matches the inverse square law the graph will be a straight line with a slope of 1/(ESD + d).

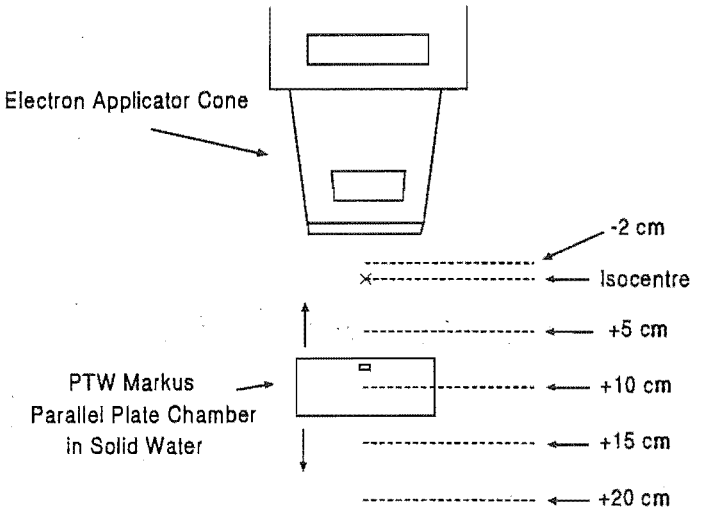

Figure B.1: Effective source distance measurement set-up

B.3 Results

Figures B.2 through B.4 illustrate the results of the effective source distance measurements. The rectangular fields are highlighted, where in this case the equivalent field size was chosen as a square of equal area to the rectangle. Mathematical regression was used to fit curves to the data for each applicator, shown as dashed line, which enables one to predict the E.S.D. given an equivalent square field.

Figure B.5 illustrates the variation in field factors for the range of applicator and cut-out sizes. Results for the 6 x 6 cm2 applicator are included for completeness. In this case the equivalent field size is related by the following equation.

$$Cequiv = k\,(a \times b)^{\frac{1}{2}}\,. \tag{B.3}$$

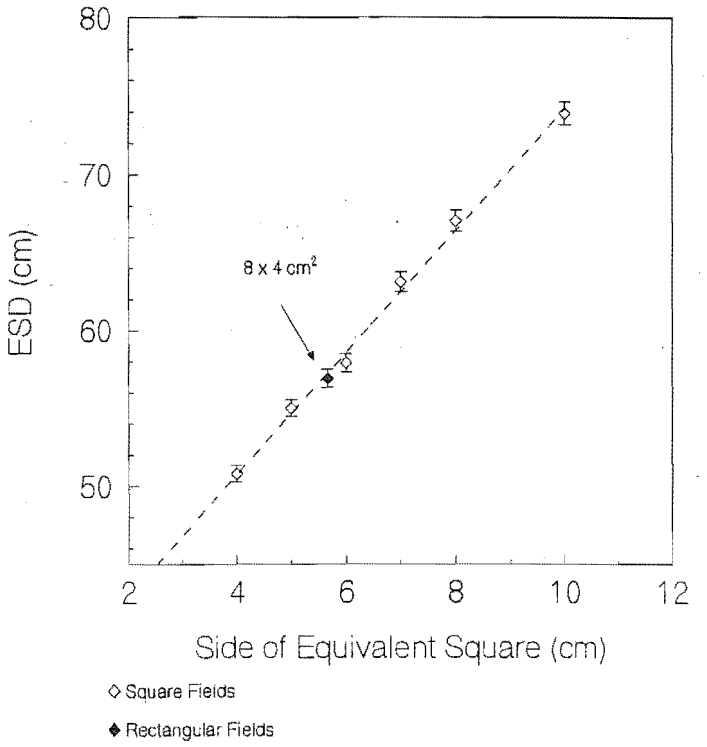

Figure B.2: Effective source distances for 9 MeV electrons, $10\times10\text{cm}^2$ applicator

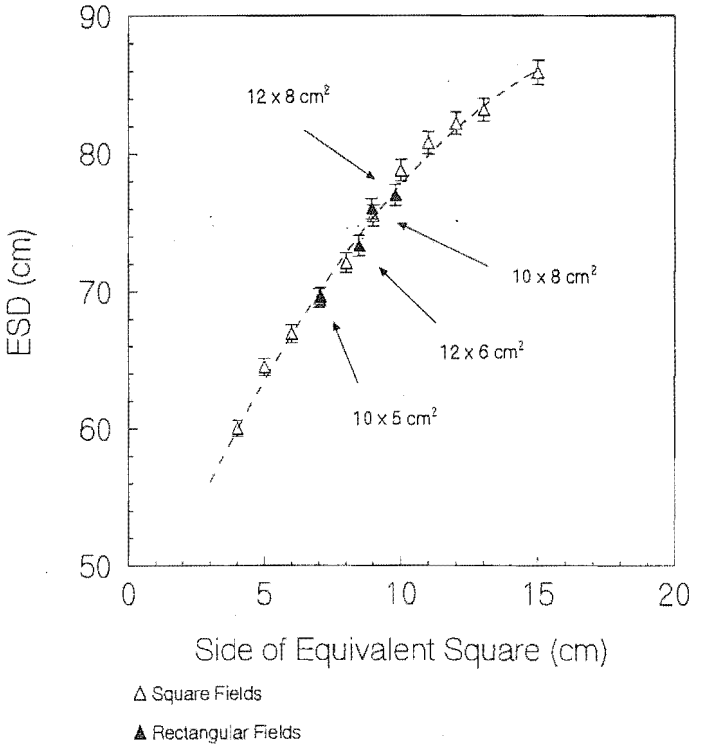

Figure B.3: Effective source distances for 9 MeV electron, $15\times15\text{cm}^2$ applicator

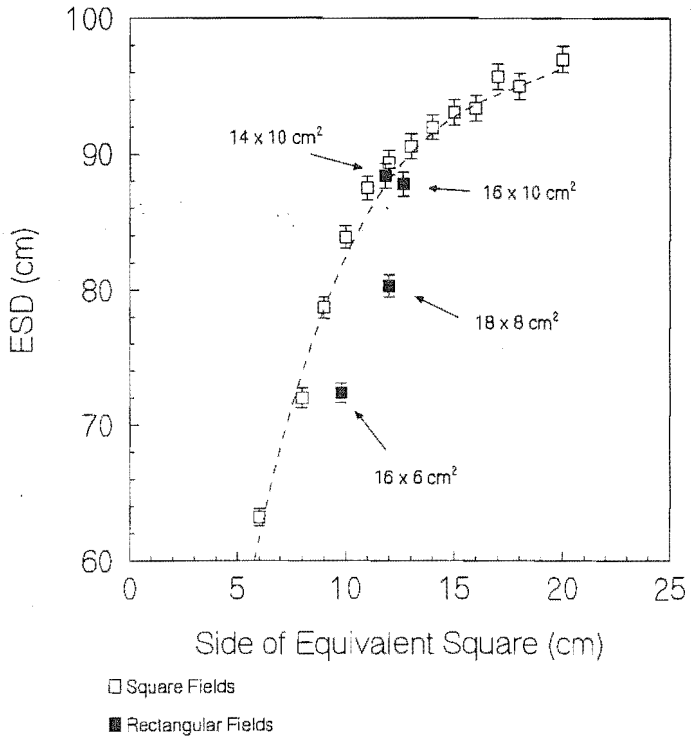

Figure B.4: Effective source distances for 9 MeV electrons, $20\times20\text{cm}^2$ applicator

Applicator Size (cm2)	a1	a2	a3	a4
10 × 10	0.9649	0.00347	2.4455	0.8092
15 × 15	1.082	0.00102	1.4708	0.7412
20 × 20	1.032	0.00117	4.4934	0.8772

Table B.1: Coefficients for Field Factor Equations for both square and rectangular fields.

where Cequiv is the side of the equivalent square, a and b are the two sides of the rectangle and k is a coefficient that is dependent on the ratio of a to b (with a > b), i. e. the elongation of the field as determined by Klevenhagen[3].

The general equation obtained for the field factor data is shown below. The coefficients of the equation for each applicator are shown in table B.1.

B.4 Discussion

The effective source distance and field factor measurements show reasonable agreement between the square and rectangular field data, with the exception of 20 × 20 cm^2 applicator data. As the larger applicators tend to be used less frequently we recommend that direct measurements be performed for the 20×20 cm^2 applicator.

While the 20×20 cm^2 applicator field factor data for rectangular fields lies outside the ±0.5% range of the mathematical best fit curve, we find that all of the data is within 1% of the curve so the expression is useful within these prescribed limits. The rectangular field effective source distance data for the 20× 20 cm^2 applicator also lie outside the best fit curve. In this case an elongation correction to the equivalent square could improve the correlation between the rectangular and square field data. Such an approach offers an alternative to the recommendations adopted within our department.

We find that for the effective source distance and field factor data the equivalent square was related to the field area. But for the rectangular field measurements to correlate with square field factor data, the equivalent square also requires a correction for the elongation of the field. Agreement between square and rectangular fields is therefore dependent on the definition of the equivalent square, and in particular on the elongation factor applied.

Using the mathematical expressions derived for each applicator it is possible to calculate an effective source distance or field factor given almost any square or rectangular field size. However the expressions are only valid over the range of field dimensions that were measured. A number of papers [4, 5, 6] refer to the "square root" method of obtaining rectangular field factors. This method

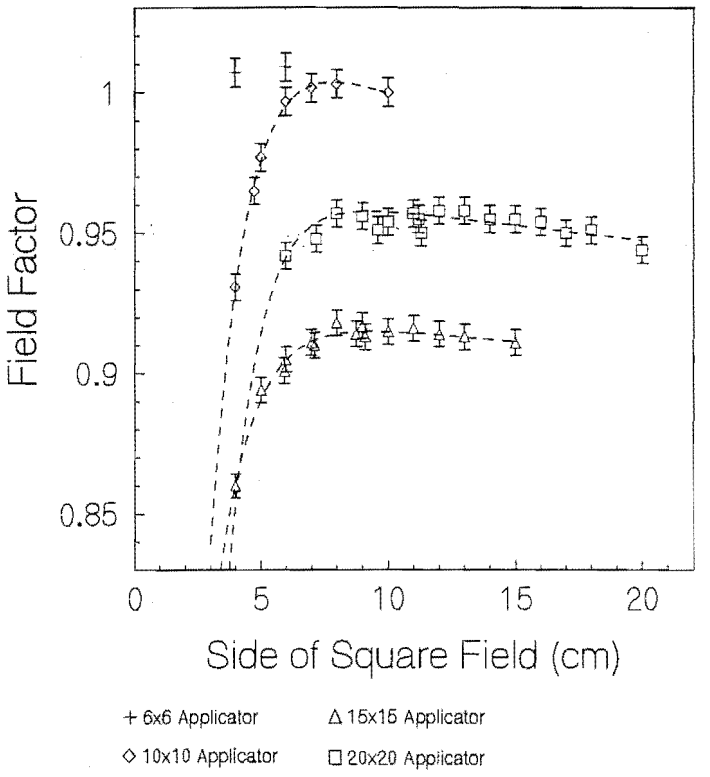

Figure B.5: Field factors for 9 MeV electrons for both square and rectangular fields

relates rectangular and square field factors by the following equation:

$$FF(a \times b) = [FF(a \times a) \bullet FF(b \times b)]^{\frac{1}{2}} \quad \text{(B.4)}$$

where FF is the field factor in each case. Table B.2 shows measured field factors for rectangular fields and the corresponding field factor calculated from measured square field data using the equation above. Two advantages in using this method are that an equivalent square is not required and only square field data need be obtained.

A point to note is the variation in field factor with change in applicator size, as demonstrated in figure B.5. Clear distinction must be made between a rectangular or square cerrobend aperture and a similar sized applicator. The data in figure B.5. shows that one must consider the applicator size rather that the cerrobend aperture size; errors up to 10% may otherwise be observed. For example, an 8× 10 cm^2 cerrobend cut-out requires a 15 × 15 cm^2 applicator as it cannot be fabricated for a 10×10 cm^2 applicator. If a calculation is made assuming a 10 × 10 cm^2 applicator the calculation will out by 9.4% (see figure B.5).

Rectangular Field Size (cm2)	Measured Field Factor	"Square Root" Method	Difference (%)
8 x 4	0.965	0.966	0.1
10 x 5	0.901	0.904	0.3
10 x 8	0.914	0.916	0.2
12 x 6	0.910	0.909	0.1
12 x 8	0.913	0.916	0.3
14 x 10	0.950	0.954	0.4
16 x 6	0.948	0.948	0.0
16 x 10	0.955	0.954	0.1
18 x 8	0.951	0.954	0.3

Table B.2: Rectangular field factors.

B.5 Conclusion

We find that for 9 MeV electrons, effective source distance is dependent on field area and applicator cone, while field factors are dependent on the elongation of the field, field area and applicator cone. Field factor data have been shown to lie within 0.5% of the best fit curve for the 10 × 10 cm^2 and 15×15 cm^2

applicators and within 1% for the 20 × 20 cm^2 applicator. Effective source distance data is within 1% of the best fit curve for the 10× 10 cm^2 and 15×15 cm^2 applicators and the square field points of the 20 × 20 cm^2 applicator. Measured field factor data for rectangular fields agree to within 0.5% of those field factors obtained using the "square root" method. We find that in practice, using the "square root" method provides an easy and accurate way of estimating field factors. The advantage, however, in using regression equations is in the ability to interpolate between standard settings without having to perform further square field measurements. Finally we observe that field factors can vary up to 10%, for the same field size with the largest differences occurring between the 10×10 cm^2 and 15×15 cm^2 applicator cones.

References

[1] Manufactured by RMI.

[2] Khan, F. M., K. P. Doppke, K. R. Hogstrom, G. J. Kutchner, R. Nath, S. C. Prasad, J. A. Purdy, M. Rozenfeld and B. L. Werner, 1991: Clinical electron beam dosimetry: Report of aapm task group no. 25, *Medical Physics*, **18**(1), 73–109.

[3] Klevenhagen, S. C., 19: *Physics of Electron Beam Therapy, Medical Physics Handbooks No. 13*, Adam Hilger Ltd, Bristol, England.

[4] McParland, B. J., 1987: A parameterization of the electron beam output factors of a 25 mev linear accelerator, *Medical Physics*, **14**(4), 665–669.

[5] ———, 1992: An analysis of equivalent fields for electron beam central-axis dose calculations, *Medical Physics*, **19**(4), 901–906.

[6] Mills, M. D., K. R. Hogstrom and P. R. Almond, 1982: Prediction of electron beam output factors, *Medical Physics*, **9**(1), 60–68.

[7] Thomas, S. J., 1988: Virtual source distances for electron beams between 5 and 20 MeV, *Phys. Med. Biol.*, **33**(11), 1325–1328.